

“Statistical Comparison of SAR Backscatter from Icebergs
Embedded in Sea Ice and in Open Water using RADARSAT-2
Images of in Newfoundland waters and the Davis Strait”

By

Umma Hafsa Himi, B.Sc.

A thesis submitted to the school of Graduate Studies in partial

fulfillment of the requirements for the degree of

Master of Engineering

Electrical Engineering Program

Memorial University

October 2019

St. John's Newfoundland & Labrador

THIS PAGE LEFT INTENTIONALLY BLANK

Abstract

Icebergs are considered a threat to marine operations. Satellite monitoring of icebergs is one option to aid in the development of iceberg hazard maps. Satellite synthetic aperture radar (SAR) is an obvious choice because of its relative weather independence, day and night operation. Nonetheless, the detection of icebergs in SAR can be a challenge, particularly with high iceberg areal density, heterogeneous background clutter and the presence of sea ice.

This thesis investigates and compares polarimetric signatures of icebergs embedded in sea ice and icebergs in open water. In this thesis, RADARSAT-2 images have been used for analysis, which was acquired over locations near the coastline (approximately 3-35 km) of the islands of Newfoundland and Greenland. All icebergs considered here are in the lower incident angle range (below 30 degrees) of the SAR acquisition geometry. For analysis, polarimetry parameters such as co- (HH) and cross- (HV) polarization and several decomposition techniques, specifically Pauli, Freeman-Durden, Yamaguchi, Cloud-Pottier and van Zyl classification, have been used to determine the polarimetric signatures of icebergs and sea ice. Statistical hypothesis tests were used to determine the differences among backscatters from different icebergs. Statistical results tend to show a dominant surface scattering mechanism for icebergs. Moreover, icebergs in open water produce larger volume scatter than icebergs in sea ice, while icebergs in sea ice produce larger surface scatter than icebergs in open water. In addition, there appear to be minor observable differences between icebergs in Greenland and icebergs in Newfoundland.

THIS PAGE LEFT INTENTIONALLY BLANK

Acknowledgements

This thesis would not be possible without support from several people and several sources. Foremost, I would like to express my sincere thanks and gratitude to my supervisors, Dr. Peter McGuire and Desmond Power for their continuous support of my M.Eng. study and research. Besides teaching me scientific research, they are icons of enormous motivation and patience who helped me keep on the right track and overcome many obstacles throughout my research. I am truly blessed to have such knowledgeable and nice supervisors during my program.

Besides my supervisors, I thank Centre for Cold Oceans Resources Engineering (C-CORE) and the Natural Sciences and Engineering Research Council of Canada (NSERC) for providing me sufficient funds, a wonderful office environment and all the equipment needed for my research.

I would also like to thank C-CORE, Defence Research & Development Canada (DRDC), Canadian Space Agency and the Canadian Ice Service for the provision of satellite imagery for this study. The satellite imagery analysed herein was made available through a collaboration agreement established for my NSERC grant. These data were collected and ground truthed through funding provided from several different research programs, with

funds made available through DRDC, Cairn Energy, and the Research and Development Corporation of Newfoundland and Labrador (RDC)¹.

My sincere thanks also to Dr. Bahram Salehi, who was my instructor in the ‘Applied Remote Sensing’ course. It was a well-organized course that taught me all the basics of remote sensing. I also thank C-CORE employees, Carl Howell and Pamela Burke for helping me to collect data for my research which was very time consuming.

Finally, I thank specially to my Husband, Saimoom, who was always beside me and my parents for their selfless support and encouragement for my scientific discoveries throughout my education.

¹ RDC has since been renamed InnovateNL.

Table of Contents

1. Introduction.....	1
1.1 Purpose of the Study	4
2. Literature Review	6
2.1 Fundamentals of SAR	6
2.1.1 Synthetic Aperture Radar (SAR).....	7
2.1.2 SAR imaging	8
2.1.3 SAR Polarization	12
2.1.4 Ocean Response to SAR.....	15
2.1.5 Icebergs and Sea Ice Response to SAR	16
2.2 Polarimetric Decomposition.....	18
2.2.1 Pauli Decomposition.....	20
2.2.2 van Zyl Decomposition	22
2.2.3 Freeman-Durden Decomposition	23
2.2.4 Yamaguchi Decomposition	25
2.2.5 Cloud-Pottier Decomposition	26

2.3 Statistical Tests.....	28
2.3.1 Two Tail T-test	30
2.3.2 One Tail T-test.....	32
2.4 Previous Work.....	32
2.4.1 Properties of Sea Ice and Icebergs.....	32
2.4.2 C-CORE’s Research on Iceberg Detection with SAR.....	33
2.4.3 Detection of Icebergs in Sea Ice using Polarimetric RADARSAT-2 Data	35
2.4.4 Iceberg Detection Using Full Polarimetric RADARSAT-2 Data in West Antarctica.....	36
2.4.5 Automatic Iceberg Detection in Open Water and Sea Ice	37
3. RADARSAT-2 Data.....	38
3.1 Data	39
3.2 Target Detection	44
3.3 Iceberg Detection Using Ground Truth information.....	46
4. Methodology	49
4.1 SAR Image Processing.....	50

4.1.1 Polarimetric Feature Extraction.....	50
4.1.2 Image Clipping.....	50
4.1.3 Masking.....	51
4.1.4 Filtering.....	53
4.2 Polarimetric Decompositions.....	54
4.3 Hypothesis Test.....	56
4.3.1 Two tail T-test.....	57
4.3.2 One tail T-test.....	59
5. Results.....	61
5.1 Radar Backscatter Plots.....	61
5.2 Decomposition Results.....	63
5.2.1 Icebergs in Open Water Versus in Sea Ice (NLSI Versus NLOW).....	64
5.2.2 Greenland Versus Newfoundland icebergs (GLOW versus NLOW).....	72
5.2.3 Statistical Comparison of Iceberg Groups.....	77
5.3 Hypothesis Test.....	82
5.3.1 Two Tail T-test.....	82

5.3.2 One Tail T-Test	85
5.4 Summary	87
5.5 Discussion	88
6. Conclusion	94
6.1 Limitations	95
6.2 Future Work	96
7. References	98
Appendix I	103
Appendix II.....	105
Appendix III	107
Appendix IV	109

List of Tables

Table 3.1	Image acquisition details	42
Table 4.1	Normality test, Pauli Volume (Iceberg in Sea Ice)	58
Table 4.2	Two tail T-test (assuming unequal samples) for Pauli decomposition volume scattering (sea ice versus open water)	60
Table 4.3	One tail T-test of Freeman-Durden surface scattering in sea ice and open water	61
Table 5.1	Two tail T-test of NLSI and NLOW group	84
Table 5.2	Two tail T-test of NLOW and GLOW group	85
Table 5.3	One tail T-test of NLSI and NLOW group (surface)	86
Table 5.4	One tail T-test of NLSI and NLOW group (double bounce, volume, helix)	87
Table 5.5	One tail T-test of NLOW and GLOW group	88

List of Figures

Figure 1.1	Iceberg's journey from Greenland to the Grand Banks of Newfoundland and Labrador (figure courtesy of C-CORE)	1
Figure 2.1	Basic radar imaging	7
Figure 2.2	SAR imaging geometry	9
Figure 2.3	Horizontal and vertical polarization	12
Figure 2.4	Backscatter Mechanism of iceberg and sea ice	17
Figure 2.5	Types of decomposition	19
Figure 2.6	Flow chart of Freeman-Durden decomposition (adapted from Lee and Pottier (2009))	24
Figure 2.7	H/α plane	27
Figure 2.8	Visual illustration of the one tail and two tail tests; Left: one-tailed T-test, although the picture is shaded on the right, it's a mirror image (critical region in the left will also be a one tailed test, the condition of rejection of null hypothesis then be, $t\text{-stat} < -t\text{-critical}$); Right: two tailed T-test	31
Figure 3.1	Grouping of data sets for analysis	39

Figure 3.2	Study area	41
Figure 3.3	Top: iceberg identifying using pixel/line information from ground truth data in PCI Geomatica; Bottom: Several icebergs that have been clipped from HV channel from a scene	47
Figure 3.4	Iceberg backscatter in SAR in different polarization channels	48
Figure 4.1	Flow chart of the processing chain	51
Figure 4.2	Clutter masking	54
Figure 4.3	Iceberg completely merged with sea ice clutter in both HV (left) and HH (right) channel; though it has the ground truth information (From field survey).	55
Figure 5.1	Comparison of polarimetric parameters (intensity) Left: HH vs HV; Right: HH vs VV	63
Figure 5.2	Comparison of polarimetric parameters (intensity) of Newfoundland and Greenland icebergs; Left: HH vs HV; Right: HH vs VV	64
Figure 5.3	Pauli decomposition of NLSI and NLOW group	66
Figure 5.4	Freeman-Durden decomposition of NLSI and NLOW group	67

Figure 5.5	van Zyl decomposition of NLSI and NLOW groups	68
Figure 5.6	van Zyl decomposition of NLSI and NLOW groups	69
Figure 5.7	(a) Backscatter comparison using Cloude-Pottier decomposition (b) H/α plane	71
Figure 5.8	Cloud-Pottier decomposition of a sea ice chip	72
Figure 5.9	Freeman-Durden decomposition of NLOW and GLOW groups	74
Figure 5.10	van Zyl decomposition results; Top: NLOW, Bottom: GLOW	75
Figure 5.11	Yamaguchi decomposition results; Top: NLOW; Bottom: GLOW	77
Figure 5.12	(a) Scatter plot of Cloude-Pottier decomposition; (b) H/α plane	78
Figure 5.13	Box Plot representation of Pauli decomposition results	81
Figure 5.14	Box Plot representation of Freeman-Durden decomposition results	82
Figure 5.15	Box Plot representation of van Zyl decomposition results	82
Figure 5.16	Box Plot representation of Yamaguchi decomposition results	83

List of Abbreviations and Symbols

dB	Normalized unitless intensity measure
CIS	Canadian Ice Service
RS-2	RADARSAT-2
RS-1	RADARSAT-1
SAR	Synthetic Aperture Radar
HH	Horizontal transmit and Horizontal receive polarization
HV	Horizontal transmit and Vertical receive polarization
VH	Vertical transmit and Horizontal receive polarization
VV	Vertical transmit and Vertical receive polarization
H	Entropy
A	Anisotropy
α	Alpha angle
δ	Significance level
S_{HH}	Scattering intensity value in HH channel
S_{HV}	Scattering intensity value in HV channel
σ^0	Radar cross section
SLC	Single look complex
CFAR	Constant False Alarm Rate

THIS PAGE LEFT INTENTIONALLY BLANK

1. Introduction

Calving of icebergs at the tidewater glacier fronts is a component of the regular mass loss from glaciers and ice sheets in Arctic regions (Dierking & Wesche, 2014). The Newfoundland and Labrador region can have hazardous environmental conditions that threaten exposed human-made structures due to extreme ice conditions. This area experiences thousands of icebergs and a large amount of sea ice every year.

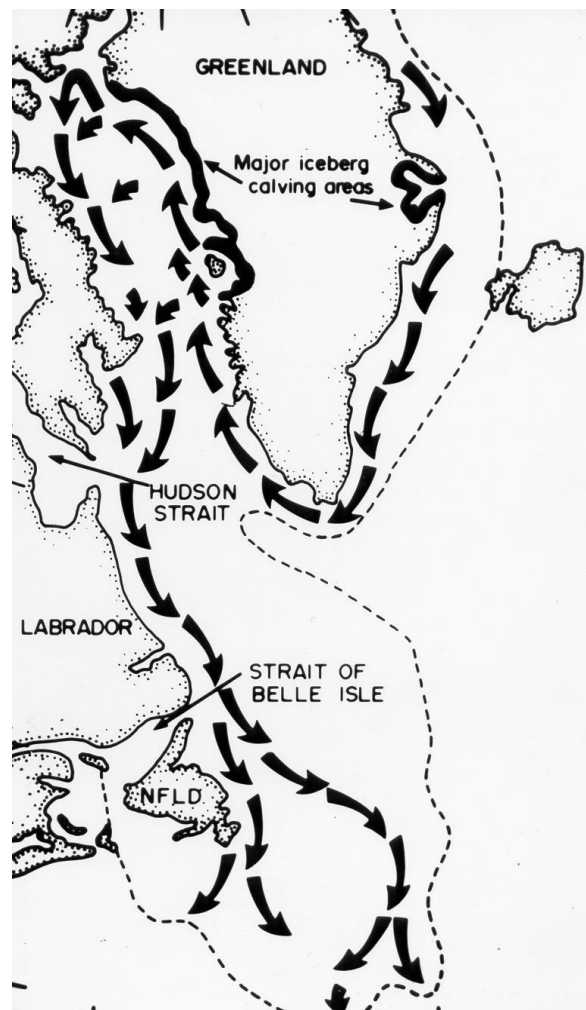


Figure 1.1: Iceberg's journey from Greenland to the Grand Banks of Newfoundland and Labrador (figure courtesy of C-CORE)

Greenland is the birthplace of most of the icebergs that frequent the coastline of eastern Canada. Icebergs, unlike sea ice, originate from the land, specifically from glaciers. When snowfall exceeds ablation, over time the snow accumulates and compresses to form ice. This ice then flows from higher altitude regions to sea level. The glacier interface at the ocean is constantly exposed to tides and sea level fluctuation that cause large pieces of ice to calve (Ulaby et al., 2014). These icebergs make their way to the Grand Banks over many freezes and thaw seasons (shown in Figure 1.1). Over the winter, sea ice and cold weather conditions protect icebergs from degradation as they drift south through the Baffin Bay and the Davis Strait. When the sea ice starts to melt in the spring, icebergs break away and it is then that they become a hazard to shipping and marine operations. However, once free from the sea ice, icebergs degrade quickly due to weathering from the ocean, rains, wind and temperature.

A means of surveilling icebergs while they are drifting south with the sea ice pack is compelling because it would allow marine operators to determine the number of icebergs that may become threats once they break away from the pack. This study is equally important to weather forecasters to set the initial conditions of icebergs in drift models to estimate the size and spatial distribution of icebergs breaking up. Satellite synthetic aperture radar (SAR) is one such solution, due to its wide areal coverage, day and night and all-weather acquisition capabilities. SAR is also the *de facto* standard for the monitoring of ice in extreme northern and southern regions. SAR has become a standard for monitoring of icebergs (see, for example Power et al. 2001; Lane et al. 2002; Howell et al. 2008; Wesche & Dierking 2012) and is presently used by the Canadian Ice Service

(CIS), the International Ice Patrol and the Danish Meteorological Institute for iceberg surveillance.

Icebergs manifest themselves as bright echoes against the darker ocean backscatter and the detection of icebergs in SAR can generally be accomplished using an adaptive threshold technique known as the constant false alarm rate (CFAR) (Skolnik, 2008). Nonetheless, the detection of icebergs within the pack is difficult because SAR backscatter from sea ice can be similar to that of icebergs. Standard CFAR techniques can also produce large numbers of false alarms when applied to sea ice regions. Therefore, SAR detection of icebergs in sea ice is fairly challenging.

New features in recent and upcoming satellite SAR missions promise to lead to improved capabilities for iceberg and sea ice monitoring both on the Grand Banks and in Arctic and subarctic regions. The type of sea ice in which icebergs are present play a role in SAR backscatter and in the context of analysis and detection of icebergs (Dierking & Wesche, 2014). The ice surface characteristics have a strong influence on radar intensity. There are many different types of sea ice, based on their thermodynamic and geophysical evolution throughout the seasons. Dierking & Wesche (2014) state that the potential of SAR remote sensing for iceberg detection depends on several factors: i) physical properties of icebergs such as size, shape and structure ii) SAR sensor specific properties such as incident angle, frequency band, resolution and polarization; iii) geophysical parameters such as winds, sea state, surface currents and season and iv) the backscatter of the surrounding sea ice or open water. Since space borne SAR systems can image the ocean and their sea ice regions

independent of light and cloud conditions, their potential for iceberg monitoring has been extensively investigated.

1.1 Purpose of the Study

The purpose of this research is to investigate the comparative characteristics of icebergs surrounded by sea ice and open water in SAR images. The SAR response from icebergs is generally complicated compared to other natural surfaces due to the geometric shapes of icebergs, the composition of the iceberg glacial ice and the presence or absence of meltwater on the surface of the iceberg. In addition, minor variations of temperature, wind speed and direction, SAR incident angle and the line of sight direction of the satellite can affect the results. Thus, iceberg polarimetric response varies by a significant number of parameters. Therefore, further study of iceberg polarimetric response in different conditions is important to optimize the surveillance of icebergs and enhance iceberg detection in sea ice. The main objective of this study is to determine the variability of the SAR response of icebergs in various aspects. In particular, the variability of the polarimetric response of icebergs is studied and a comparison is made between the SAR response in open water and in sea ice. The results obtained from this study may be used in other studies, such as enhanced detection and automatic iceberg discrimination (from other targets) using a machine learning approach.

The present state of the art in SAR-based vessel and iceberg discrimination is the use of machine learning to train algorithms to distinguish between vessel and iceberg backscatter (for example (Bentes, Frost, Velotto, & Tings, 2016; C-CORE, 2012; C-CORE, 2016;

Howell et al., 2004; Howell et al., 2006; Howell, 2008; Howell, Bobby, Power, Randell, & Parsons, 2012)). Several of the authors have been involved in efforts to develop ship and iceberg classifier in different types of SAR imagery, starting initially with RADARSAT-1 (unpublished) and then to ENVISAT ASAR (Howell et al., 2004; Howell et al., 2006), RADARSAT-2 (C-CORE, 2012; Howell, 2008) and TerraSAR-X (Howell et al., 2012). The most recent efforts (C-CORE, 2016) deal with discriminators trained for simulated data from RADARSAT Constellation Mission, showing the benefits of compact polarimetry for target discrimination.

2. Literature Review

This chapter provides a detailed description of literature of remote sensing fundamentals related to target (iceberg, sea ice) detection and discrimination using SAR data. Included here is a summary of radar theory relevant to iceberg, sea ice and ocean response, SAR image processing and polarimetric decomposition techniques. In addition, background information is provided on the statistical hypothetical tests that have been used later to compare and contrast iceberg backscatter.

2.1 Fundamentals of SAR

This section represents a few concepts of SAR imaging techniques that are relevant to this study. Basic knowledge about SAR is presented, including SAR image acquisition techniques, SAR ocean target response, and the potential of SAR data to detect icebergs.

According to Lee & Pottier (2009), a radar system performs three primary functions for imaging. First, it transmits microwave pulses towards a target. Then it receives a return portion of the transmitted signal after the interaction with the target. Finally, by observing the strength, temporal behavior and time delay of the received signal, the information about the target can be deduced.

Figure 2.1 shows a simple illustration of radar imaging. A radar sensor operates by transmitting microwave signals towards the earth's surface in a direction perpendicular to the flight path of the platform. By measuring the time delay between the transmission of a pulse and the reception of the backscattered echo from different targets, their distances

from the radar and the location can be determined (Lee & Pottier, 2009). As the sensor platform moves forward, recording and processing of the backscattered signal build up a two-dimensional image of the surface. Radar transmissions of microwaves are sensitive to a geometric shape, surface roughness and moisture contents.

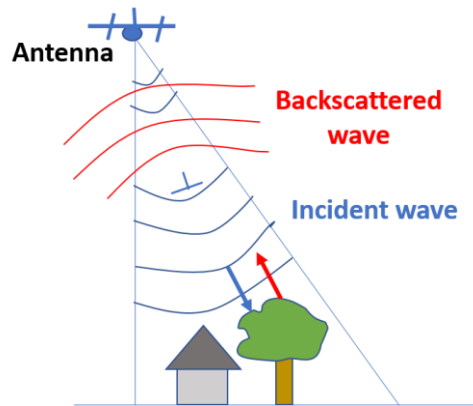


Figure 2.1 Basic radar imaging

2.1.1 Synthetic Aperture Radar (SAR)

A SAR system combines radar and signal processing units to form high resolution backscatter images (Ulaby et al., 2014). SAR systems take advantage of the long-range propagation characteristics of radar signals and the complex information processing capability of modern digital electronics to provide high resolution imagery. SAR sensors are an active sensor and are an important tool for the surveillance of icebergs, sea ice, and vessels. SAR data are used in many sectors such as ice services, defense, ocean and forestry, oil and gas and a variety of other sectors. Two of the most important factors behind the reliability of SAR are its capability of imaging day and night and that is relatively unaffected by weather conditions. Besides these acquisition capabilities, other advantages

of the SAR image are its sensitivity to geometric shape, surface roughness, moisture content, and partial penetration through the objects. Thus, the backscatter from different targets varies and it becomes possible to differentiate between certain classes of targets. Basically, SAR is based on the movement of the radar antenna over a stationary target (Ulaby et al., 2014). The general procedure of SAR imaging will be described in the following section.

2.1.2 SAR imaging

Generally speaking, SAR is a side looking sensor and in the case of space borne SAR, the synthetic aperture is formed by the movement of SAR along its orbit (Ulaby et al., 2014). Figure 2.2 below is an illustration of a SAR imaging system. SAR is a form of radar which is used to generate two-dimensional (2D) images. The SAR antenna directs energy over quite a broad beam, which defines the swath width of the image.

One dimension is a range (or cross track) and is a measure of the LOS distance from the radar to the target. Range measurement and resolution are achieved in SAR where the range is determined by measuring the time from transmission of a pulse to receiving the echo from a target and, in the simplest SAR, range resolution is determined by the transmitted pulse width, i.e., narrow pulses yield fine range resolution. The direction perpendicular to the flight path is referred to as the range direction. The SAR transmits the energy in the form of chirp pulses to provide resolution in the range direction. The other dimension is called azimuth (or along the track) and is perpendicular to the range. The antenna beam

parallels to the platform motion in the direction along the flight path is called the azimuth direction (Lee & Pottier, 2009).

The synthetic aperture formed by the flight path results in a very narrow beam and provides the resolution in the azimuth direction. Slant range resolution and ground range resolution are independent of the altitude of the platform. The SAR sensor operates by transmitting microwaves towards the earth's surface in a direction perpendicular to the flight path of the platform. By measuring the time delay between the transmission of a pulse and the reception of the backscattered echo from the targets, the distance between targets and sensor and their location can be determined (Lee & Pottier, 2009). As the sensor platform moves forward, recording and processing of the backscattered signal form a two-dimensional image of the surface. So, basically, SAR image is a record of the amount of power backscatter re-radiated from the target.

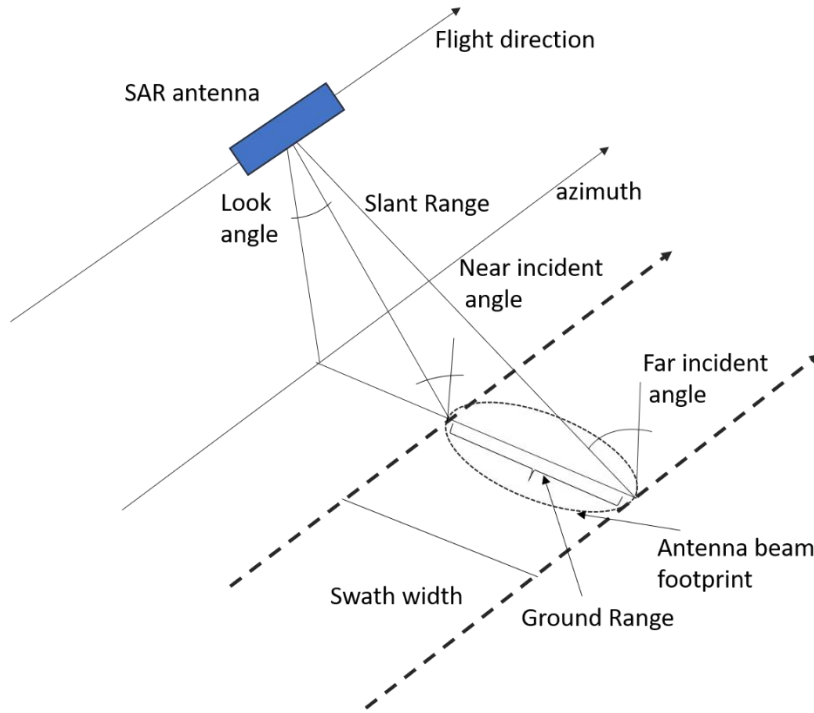


Figure 2.2: SAR imaging geometry [adapted from Lee & Pottier (2009)]

To provide resolution in the range direction, radar transmits signal in pulse form rather than continuous signal. In radar systems, the fundamental distance measure, which is referred to as the slant range resolution R_s , is given by

$$R_s = c\tau/2 \quad (2.1)$$

And the ground range resolution, R_g is given by

$$R_g = c\tau/2\sin\theta \quad (2.2)$$

where the c is the velocity of light, τ is the time width of the pulse transmission to scatter reception and θ is the incident angle. The ground range resolution is dependent on the incident angle. The incident angle close to near swath is the near incident angle and far

swath is the far incident angle. The factor of 2 accounts for the two-way travel of the pulse energy. One of the most useful models for describing radar performance is the radar range equation. The radar equation gives the received signal power P_r of the scattering from an object as

$$P_r = P_t G_t \sigma A_e / (4\pi)^2 R^4 \quad (2.3)$$

where P_t is the power radiated from the antenna in watts, G_t is antenna gain, σ is the radar cross section, R is the sensor-target distance, A_e is the effective aperture area and

$$A_e = G_t \lambda^2 / 4\pi \quad (2.4)$$

The radar cross section measures the power that a target extracts from the power density of the incoming wave. It is given by

$$\sigma = 4\pi R^2 |E_r|^2 / |E_i|^2 \quad (2.5)$$

Where, E_r is the energy of the electric field scattered from the target and E_i is the energy of the electric field incident on the target. The radar cross-section is normalized with respect to radar resolution by taking the fraction of σ to the area of the image sample spacing (m^2). Thus, the normalized radar cross-section or sigma naught (σ^0) is a unitless ratio of area. The normalization reference for the radar-cross section is a perfectly conducting sphere, and thus a target having a $\sigma^0 = 1$ will have the same strength reflection coming from that image sample as a sphere with a cross-sectional area of $1 m^2$. Sigma naught is also called radar cross-section per unit area (Ulaby et al., 2014).

2.1.3 SAR Polarization

SAR transmits the electromagnetic wave to capture an image. According to Ulaby et al. (2014), electromagnetic wave consists of oscillating electric and magnetic fields which are perpendicular to one another and perpendicular to the direction of propagation. However, polarization is an important property when discussing electromagnetic wave propagation and SAR backscatter. Polarization refers to the alignment and regularity of the electric field component of the wave, in a plane perpendicular to the direction of propagation.

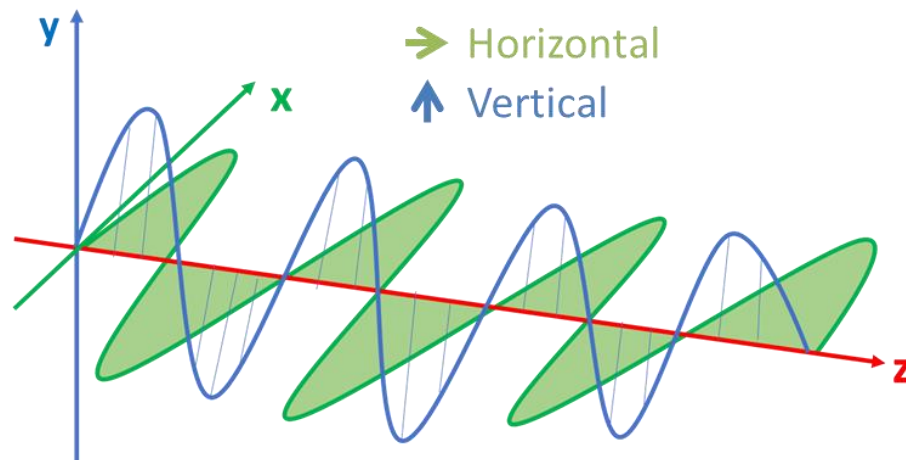


Figure 2.3 Horizontal and vertical polarization

Figure 2.3 shows the different states of polarization. A wave is horizontally polarized when its electric field component is in the plane perpendicular to the plane of the incident (in the direction of the x-axis, shown in green colour). The wave is vertically polarized when its electric field component is in the plane of the incident (in the direction of the y-axis, shown in blue color). The z-axis represents the direction of wave propagation. There are four kinds of combinations of polarization modes. They are:

- HH- Horizontal transmit, Horizontal receive
- HV- Horizontal transmit, Vertical receive
- VH- Vertical transmit, Horizontal receive
- VV- Vertical transmit, Vertical receive

HH and VV polarization combinations are referred to as co-polarization. For both channels, the polarization of the transmitting and receiving signal is the same. On the other hand, HV and VH are known as cross-polarization, as the polarization of the transmitting and receiving signal are orthogonal to each another. Spaceborne SAR generally has four kinds of polarization, including:

- Single polarization (HH or HV)
- Dual polarization (HH & HV or VH & VV or HH & VV) and
- Fully (quad) polarimetric polarization (HH, HV, VH, and VV)

RADARSAT-2 can provide images having any of these four polarimetric polarization combinations except HH, VV. The RADARSAT-2 images with a fine quad polarization combination have been used in this study. The information obtained from each polarimetric channel together provides a scattering matrix. The matrix represents a complex value containing both amplitude and phase of each polarization channel. The structure of the scattering matrix is shown in equation 2.6,

$$\mathbf{S} = \begin{bmatrix} S_{HH} & S_{HV} \\ S_{VH} & S_{VV} \end{bmatrix} \quad (2.6)$$

The scattering matrix is the received output of radar. Further processing of the scattering matrix is the next step for analysis of SAR data.

Another two formations of scattering matrix named covariance and coherency have been used in this study to implement some polarimetric decomposition. The covariance matrix is defined on the lexicographic vector basis:

$$\mathbf{C} = \begin{bmatrix} \langle S_{HH}S_{HH}^* \rangle & \langle S_{HH}S_{HV}^* \rangle & \langle S_{HH}S_{VH}^* \rangle & \langle S_{HH}S_{VV}^* \rangle \\ \langle S_{HV}S_{HH}^* \rangle & \langle S_{HV}S_{HV}^* \rangle & \langle S_{HV}S_{VH}^* \rangle & \langle S_{HV}S_{VV}^* \rangle \\ \langle S_{VH}S_{HH}^* \rangle & \langle S_{VH}S_{HV}^* \rangle & \langle S_{VH}S_{VH}^* \rangle & \langle S_{VH}S_{VV}^* \rangle \\ \langle S_{VV}S_{HH}^* \rangle & \langle S_{VV}S_{HV}^* \rangle & \langle S_{VV}S_{VH}^* \rangle & \langle S_{VV}S_{VV}^* \rangle \end{bmatrix}$$

$$\text{or, } \mathbf{C} = \begin{bmatrix} \langle |S_{HH}|^2 \rangle & \langle S_{HH}S_{HV}^* \rangle & \langle S_{HH}S_{VH}^* \rangle & \langle S_{HH}S_{VV}^* \rangle \\ \langle S_{HV}S_{HH}^* \rangle & \langle |S_{HV}|^2 \rangle & \langle S_{HV}S_{VH}^* \rangle & \langle S_{HV}S_{VV}^* \rangle \\ \langle S_{VH}S_{HH}^* \rangle & \langle S_{VH}S_{HV}^* \rangle & \langle |S_{VH}|^2 \rangle & \langle S_{VH}S_{VV}^* \rangle \\ \langle S_{VV}S_{HH}^* \rangle & \langle S_{VV}S_{HV}^* \rangle & \langle S_{VV}S_{VH}^* \rangle & \langle |S_{VV}|^2 \rangle \end{bmatrix} \quad (2.7)$$

Where, * is the symbol of complex conjugate and $\langle \rangle$ is the averaging operator. For reciprocity or monostatic case when $S_{HV}=S_{VH}$. Then,

$$\mathbf{C} = \begin{bmatrix} \langle |S_{HH}|^2 \rangle & \langle \sqrt{2}S_{HH}S_{HV}^* \rangle & \langle S_{HH}S_{VV}^* \rangle \\ \langle \sqrt{2}S_{HV}S_{HH}^* \rangle & \langle 2|S_{HV}|^2 \rangle & \langle \sqrt{2}S_{HV}S_{VV}^* \rangle \\ \langle S_{VV}S_{HH}^* \rangle & \langle \sqrt{2}S_{VV}S_{HV}^* \rangle & \langle |S_{VV}|^2 \rangle \end{bmatrix} \quad (2.8)$$

Another easier form of scattering matrix is coherency matrix, \mathbf{T} , which is defined on the Pauli basis and used to interpret the physical scattering mechanism of distributed targets.

$$\mathbf{T} = \frac{1}{2} \begin{bmatrix} \langle k_a k_a^* \rangle & \langle k_a k_b^* \rangle & \langle k_a k_c^* \rangle & \langle k_a k_d^* \rangle \\ \langle k_b k_a^* \rangle & \langle k_b k_b^* \rangle & \langle k_b k_c^* \rangle & \langle k_b k_d^* \rangle \\ \langle k_c k_a^* \rangle & \langle k_c k_b^* \rangle & \langle k_c k_c^* \rangle & \langle k_c k_d^* \rangle \\ \langle k_d k_a^* \rangle & \langle k_d k_b^* \rangle & \langle k_d k_c^* \rangle & \langle k_d k_d^* \rangle \end{bmatrix} \quad (2.9)$$

Whereas, k is pauli vector and

$$k_a = S_{HH} + S_{VV} ; k_b = S_{HH} - S_{VV} ; k_c = S_{HV} + S_{VH} ; k_d = j(S_{HV} - S_{VH}); \quad (2.10)$$

For monostatic case, when $S_{HV} = S_{VH}$, then the coherency matrix will be,

$$\mathbf{T} = \frac{1}{2} \begin{bmatrix} \langle (S_{HH} + S_{VV})(S_{HH}^* + S_{VV}^*) \rangle & \langle (S_{HH} + S_{VV})(S_{HH}^* - S_{VV}^*) \rangle & 2 \langle (S_{HH} + S_{VV})S_{HV}^* \rangle \\ \langle (S_{HH} - S_{VV})(S_{HH}^* + S_{VV}^*) \rangle & \langle (S_{HH} - S_{VV})(S_{HH}^* - S_{VV}^*) \rangle & 2 \langle (S_{HH} - S_{VV})S_{HV}^* \rangle \\ 2 \langle S_{HV}(S_{HH}^* + S_{VV}^*) \rangle & 2 \langle S_{HV}(S_{HH}^* - S_{VV}^*) \rangle & 4 \langle S_{HV}S_{HV}^* \rangle \end{bmatrix} \quad (2.11)$$

2.1.4 Ocean Response to SAR

SAR interaction with the ocean surface is quite complex. The ocean response to SAR is dependent on several factors related to the geometry and radar sensor parameters, as the ocean surface is dependent on the wind speed and direction, wave height and direction, atmospheric conditions and sea surface temperature (Ulaby et al., 2014). All these parameters affect the local surface roughness of the ocean upon which the SAR response is primarily dependent. Both the target and radar antenna parameters can influence radar power return.

The target parameters that affect the radar backscatter include geometric shape, surface roughness and the dielectric constant of the target. The important sensor parameters include wavelength, incident angle, look direction and polarization of the wave. Wind is a strong factor when considering ocean backscatter, since it contributes significantly to the ocean surface roughness. Ocean surface roughness increases with the increase of wind speed. In

the absence of wind, the ocean surface will be smooth and specular. Different sea states are defined as a code number in the World Meteorological Organization (WMO) sea state code (Ulaby et al., 2014). For example, the WMO code is 0 when the sea state is calm as a mirror and the wave height is 0 cm, the code is 10 during a storm when the wave height is very high. The ocean condition or sea states is therefore an important factor in detecting targets, including vessels and icebergs. Strong backscatter from the ocean surface due to high wind speed decreases the contrast between bright target returns and the ocean background and in extreme cases, can completely mask target backscatter, rendering detection difficult or impossible. The intensity value of ocean wave increases with the increase of wind speed but decreases as a function of incidence angle. It is also apparent that the σ^0 C-band VV polarization is greater than HH for all wind speeds, directions, and incidence angles. Moreover, HV polarization generally has a much lower contribution from wind or sea states.

2.1.5 Icebergs and Sea Ice Response to SAR

Iceberg backscatter is a complex phenomenon. Generally, backscatter from an iceberg arises from three mechanisms, including surface scattering, dihedral or double bounce and volume scattering (Freeman & Durden, 1998). Surface scattering or odd bounce is reflected from the top surface of the iceberg. Dihedral scattering is reflected twice from the corner reflector made by the ocean-iceberg or sea ice-iceberg interface. Dihedral scattering mostly depends on the size and shape of the iceberg. Large icebergs tend to give higher double bounce scattering compared to smaller icebergs, as a large iceberg creates a comparatively strong corner reflector with water/sea ice surface. Volume scattering is the reflection due

to multiple scattering that occurs inside the icebergs. Icebergs composed of glacial ice have air bubbles inside them. When the incident wave penetrates through the top surface of an iceberg, multiple reflections occur due to the air bubbles. The penetration energy is scattered by dielectric discontinuity (change in medium). The orientation of the local surface roughness is a contributing factor in the total backscatter intensity (Ulaby et al., 2014). Figure 2.4 represents the general backscattering mechanism for icebergs. The reflected wave indicated in blue colour represents surface scattering, red represents double bounce scattering and the green is volume scattering. For iceberg in open water, some double bounce reflection might add the backscatter from iceberg-open water interaction.

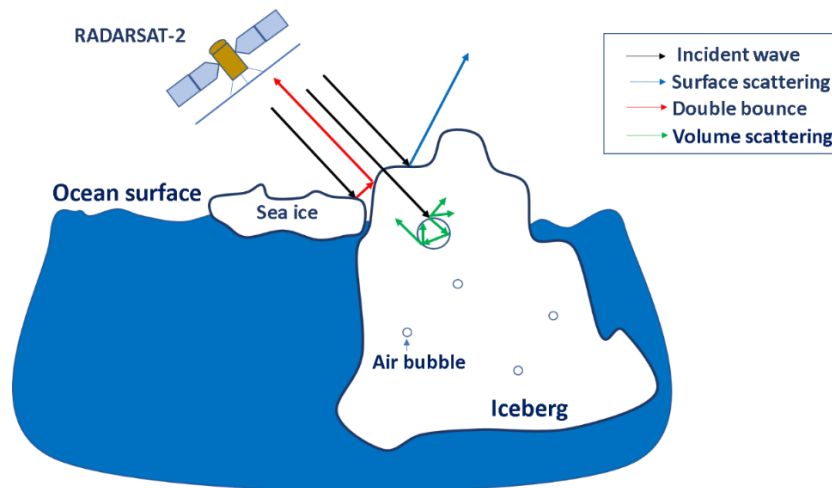


Figure 2.4: Backscatter mechanism of iceberg and sea ice

The comparative analysis is shown in two aspects: icebergs surrounded by differing clutter and icebergs from different geographical locations. This section describes the details of the parameters and tests that were used for statistical analysis. The comparison of the intensity value of co (HH) and cross (HV) polarization channels is presented in this section. The

four types of decomposition techniques described earlier (i.e., Pauli, Freeman-Durden, van Zyl, Yamaguchi and Cloud-Pottier) have been used for the analysis here for discrimination. Each decomposition accounts for the three backscatter mechanisms described above except Yamaguchi which also includes the helix scattering component. The following sections describe their application.

2.2 Polarimetric Decomposition

When the full scattering matrix (i.e., four channels with inter-channel phase) is available for analysis, so-called polarimetric decompositions can be performed. The primary purpose of these decompositions is to use the scattering matrix to express the SAR response in terms of elemental scatterer that better describes the physical nature of the scatter. These decompositions are used to determine the nature of iceberg scattering in the analysis presented in later chapters of this thesis.

To perform a polarimetric decomposition, the SAR image, in form of a scattering matrix, is transformed into another matrix (either the covariance, coherency) and then decomposed into individual scatterers i.e., surface, double bounce or volume scattering. Decomposition facilitates the interpretation of the scattering process. There are several kinds of decomposition techniques that can be used to analyze SAR data. Figure 2.5 shows the different kinds of decomposition techniques. Basically, decompositions can be categorized into coherent and incoherent decompositions.

The objective of the coherent decomposition is to express the scattering matrix as a combination of the scattering responses of simpler objects. Incoherent decomposition

characterizes the distributed scatterer (urban areas, vegetation, cropland). However, the scattering matrix is only able to characterize the pure scatterer. Distributed scatterer is characterized by the covariance or coherency matrix. Ultimately, the objective of the decompositions is to express the measured scattering matrix in terms of the scattering response of the simpler or distributed targets (Lee & Pottier, 2009).

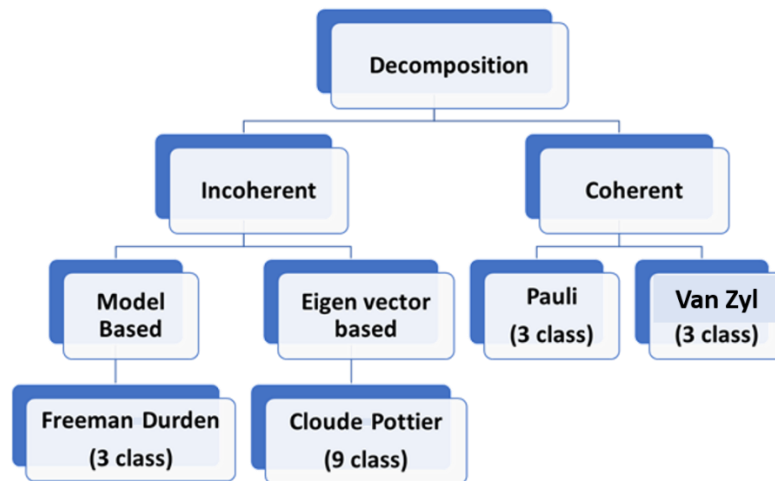


Figure 2.5 Types of Decompositions

In this study, the decomposition techniques that have been used include Pauli, Freeman-Durden, van Zyl, Yamaguchi and Cloud-Pottier decompositions. Pauli decomposition is considered as an appropriate decomposition for a point or single targets. Another unsupervised classification algorithm named van Zyl decomposition has been applied, which uses the covariance matrix and decomposes the matrix into three dominant scatterers (surface, double bounce, volume). A comparative study has indicated that van Zyl decomposition gives better classification accuracy than other decomposition techniques (Turkar & Rao, 2011). Cloud-Pottier (Cloude & Pottier, 1997) and Freeman-Durden

(Freeman & Durden, 1998) decompositions are commonly cited and applied for agricultural and land classification applications. The Freeman-Durden decomposition is extensively used to classify the scattering of vegetation and urban areas. van Zyl (2011) found that the Freeman-Durden decomposition overestimates the volume scattering from distributed targets like vegetation when the SAR band is L-band. L-band SAR wavelengths (nominally 23.6 cm) are higher than C-band (nominally 5.5 cm), and so L-band is better able to penetrate through distributed targets relative to C-band. In this study, Freeman-Durden is assumed applicable for the analysis of iceberg targets. The Yamaguchi decomposition is also an extensively used decomposition and is known to be better than Freeman-Durden for partitioning of the dipole and dihedral scatterers.

2.2.1 Pauli Decomposition

Coherent decompositions were developed to completely characterize polarized scattered waves for which fully polarimetric information is contained in the scattering matrix $[S]$. The Pauli decomposition is one of the extensively used coherent decompositions (Lee & Pottier, 2009). The Pauli decomposition transforms polarimetric data into a set of Pauli basis matrices $\{[S]_a, [S]_b, [S]_c, [S]_d\}$ (Lee & Pottier, 2009), where

$$\begin{aligned}
 [S]_a &= \frac{1}{\sqrt{2}} \begin{bmatrix} 1 & 0 \\ 0 & 1 \end{bmatrix}, & [S]_b &= \frac{1}{\sqrt{2}} \begin{bmatrix} 1 & 0 \\ 0 & -1 \end{bmatrix}, \\
 [S]_c &= \frac{1}{\sqrt{2}} \begin{bmatrix} 0 & 1 \\ 1 & 0 \end{bmatrix}, & [S]_d &= \frac{1}{\sqrt{2}} \begin{bmatrix} 0 & -j \\ j & 0 \end{bmatrix},
 \end{aligned}$$

A monostatic case, where reciprocity is assumed ($S_{HV} = S_{VH}$), is easier for illustration as S_{HV} and S_{VH} is generally same for monostatic case (Lee & Pottier, 2009). Thus, the Pauli basis will reduce to $\{[S]_a, [S]_b, [S]_c\}$, whereby

$$\mathbf{S} = \begin{bmatrix} S_{HH} & S_{HV} \\ S_{VH} & S_{VV} \end{bmatrix} = \alpha[S]_a + \beta[S]_b + \gamma[S]_c. \quad (2.12)$$

In this equation, α (power contribution due to surface scattering):

$$S_{HH} + S_{VV}/\sqrt{2} \quad (2.13)$$

β (power contribution due to double bounce):

$$S_{HH} - S_{VV}/\sqrt{2} \quad (2.14)$$

γ (power contribution due to volume scattering):

$$\sqrt{2}S_{HV} \quad (2.15)$$

The total power contribution for Pauli decomposition is calculated from equations (2.13), (2.14) and (2.15)

$$P_{pauli} = |\alpha|^2 + |\beta|^2 + |\gamma|^2 = |S_{HH}|^2 + 2|S_{HV}|^2 + |S_{VV}|^2 \quad (2.16)$$

$[S]_a$ represents single or odd bounce scattering. The complex coefficient, α , characterizes the contribution of $[S]_a$ to $[S]$ and $|\alpha|^2$ represents the power backscattered from a single or odd bounce. The second matrix, $[S]_b$, expresses the scattering mechanism of a dihedral oriented at 0 degrees, which is basically double or even bounce scattering. β is the complex

coefficient that characterizes $[S]_b$ and $|\beta|^2$ is the power contribution of even bounce scattering to $[S]$. The third matrix, $[S]_c$, represents the scattering mechanism of a dihedral oriented at 45° , which is interpreted as volume or diffuse scattering. The complex coefficient γ characterizes volume scattering, whereas $|\gamma|^2$ quantifies the power contributions of volume scattering to the total scattering matrix $[S]$.

2.2.2 van Zyl Decomposition

Jacob van Zyl (1989) proposed an algorithm to classify SAR image pixels into simple classes of scattering such as even and odd number of reflections and diffuse scattering. The purpose of this decomposition is to group pixels in a general known class by measuring dominant scattering behavior instead of quantifying the power contribution of pixels. Later, van Zyl (2008) proposed an improved version of this decomposition. van Zyl (2008) assumes that the reflection symmetry hypothesis is established and the correlation between co-polarized channels is zero. The assumption is generally true in case of natural media such as soil and forest. With such an assumption, the averaged covariance matrix can be given analytically and the covariance matrix can be expressed in the following manner.

$$\mathbf{C}_3 = A_1 \begin{bmatrix} |\alpha|^2 & 0 & \alpha \\ 0 & 0 & 0 \\ \alpha^* & 0 & 1 \end{bmatrix} + A_2 \begin{bmatrix} |\beta|^2 & 0 & \beta \\ 0 & 0 & 0 \\ \beta^* & 0 & 1 \end{bmatrix} + A_3 \begin{bmatrix} 0 & 0 & 0 \\ 0 & 1 & 0 \\ 0 & 0 & 0 \end{bmatrix} \quad (2.17)$$

where, \mathbf{C}_3 is the average covariance matrix. The van Zyl decomposition thus shows that the first two eigenvectors represent equivalent scattering matrix that can be interpreted in terms of odd and even number of reflections. The 2008 version of van Zyl decomposition

has been implemented in this study. There is a more recent version of this decomposition available (van Zyl (2011)), but that one is not implemented in this thesis as no software/tool/code have been found for this version.

2.2.3 Freeman-Durden Decomposition

A scattering matrix \mathbf{S} can only characterize coherent or pure scatterer. It cannot be employed to characterize distributed targets (Lee & Pottier, 2009). That is why incoherent decompositions are important to characterize distributed scattering. The Freeman-Durden decomposition is one kind of incoherent decomposition that describes the scattering as three physical mechanisms (Freeman & Durden, 1998), including:

- surface or single bounce scattering modeled by Bragg or rough surface;
- double bounce scattering modeled by dihedral corner reflector; and
- volume scattering, such as from forest area.

According to this model, the total measured power P is expressed as total power:

$$P = \langle |S_{HH}|^2 \rangle + \langle |S_{VV}|^2 \rangle + \langle |S_{HV}|^2 \rangle = P_s + P_d + P_v \quad (2.18)$$

where P_s = power contribution due to surface scattering; P_d = power contribution due to double bounce and P_v = power contribution due to volume scattering. According to Freeman & Durden (1998), P is four times the usual expression of total power.

These three components can be calculated from the covariance matrix. The following series of intermediate parameters are needed to derive the theory.

$$P_s = f_s(1 + |\beta|^2) \quad (2.19)$$

$$P_d = f_d(1 + |\alpha|^2) \quad (2.20)$$

$$P_v = 8f_v/3 \quad (2.21)$$

The value of equation [2.19, 2.20, 2.21] can be calculated from the following equations of the scattering matrix

$$\langle |S_{HH}|^2 \rangle = f_s|\beta|^2 + f_d|\alpha|^2 + f_v \quad (2.22)$$

$$\langle |S_{VV}|^2 \rangle = f_s + f_d + f_v \quad (2.23)$$

$$\langle S_{HH}S_{VV}^* \rangle = f_s\beta + f_d\alpha + f_v/3 \quad (2.24)$$

$$\langle |S_{HV}|^2 \rangle = f_v/3 \quad (2.25)$$

From these four equations, $f_s, f_d, f_v, \alpha, \beta$ can be calculated and finally the individual power contribution P_s, P_d, P_v can be obtained. But there are 4 equations and 5 unknown parameters. To solve these 4 equations, the value of α, β are assumed depending on the dominant scattering mechanism as follows:

- When, $Re\{S_{HH}S_{VV}^*\} \geq 0$, surface scattering is dominant and $\alpha = -1$
- When, $Re\{S_{HH}S_{VV}^*\} < 0$, then double bounce is dominant and $\beta = 1$

Figure 2.6 shows the flow chart to derive these 4 equations from the covariance matrix.

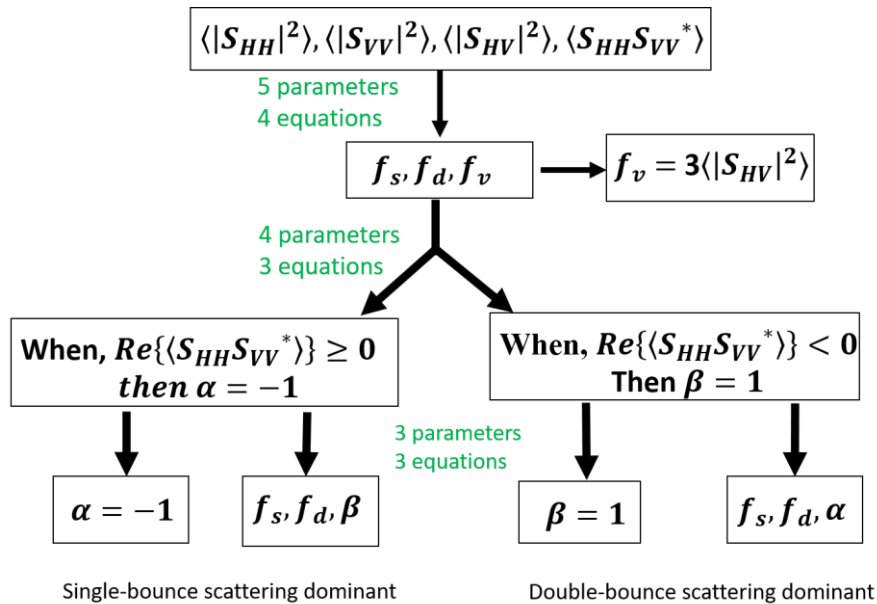


Figure 2.6: Freeman-Durden decomposition (adapted from Lee & Pottier (2009))

2.2.4 Yamaguchi Decomposition

The three component Freeman-Durden decomposition can be successfully applied to SAR observations under the reflection symmetry assumption. However, there are areas in a SAR image where the reflection symmetry condition does not necessarily hold. Yamaguchi et al. proposed in 2005, a four-component scattering model by introducing an additional term corresponding to non-reflection symmetric cases. The fourth component introduced is equivalent to a helix scattering power. This helix scattering power term appears in heterogeneous areas (complicated shaped targets or man-made structures) that disappear for almost all natural distributed scattering. Therefore, Yamaguchi decomposition models the covariance matrix as a four scattering mechanism: surface, double-bounce, volume and helix scatter components.

2.2.5 Cloud-Pottier Decomposition

Cloud-Pottier decomposition is an eigenvector based decomposition. Eigenvector based decompositions are based on the eigenvalues of the coherency matrix typically (Cloude & Pottier, 1996). Cloud-Pottier decomposition is also known as $H/A/\alpha$ decomposition where H is denoted as scattering entropy, A as anisotropy and α as the alpha angle. The entropy, anisotropy and alpha angle all can be calculated from the eigenvalue of the coherency matrix \mathbf{T} (Cloude & Pottier, 1996) by using the following equation

$$\text{Entropy, } H = -\sum_{i=1}^3 P_i \log_3(P_i) \quad (2.26)$$

where

- P_i is the probability of the eigenvalue λ_i and $P_i = \lambda_i / \sum_{k=1}^3 \lambda_k$;
- $\lambda = [\lambda_1 \lambda_2 \lambda_3]$ = Eigen vector of coherency matrix \mathbf{T}

$$\text{Anisotropy, } A = (\lambda_2 - \lambda_3) / (\lambda_2 + \lambda_3); \quad (2.27)$$

$$\text{alpha angle, } \alpha = \sum_{i=1}^3 P_i \alpha_i \quad (2.28)$$

The degree of randomness of the target scattering is represented by H . The value of H is between 0 to 1.

When entropy $H = 0$, the scattering from the target corresponds to a pure target or canonical objects. When $H = 1$, scattering comes from three pure targets. If the value of H is between $0 < H < 1$, then the scattering mechanism is represented by three pure targets but weighted by the corresponding eigenvalues.

Anisotropy, A measures the relative importance of the second and third Eigenvalue of the eigenvector. From a practical point of view, anisotropy can be a source of discrimination only when $H > 0.7$, as for higher entropy, the second and third eigenvalues are highly affected by noise (Lee & Pottier, 2009).

The value of alpha angle provides information about the dominant scattering mechanism. When the alpha angle is 0° , scattering corresponds to single bounce scattering. The scattering mechanism is due to volume scattering when alpha is 45° and it corresponds to double bounce when alpha is 90° (Lee & Pottier, 2009).

As the anisotropy value is noisy, by using the value of H and alpha, the SAR image can be classified into nine zones for better understanding. The H/α plane containing all zones of scattering type is shown in Figure 2.7 below.

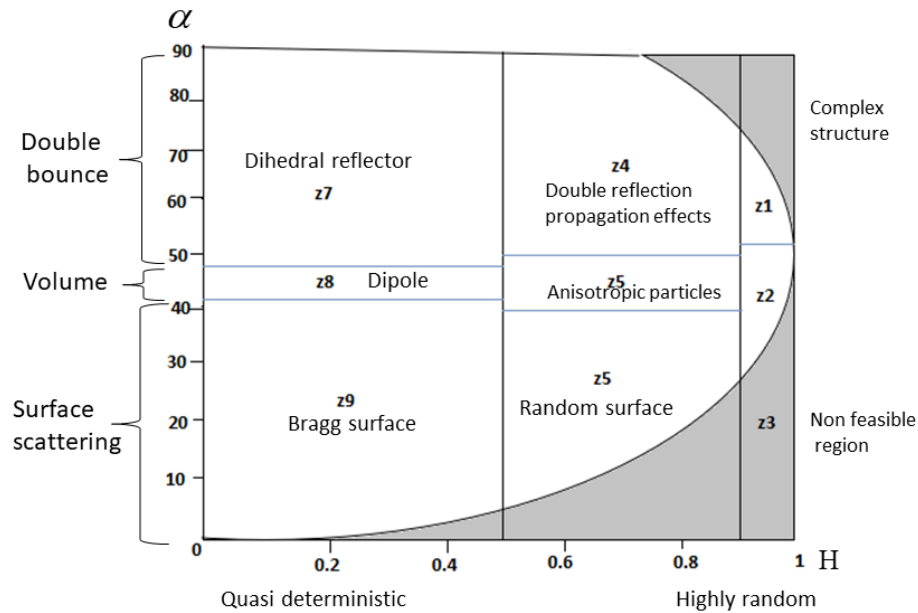


Figure 2.7: H/α plane; adapted from Lee & Pottier (2009)

2.3 Statistical Tests

This comparative study requires a statistical test to quantify and compare the backscatter of iceberg samples. Statistical tests often imply the calculation of a specific number called a statistic, which has a theoretical probability distribution. A statistical or hypothesis test is a premise that is used to establish a quantitative decision about a particular sample or to compare statistics between several samples. A hypothesis is formed based on the sample sets, and statistical tests are performed to test that hypothesis. Decisions are made based on parameters such as the mean and variance of the samples (Eadie et al., 1971). Generally, the hypothesis is called the null hypothesis and is represented as H_0 . An alternate hypothesis, H_a , is also formed that becomes true if the null hypothesis is rejected. The null and alternate hypotheses are thus mutually exclusive. When comparing two samples (i.e., two sets of data), the most popular null hypothesis is that there is no significant difference between the two samples, meaning in general that their corresponding means are equal:

$$H_0: \mu_1 = \mu_2$$

The alternate hypothesis is that the means are not equal; there are generally three common alternate hypotheses:

$$H_a: \mu_1 \neq \mu_2, H_a: \mu_1 < \mu_2, \text{ or } H_a: \mu_1 > \mu_2.$$

When a statistical test is performed, it either accepts or rejects the null hypothesis on the basis of a pre-specified significance level, δ . If the null hypothesis is accepted at that significance level, it means that the samples are not statistically different, whereby their

means are essentially equal at the pre-defined significance level. But when H_0 is rejected, the alternate hypothesis H_a is accepted, which means the samples are statistically different at the specified significance level, δ .

Statistical tests are of various kinds depending on the study requirements. In this study, the Welch's T-test, has been used.

The Welch's T-test is an adaptation of the student's T-test and is a two-sample test that tests the hypothesis that two populations have equal means when the two samples have unequal variances and/or unequal sample sizes. The test performs the comparison by quantifying the means, the standard deviations and the number of samples in each group. The size of standard deviation highly influences the outcome of this test (Brown & Forsythe, 1974). The test evaluates a test statistic first by using the following equations:

$$t_{STAT} = (\bar{x}_1 - \bar{x}_2) / \sqrt{\frac{SD_1^2}{n_1} + \frac{SD_2^2}{n_2}} \quad (2.29)$$

where x_1 and x_2 is the mean of the first and second sample respectively, SD_1 and SD_2 are the standard deviations and n_1, n_2 are the sample sizes. From this, there is a necessity to calculate the critical value, which is the point on the test distribution that is compared to the test statistic to determine whether to accept or reject the null hypothesis. The critical value is the value of the test statistic at the confidence level established for statistical significance.

$$t_{CRIT} = t_{STAT} |_{\delta} \quad (2.30)$$

The critical value, t_{CRIT} , can be calculated from the degrees of freedom (DoF) (Eadie et al., 1971). DoF is a number that can be determined from the sample size (n). There are some conditions that are needed to be fulfilled by the sample sets before applying the T-test. The conditions are that both data sets should have a normal distribution and the sample size for both sets should be greater than 30.

The following sub-sections contain a short description of two kinds of T-tests and how they work.

2.3.1 Two Tail T-test

There are two kinds of T-test based on observation, including one tail and two tail T-test. In this study, both one tail and two tail T-test have been used. Since we will be evaluating different sets of data in this study, we will use so called two sample T-tests that evaluate two different sample sets.

In the case of two tail T-test, the degree of freedom (DoF) (Eadie et al., 1971) is:

$$DoF = \left(\frac{SD_1^2}{n_1} + \frac{SD_2^2}{n_2} \right)^2 / \left(\frac{SD_1^4}{n_1^2 d_1} + \frac{SD_2^4}{n_2^2 d_2} \right) \quad (2.31)$$

where, $d_1 = n_1 - 1$ and $d_2 = n_2 - 1$.

When the critical value, t_{CRIT} , is greater than the statistical test value, t_{STAT} , or alternately less than $-t_{STAT}$ when the critical value is negative, the null hypothesis cannot be rejected at the α significant level. When t_{CRIT} is less than t_{STAT} , or t_{CRIT} is greater than $-t_{STAT}$ for negative critical values, the null hypothesis will be rejected at the δ significant level. The

one-tailed test is associated with an alternative hypothesis for which the sign of the potential difference is known before running the experiment and the test.

The distribution of a sample is often a Gaussian. The Figure 2.8 below shows that tails are the extremes of the Gaussian. In order to obtain the p-value, the statistic computed out of the data is compared to the distribution under the null hypothesis. The further the statistic is from the center of the distribution (i.e., the closer it is to a tail), the more extreme the data are relative to data generated under the null hypothesis and thus the lower the p-value. Before gathering the data, if we don't know whether the computed statistic will be at the right tail or at the left tail under the alternative hypothesis, the two tail T-test are considered. We thus work with a two-tailed hypothesis. If the computed statistic is in one of the two grey areas, the p-value will be under the alpha threshold and thus the null hypothesis is rejected.

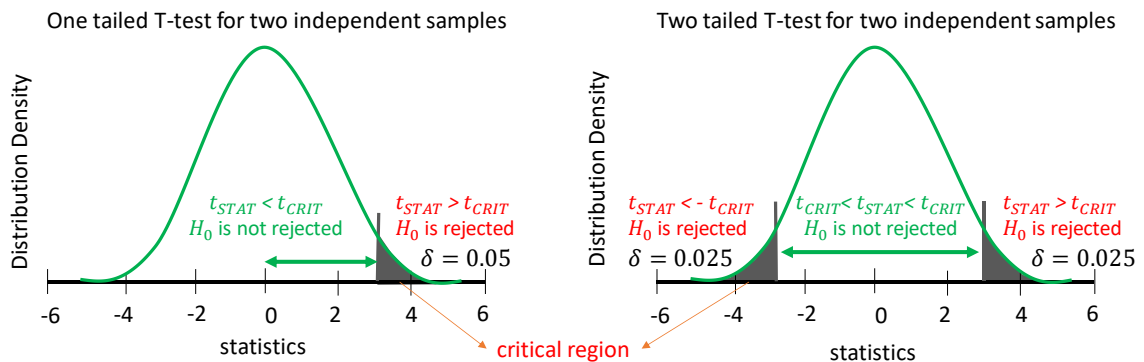


Figure 2.8: Visual illustration of the one tail and two tail tests; Left: one-tailed T-test (right sided); Right: two tailed T-test

2.3.2 One Tail T-test

The one tail T-test is quite similar to the two tail T-test. The exception is that the one tail T-test calculates the probability and the critical value in one direction. If we expect a specific tail under the alternative hypothesis, it is possible to choose a one-tailed hypothesis. If the computed statistic is under the grey area, the p-value will be under the alpha threshold and thus the null hypothesis is rejected. Figure 2.8 (left) shows the strategy of performing one tail T-test. When the t-statistics value is in the critical region, it rejects the null hypothesis.

2.4 Previous Work

As this thesis involves the study of iceberg detection in SAR imagery, this section provides a synopsis of previous work on this topic. There has been a significant amount of previous work related to iceberg detection in open water and sea ice in SAR imagery. The following is a collection of significant journals, books and conference papers that have contributed to the direction of this work.

2.4.1 Properties of Sea Ice and Icebergs

Ulaby et al. (2014) describes the properties of sea ice, icebergs and ocean winds, which is crucial to explaining the analytical results presented here. The formation of sea ice is complicated. The important factors that play a vital role in the formation of sea ice are the salinity and density of sea water, surface temperature and the depth of water. Generally, sea ice formation starts in shallow water near the coastline rather than in deep water. When the salinity density of water exceeds 24.7% and the temperature drops to -1.8°C , it starts

freezing. Then freezing continues depending on the environmental conditions, e.g., wind speed, ocean currents and waves and temperature (below 0°C). When the surface is calm and cooling is rapid, ice forms in small crystals known as frazil ice. Further, the star crystals grow rapidly and they form a uniform sheet of young ice. Their property changes rapidly and forms into different kinds of sea ice, such as first year ice, multiyear ice, summer ice and so on. As sea ice is a mixture of ice crystals, salt and air bubbles, it exhibits complex dielectric behavior. The penetration depth of radar signals in sea ice depends mostly on the radar frequency, sea ice type, dielectric property and the weather conditions. For example, penetration into a dry snow surface of sea ice in winter is much greater than for the summer ice because summer ice will have a melting surface that attenuates the radar signal. Thus, the scattering properties of sea ice have considerable seasonal variation.

The electromagnetic properties of icebergs are quite different from that sea ice. Icebergs are formed by the calving of large chunks of ice from glaciers. Glacier ice is formed from layers of accumulated snow and composed of freshwater ice. Icebergs come in a variety of sizes from extremely large (km range) to very small (a few meters). Large icebergs are often visible in SAR imagery, but small icebergs might be difficult to detect, depending on the spatial resolution of the SAR. Like sea ice, the backscatter from an iceberg also depends highly on the weather conditions and location.

2.4.2 C-CORE's Research on Iceberg Detection with SAR

There has been significant research conducted at C-CORE on the topic of iceberg detection. A subset of the papers that are available to the public is described below.

Power et al. (2001) investigated the capability of detecting icebergs using RADARSAT-1 (RS-1). This paper presents some validated results of iceberg detection using RS-1 data that were acquired at offshore locations in the Newfoundland sea. The authors describe a guard cell CFAR implementation, where the highest intensity pixels are excluded from the background intensity approximation via truncated statistics. This ensures that the ocean clutter measures are representative of the sea clutter alone. They showed that an incident angle of SAR greater than 35° can easily detect large and extra-large icebergs even in rough sea states, but in the case of medium and small icebergs, the probability of detection is lower. Statistics presented here show that wind speed has a substantial effect to detect iceberg.

Lane et al. (2002) investigated the iceberg detection performance of RS-1 SAR data. C-CORE validated the iceberg detection capability of RS-1 SAR and the validation process used over 50 RADARSAT-1 scenes in various modes including Wide2, Wide3, and ScanSAR NarrowB. To detect icebergs, several factors that affect the backscatter of SAR data, specifically sea state and incident angle, were taken into account. The increase of wind speed increases the ocean surface roughness as well as backscatter in SAR and the mean sea clutter increases, in general, with a decrease in incident angle. They used background clutter and the CFAR technique to determine the threshold value to separate the iceberg pixels from the background clutter.

Howell, Bobby, Power, Randel, & Parsons (2012) contributed to the improvement of the detection of icebergs using dual SAR imagery. By using a false color visualization method,

they showed that an iceberg has distinguishable visibility from the background using a single polarization. They analyzed two SAR datasets of validated icebergs in sea ice. The algorithm used in this literature is focused on iceberg detection, false alarm removal and false alarm prioritization. The outlined model proposed here assumes a multivariate Gaussian distribution for both icebergs and sea ice backscatter.

Results obtained by using visualization methods with dual polarization false colour composite imagery showed that the occurrences of icebergs appeared more distinct in the composite imagery than in their native single polarization form. A prototype image processing software package that presently supports RADARSAT-2 Wide and TerraSAR-X Strip map imagery have been used in this methodology.

2.4.3 Detection of Icebergs in Sea Ice using Polarimetric RADARSAT-2 Data

Dierking & Wesche (2014) discussed the capability of polarimetric parameters of C-band radar for detecting icebergs in sea ice. The polarimetric parameters used in this study were co- (HH, VV) and cross- (HV, VH) polarization channels, entropy and alpha angle, which is obtained from Cloude-Pottier decomposition; these parameters are very useful for deducing the volume scattering contribution. Dierking & Wesche attempted to detect which backscatter mechanism is dominant for icebergs in sea ice by evaluating different polarimetric parameters. The analysis of the cross-polarization ratio and the correlation coefficient between the HH and VV indicates that the radar signatures of icebergs are dominated by surface scattering and multiple reflections of the radar signal from the inside

of the iceberg. The relative contribution of each scattering mechanism varies depending on the surrounding sea ice properties. The authors found that the scattering mechanisms are not definitive, because the spatial patterns of polarimetric parameters as well as the decomposition results vary from iceberg to iceberg. Nonetheless, this study is an inspiration for this thesis. The data that were used in this study were acquired at C-band (5.3 GHz) in single-polarization mode (VV- or HH-polarization).

2.4.4 Iceberg Detection Using Full Polarimetric RADARSAT-2 Data in West Antarctica

Kim, Kim, Kim, & Hwang (2011) used RADARSAT-2 images acquired over the West Antarctica region to investigate the detection of icebergs that have broken off from the Wilkinson glacier. The Freeman-Durden and unsupervised H/α decompositions were mainly used to classify the images. These decompositions were used successfully to distinguish icebergs from the sea ice shelf and surrounding sea ice. They showed that the $[1 - H][1 - A]$ parameter can distinguish icebergs and sea ice more accurately than the H and α itself and that the chance of false target detection is lower.

The results from the classification have shown that a few icebergs which have a similar intensity of volume and surface scattering are classified as sea ice and most of them were classified accurately when the volume scattering was dominant. They proved that $[1 - H][1 - A]$ can be a useful parameter for iceberg detection, although some of the icebergs were not clearly distinguishable, even from the Freeman-Durden or $H/A/\alpha$ decomposition.

2.4.5 Automatic Iceberg Detection in Open Water and Sea Ice

Akbari & Brekke (2018) made a notable contribution to iceberg detection in open water and sea ice using C-band polarimetric SAR data. They proposed a new methodology of automatic identification of potential icebergs high resolution polarimetric SAR images. The proposed algorithm is fitted to various sea ice conditions, high iceberg density, icebergs varying by size, and in heterogeneous background conditions. The methodology proposed here uses a simple feature-based segmentation to produce distinct standardized regions between the ice and water. The detector makes use of different polarization channels of the RADARSAT-2 image.

The iceberg detection model proposed here has five major steps. These are preprocessing, land masking, polarimetric feature extraction, segmentation and discrimination. Akbari & Brekke (2018) also mentioned some advantages of the proposed detector over conventional CFAR. For instance, the new detector models for both clutter and the target, can handle different sea states, and high iceberg density and clutter edge effects automatically without window processing and tuning parameters. For the proposed segmentation-based iceberg detection technology, the confidence level is set to 99%.

3. RADARSAT-2 Data

Generally, targets on the ocean can be detected by SAR sensors when the target of interest contrasts with the ocean background. Ocean and target backscattering mechanisms are variable and complex; target detection can be difficult to model and implement in an operational context. The most challenging part of iceberg detection is the heterogeneous clutter caused by wide ranges of background intensity variation due to meteorological and oceanic conditions, e.g., with different wind conditions, and different surrounding sea ice (Akbari & Brekke, 2018). This challenge creates what is known as a false alarm target from the bright background clutter. As a result, it lowers the reliability of an automatic iceberg detection process. In this study, iceberg targets that appear brighter than the ocean or sea ice background are of interest. Target detection can then be maximized by selecting the polarization channel of the image that produces the highest signal to clutter (ocean, sea ice) contrast (the ratio of target backscatter to ocean backscatter).

This chapter describes the SAR data collection performed to support this study. Two areas have been selected, one is near the northeast coast of Newfoundland and Labrador, Canada and the other is the west coast of Greenland. All the images used in this study have been acquired from these two areas and contain a significant number of icebergs. Based on the icebergs background type and geographical location, the icebergs are categorized into three groups (shown in Figure 3.1). Furthermore, two kinds of comparison have been performed among these three groups.

The first comparison has been done between icebergs surrounded by sea ice and icebergs in open water, thus presenting two different background conditions to characterize the iceberg backscatter. Every year, a large quantity of these calved icebergs arrives in the Labrador Sea and on the Grand Banks, primarily during the spring and summer.

Another comparison has been performed between iceberg targets in open water that have been collected in two distinct regions, including Newfoundland sea and Davis Strait, thus allowing a comparison of icebergs that are freshly calved versus icebergs that have been weathered through several seasons.

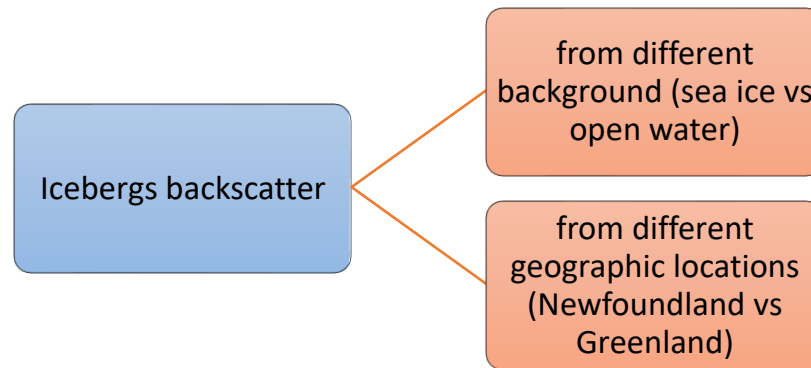


Figure 3.1: Grouping of data sets for analysis.

3.1 Data

RADARSAT-2 is a Canadian earth observation satellite developed to monitor environmental change and to support resource sustainability (Morena, James, & Beck, 2004). This satellite was launched in 2007 and provides high resolution SAR imagery. Table 3.1 presents the information of all the RADARSAT-2 images that have been used in this study. A large iceberg dataset has been prepared for the analysis to ensure a reliable

statistical comparison. Twelve fine quad RADARSAT-2 images containing icebergs have been collected from Newfoundland (in open water and ice infested water) and five fine quad RADARSAT-2 images from Greenland region.

In this study, a statistical comparison is made of the three sets of icebergs, including icebergs in sea ice compared with icebergs in open water in the same geographic location and icebergs in open water from two different geographic locations. Figure 3.2 below shows the locations of the study areas. The sets of images with icebergs surrounded by sea ice have been acquired from the northern part of the Newfoundland, specifically from the St. Anthony and Bell Isle areas, whereas the images of icebergs in open water have been collected from Bonavista, Newfoundland. Geographical and weather conditions of these two locations are similar and thus the icebergs are expected to be comparable. The images were captured in May-June, 2017 and August, 2009.

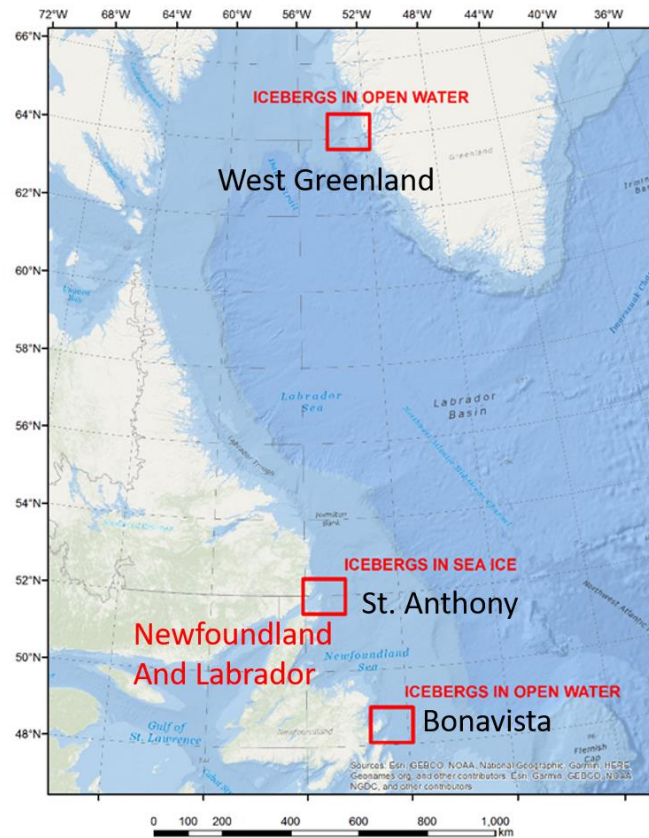


Figure 3.2 Study area

The weather conditions of the Newfoundland and the Greenland region can be quite different because of the latitude difference. Greenland is located further north than Newfoundland and, in the case of the Greenland data collection location, is 10°-15° further north than the two Newfoundland data collection regions. In spite of that, the ambient air temperatures during the time frames of the data collections are not significantly different, varying by only a few degrees Celsius. Nonetheless, the icebergs' backscatter from these places might be different, considering not only the weather conditions, but also the weathered nature of the Newfoundland icebergs relative to those from Greenland. It takes

many years for Greenland icebergs to reach Newfoundland from Greenland after calving. During these years, icebergs normally change significantly in size and physical properties. This study's focus is to find out whether there is any significant difference in iceberg characteristics between Greenland and Newfoundland icebergs. Table 3.1 presents the available radar images and meteorological conditions during the data acquisition, incident angles, acquisition times and locations. A summary of all iceberg ground truth information for this study can be found in Appendix IV.

The frequency band used in RADARSAT-2 is 5.405 GHz, which is in the C-Band (8-4 GHz) frequency range. The fine quad images were delivered in an SLC slant-range format, which is characterized by a nominal pixel spacing of 4.7 m \times 5.1 m in slant range and azimuth, respectively, covering approximately 35 km \times 50 km. The RADARSAT-2 data containing icebergs in open water or in sea ice pack are used to evaluate the performance of the iceberg backscatter analysis. The polarimetric SAR data holds great promise for this analysis because, as outlined in Chapter 2, they can be decomposed into a contribution of specific scattering mechanism.

Table 3.1 Image acquisition details

Image	Date	Time (UTC)	Incident angle range	Beam mode	Temp.	Wind speed
Iceberg in sea ice (NL) [†]	9 June, 2017	21:23:48	27°-30°	FQ9W	16°C	13 km/h
	9 June, 2017	21:23:51	27°-30°	FQ9W	16°C	13 km/h
	9 June, 2017	21:23:44	27°-30°	FQ9W	16°C	13 km/h

[†] Source https://weather.gc.ca/forecast/canada/index_e.html?id=NL weather information for different parts of Newfoundland. The location is the closest weather station to the SAR acquisition, and it is recognized that the local conditions are likely to be different than the weather conditions reported for Newfoundland.

Image	Date	Time (UTC)	Incident angle range	Beam mode	Temp.	Wind speed	
Total iceberg 55	9 June, 2017	21:23:41	27°-30°	FQ9W	16° C	13 km/h	
	9 June, 2017	21:23:31	27°-30°	FQ9W	16° C	13 km/h	
	9 June, 2017	21:23:55	27°-30°	FQ9W	16° C	13 km/h	
Iceberg in open water (NL) ‡	30 May, 2017	21:14:52	28°-30°	FQ10W	11.7° C	11 km/h	
	30 May, 2017	21:14:49	28°-30°	FQ10W	11.7° C	11 km/h	
	13 June, 2017	21:06:32	19°-21°	FQ1W	8.5° C	36 km/h	
	Total iceberg 39	13 June, 2017	21:06:30	19°-21°	FQ1W	8.5° C	36 km/h
	16 June, 2017	09:56:55	19°-22°	FQ2W	8.3° C	16 km/h	
	30 May, 2017	21:06:35	27°-30°	FQ1W	8.5° C	14 km/h	
Iceberg in open water (Greenland) §	5 August, 2009	20:52:10	23°-25°	FQ5W	6° C	11 km/h	
	15 August, 2009	20:52:13	24°-26°	FQ6W	9° C	29 km/h	
	22 August, 2009	20:56:24	24°-26°	FQ7W	9° C	32 km/h	
	Total iceberg 35	25 August, 2009	21:09:00	23°-25°	FQ5W	11° C	21 km/h
	15 August, 2009	11:02:31	28°-29°	FQ9W	9° C	62 km/h	

The first two rows of Table 3.1 represent detailed information about Newfoundland icebergs. Six fine quad RADARSAT-2 images containing iceberg targets in open water were acquired from the Bonavista region at relatively small incident angles (19°-30°) in June 2017. Six fine quad RADARSAT-2 images of icebergs in sea ice were acquired from the upper region of Newfoundland (St. Anthony), also at a lower incident angle range (27°-30°) in June of the same year. The weather conditions on those image acquisition days are also shown on the table.

Five fine quad images of icebergs in open water have been acquired at a lower incident angle range (23° to 29°) from the west Greenland region. Thirty three icebergs were located

‡ Source https://weather.gc.ca/forecast/canada/index_e.html?id=NL weather information for Newfoundland

§ Source <https://www.wunderground.com>, weather information for Nuuk, Greenland. Note that this location is the closest weather station to the SAR acquisition, and it is recognized that the local conditions are likely to be different than the weather conditions reported for Nuuk.

and ground truthed within these five images. The images were acquired at the end of summer during August 2017.

The ability to detect icebergs in SAR images depends on several factors, including the physical properties of the iceberg (size, shape, and structure), SAR sensor properties (incidence and azimuth angles, resolution, frequency, and polarization), geophysical parameters, such as wind speed and direction, sea state, surface currents, temperature, seasons and the backscatter of the surrounding sea ice or water. As we see from Table 3.1, the properties of all acquired images, including incident angle range, time of image acquisition (summer) and weather conditions are quite similar for all the SAR images. The images were taken from the same satellite RADARSAT-2 in single look complex (SLC) mode and in the same frequency band (5.405 GHz).

3.2 Target Detection

Reliable detection of icebergs is the most important component of iceberg surveillance. The detection of icebergs is very challenging when they are embedded in sea ice. As a consequence, all of the iceberg data presented here were verified by ground truth. In many cases, the ground truth icebergs were not readily identifiable within any of SAR channel and therefore, the ground truth information was very important to ensure that the extracted SAR backscatter was indeed from icebergs and not from other objects (e.g., sea ice).

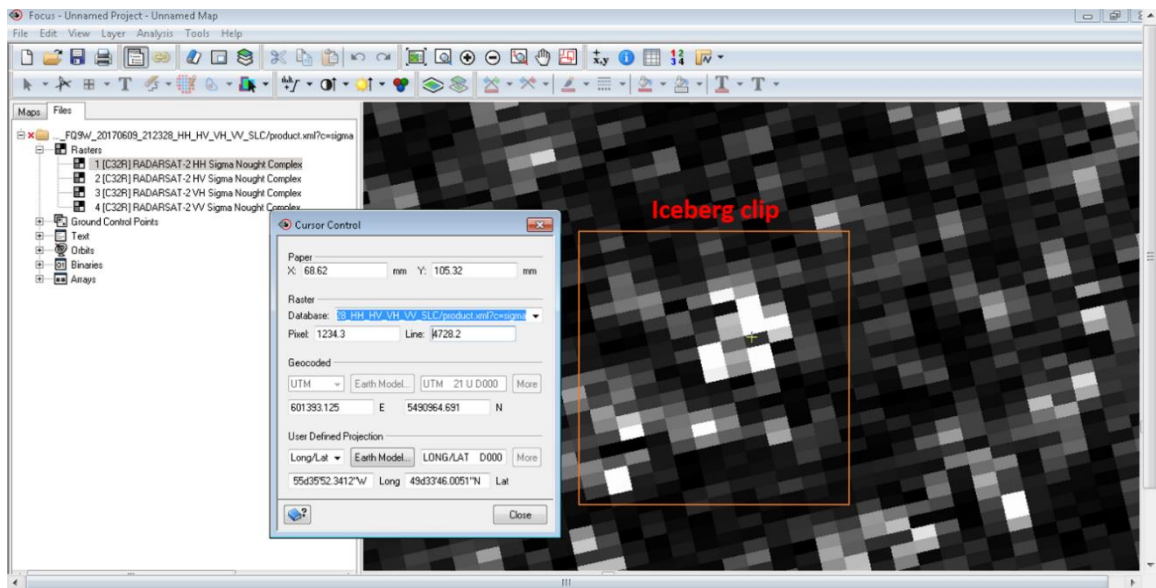
The iceberg ground validation was provided by C-CORE through several field programs. The ground validation at Bonavista and St. Anthony were funded through a grant from the Research and Development Corporation of Newfoundland and Labrador (RDC) and

Defense R&D Canada (DRDC). The Greenland icebergs were validated as part of an exploration program funded by Cairn Energy (UK). Regarding ground truth data, the icebergs were identified in two steps, eliminate ship targets and detect icebergs. Provincial Aerospace Limited (PAL) was contracted to supply offshore ice observers and equipment to perform the ground truth work. Maritime Safety and Security Information System (MSSIS) AIS (Automatic Identification System) ship information was also available as primary ground truth for some regions to differentiate ships from icebergs. Target coordinates were compared to the SAR image for visual confirmation of the target and extraction of the target statistics. Although the original CLG data didn't provide the SAR target locations directly, a shape file was created containing target location information using Geographic Information System (GIS) tools, ENVI and ArcGIS.

Secondary ground truth was also extracted based on very high-confidence targets identified by highly-experienced analysts. These targets were extracted after the elimination of primary ground-truth targets (ships, vessels) and occurred in regions which were highly populated with icebergs with very little shipping activity (such as Greenland datasets). Landmask of Newfoundland and Greenland region were used to segregate the main land, island or big rock. For analyst-selected targets, a selection process was implemented to reduce the possibility of target contamination. Most iceberg targets were identified using secondary ground truth since a high number of ships were extracted using AIS data.

3.3 Iceberg Detection Using Ground Truth information

The ground truth information was provided in a spreadsheet, carrying the information of icebergs longitude/latitude, pixel/line location and image scenes containing icebergs. PCI Geomatica 2017 have been used to extract the iceberg clip form the RADARSAT-2 scene using ground truth information. Figure 3.3 shows the iceberg clipping process using ground truth data information. First the image is clipped from the raw (sigma naught complex) RADARSAT-2 scene in PCI Geomatica and then converted it to intensity layer. Then thresholding has been implied using MATLAB. The pixel and line information of each iceberg in the associated images can be found in Appendix IV of this thesis.



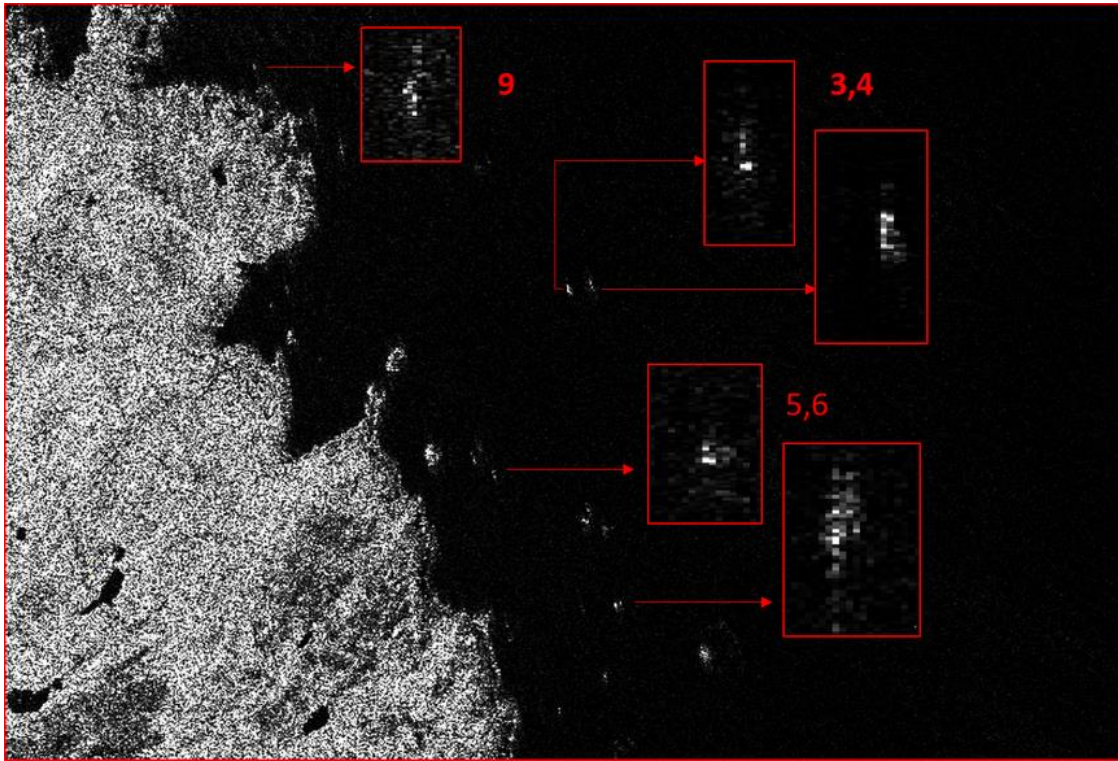


Figure 3.3: Top: iceberg identifying using pixel/line information from ground truth data in PCI Geomatica; Bottom: Several icebergs that have been clipped from HV channel from a scene, red box shows the zoomed iceberg clip.

As fine quad RADARSAT-2 data have been used in this study, it provides four polarimetric channels, including both co polarization (HH, VV) and cross polarization (HV, VH) channels. As a consequence, the full scattering matrix, S , can be reconstructed, thus allowing for polarimetric decompositions. All the identified icebergs that were ground validated in the presence of sea ice are either completely or partially surrounded by the pack.

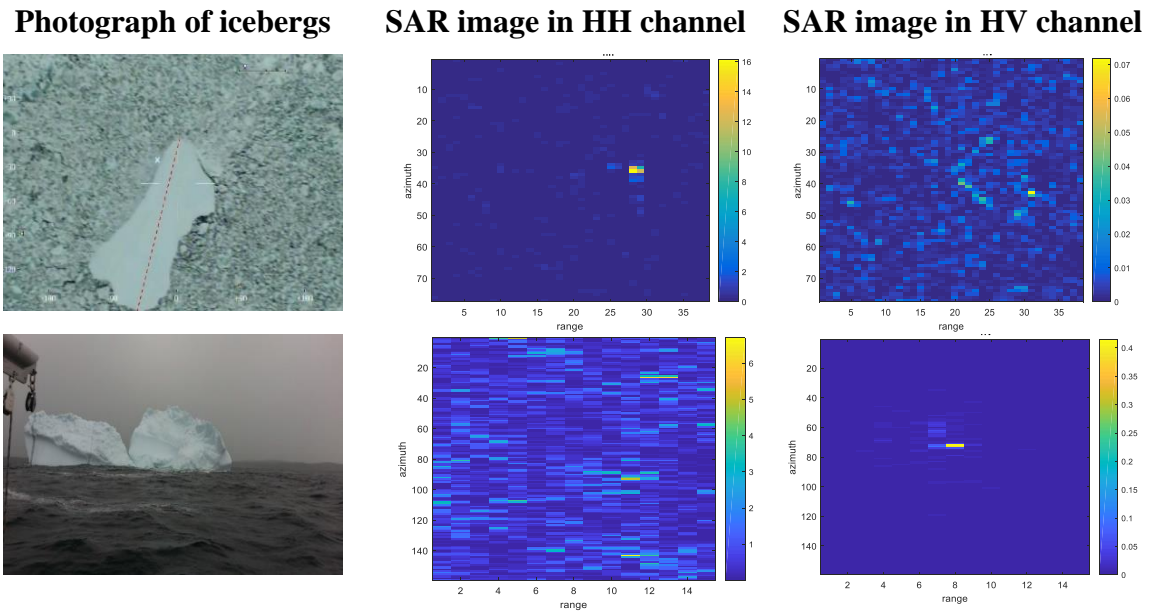


Figure 3.4: Iceberg backscatter (power) in SAR in different polarization channels (Photograph courtesy: C-CORE)

The first image in column 1 from Figure 3.4 is an example of icebergs in sea ice and the second image is an iceberg in open water. The surrounding clutter (water, sea ice) contributes to the total backscatter in the different polarimetric channels. Figure 3.4 shows an example of the backscatter response of icebergs in the co- and cross- polarization channels. The signal to clutter ratio is greater in HH than HV, which implies that the iceberg intensity is much higher in HH than HV. For this incidence angle range, the HH channel is more suitable to detect icebergs in sea ice than HV. However, for this incidence angle range, icebergs in open water are more distinguishable in the HV channel as the ocean response in the HH channel is very high compared to the HV channel. The next chapter will describe the processing of SAR scenes and implementation of decomposition and statistical algorithms.

4. Methodology

The comparative analysis of iceberg backscatter is shown for two different circumstances: icebergs surrounded by different clutter and icebergs from different geographical locations. This section describes the methods of the parameters representation and tests that have been used for statistical analysis. The five types of decomposition techniques described earlier (i.e., Pauli, Freeman-Durden, van Zyl, Yamaguchi and Cloud-Pottier) have been used for the analysis here for comparison. Each decomposition accounts for the three backscatter mechanisms described above except Yamaguchi.

Unlike other decompositions, along with three common backscatters, Yamaguchi derives another scattering mechanism ‘helix’ contributed by helical targets. Figure 4.1 shows the flow chart of the processing chain of this study. The processing steps to get the final comparative results have three main parts; 1) SAR image pre-processing, 2) decomposition and 3) hypothesis test. The following sections describe all the steps in details.

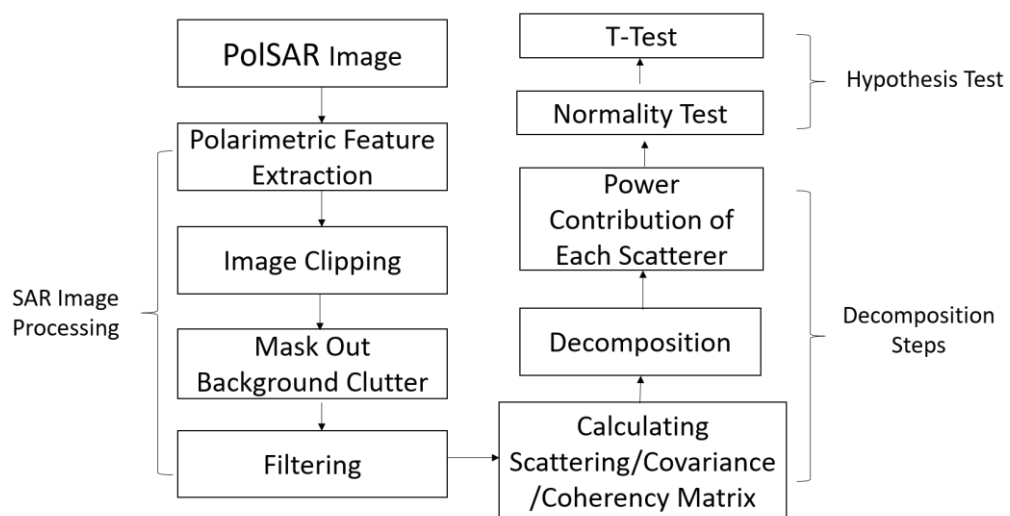


Figure 4.1 Flow chart of the processing chain

4.1 SAR Image Processing

The processing of SAR image starts with an input multi-channel single look complex (SLC) PolSAR data. First, the PolSAR data was loaded to the SNAP ESA tool and then the further processing was done in that platform. Then pre-processing of SAR image follows three steps: feature extraction, clipping and masking.

4.1.1 Polarimetric Feature Extraction

For the separation of icebergs from sea ice and the ocean, the use of multipolarized SAR images has proven to be useful (Dierking & Wesche, 2014). A number of investigations have focused specifically on the application of polarimetric SAR systems, which acquire data at VV, HH, VH and HV polarization. These features are directly related to the physical property of the scattering medium. In this step, both intensity and complex conjugation values of full polarimetric channels (HH, HV, VH, VV) were extracted. The intensity value is mainly the sigma naught intensity value of each polarimetric channel. The intensity values have been used directly to compare the icebergs backscatter based on the backscatter coefficients.

4.1.2 Image Clipping

The objective of the step of image clipping is to segment each iceberg area from the main SAR image using the ground truth information of icebergs. Ground truth information comes in the form of pixel and line information of the middle pixel of each iceberg based on the field data. Each iceberg was segmented based on the ground truth value. First, an

approximate area was selected by keeping the ground truth pixel in the middle as a reference. The area was selected in such a way that it contains all pixels of a single iceberg and surrounded by clutter pixels. That is how a single iceberg clip or segment contains an iceberg along with sea ice or open water pixels. Section 3.3 previously described the methodology of how this is achieved.

4.1.3 Masking

Clutter masking is one of the main challenges of detecting icebergs. In this study, individual binary masks have been used for each iceberg to remove the clutter. The binary mask was determined from a threshold that is calculated from the mean and standard deviation of the intensity value of the iceberg clip to mask out the ocean or sea ice area from the iceberg backscatter. For icebergs in open water, icebergs can easily be separated from ocean clutter because icebergs targets are generally brighter than the surrounding open water backscatter. For icebergs in sea ice, determining an optimal threshold is sometimes difficult, since the background clutter sometimes masks the backscatter of the iceberg. A hard thresholding value is taken to remove all the clutter pixels. In many cases, because of hard thresholding, some of the target pixels ended up being masked out. Equation 3.1 shows how the threshold is determined:

$$T_d = \mu + f * \sigma, \quad (3.1)$$

where, T_d is the threshold, μ is the mean, f is the multiplying factor and σ is the standard deviation of the clipped SAR image intensity value containing target. The multiplying

factor varies based on clutter type and intensity value and is determined by trial and error. For icebergs in sea ice, f was set to 13 and for icebergs in open water, f was set to 10.

When the intensity value of an image pixel is lower than the threshold value, that pixel is set to zero in the mask, whereas for intensity values greater than the threshold, the value of the pixel is set to 1 in clutter mask. Thus, the clutter mask is generated and then multiplied with the SAR image to isolate the target pixels. Figure 4.2 shows an example of masking the iceberg pixels from sea ice clutter. The colour bar represents the intensity value of the SAR image radar cross section. The clutter masked image is then used for further analysis. Figure 4.2 (a) presents an iceberg image with sea ice clutter and (b) is the processed iceberg image that is used for further analysis.

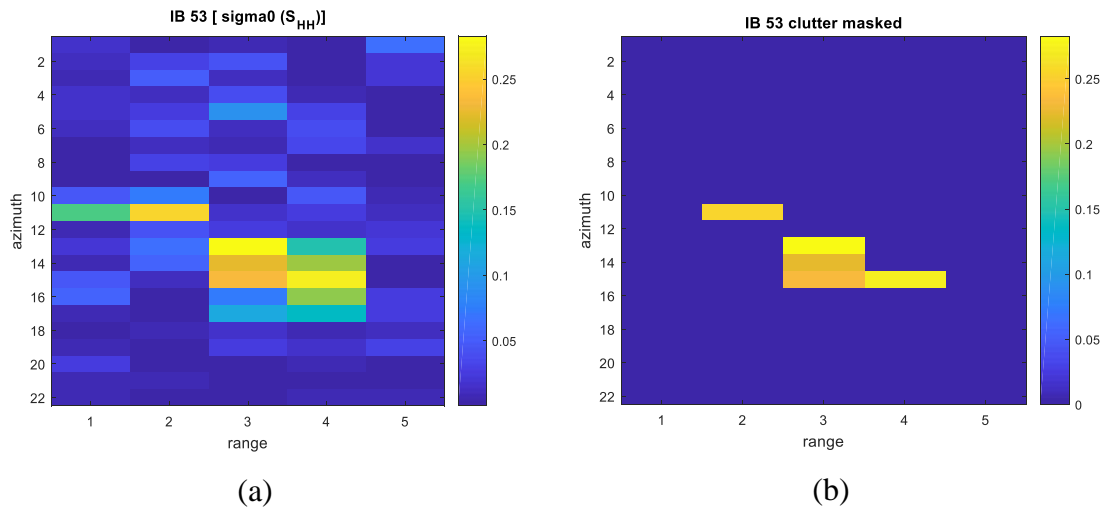


Figure 4.2: Clutter masking, (a) Target pixel in sea ice clutter before masking; (b) Target pixel without clutter after masking.

While detecting icebergs using the ground truth information (long/latitude, pixel/line), some icebergs in sea ice had a very low contrast in all polarimetric channels, relative to the

clutter. These icebergs were not used in this study as it was not possible to threshold the sea ice clutter from the iceberg. Figure 4.3 shows an example of this kind of ‘masked’ target, whereby the surrounding sea ice clutter and iceberg have no discernable contrast. The ground truth information indicated that there is an iceberg at the geographic location in question, however it is not visible in neither the HV nor in the HH channel. Therefore, thresholding is not possible for these types of icebergs and these have been excluded from the study. Note there have been demonstrated cases at C-CORE whereby the iceberg signature is darker than the surrounding sea ice, and thus the iceberg, while visible, is not detectable by standard CFAR methods. This is an incidence angle effect, whereby at very small incidence angles, sea ice backscatter is much brighter than that of icebergs.

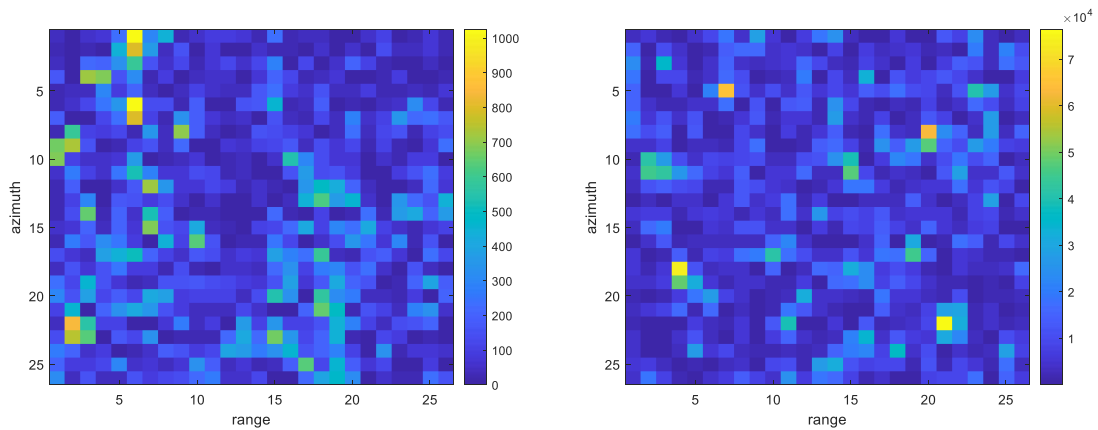


Figure 4.3 iceberg completely merged with sea ice clutter in both HV (left) and HH (right) channel; though it has the ground truth information (From field survey).

4.1.4 Filtering

Filtering is also an essential part of preprocessing as the SAR data are noisy. Except the Pauli decomposition, filtering step have been implemented for all other decompositions

i.e., Freeman-Durden, van Zyl, Yamaguchi and Cloud-Pottier. The general approach of a boxcar filter has been used in this case (Lee & Pottier (2009)). A small window of 3×3 was chosen to minimize impacts on the iceberg morphological structure and potential scattering centers.

4.2 Polarimetric Decompositions

Polarimetric decompositions have been used to compare the scattering response of the collection of iceberg targets. As stated earlier, the main goal of these decompositions is to express the average matrix as a sum of independent matrices representing independent elements and to associate a physical mechanism with each element. These decompositions facilitate the interpretation of the scattering process within the icebergs. The decompositions used in this analysis include all those previously listed in Section 2.2. Details of the application of these decompositions are as follows:

- Pauli: The complex conjugate value of the scattering matrix has directly been used in this decomposition to calculate the power contribution of the surface, double bounce and volume scattering layers. The filtering step has been skipped for this method. In general, the coherent decompositions are prone to speckle issues, so they are not appropriate when applied to natural random targets such as vegetation. Nevertheless, it is still suitable when the scene is of high resolution and dominated by a single or few scattering elements. The Pauli decomposition does not need any filtering in the case of single targets like icebergs.

- Freeman-Durden: This decomposition was applied using a sliding window of 3×3 to calculate mean covariance matrix. As with the Pauli decomposition, the output was three scattering classes including Bragg surface scatterer from a moderately rough surface (s), even or double bounce scattering (d) and volume scattering (v) from randomly oriented dipoles.
 - van Zyl: The 2008 version of this decomposition was applied to the iceberg dataset. The dimension of the sliding window size for computing mean covariance matrix was the same as Freeman-Durden (3×3). As with the two previous decompositions, the output is three classes including surface, double bounce and volume.
 - Yamaguchi: This decomposition adds the additional helix scattering term corresponding to the non-reflection symmetric cases. As with van Zyl and Freeman-Durden, a 3×3 window was used to compute the mean covariance matrix.
- Cloud-Pottier: The nine class nature of this incoherent decomposition does not lend itself to an easy comparison with the other four decompositions. Furthermore, this decomposition does not have the analogous ‘target’ nature of the other three and thus the dominant scattering class of the entire iceberg was extracted with this decomposition. For example, in the case of Pauli, a single iceberg can be decomposed into percentage backscatter of each of the three scattering classes (e.g., A% surface, B% double bounce and C% volume), whereas in Cloud Pottier only a single class (e.g., zone 9, Bragg Surface) will be the result. This meant that it was unnecessary to apply the statistical T-test to the output since a comparison of the

number of icebergs falling into each of the nine classes can be readily accomplished.

4.3 Hypothesis Test

The objective of the T-test is to find the significance between two different samples and in this application, it was used to differentiate between the following situations:

- Geographic location: Newfoundland icebergs versus Greenland icebergs
- Scattering background: Icebergs in sea ice versus icebergs in open water.

Both two tail and one tail T-tests have been applied to the three sets of icebergs for the two situations outlined above.

The datasets need to fulfill a certain number of preconditions before applying the T-tests to the sample sets. The conditions are that both data sets should have to be normally distributed and the sample size for both sets should be above 30 to secure a robust result.

In the case of the sample size, the Newfoundland icebergs in sea ice sample size is 55, the open water iceberg sample size is 39, and the Greenland iceberg sample size is 35. Therefore, all three data sets follow the condition of the sample size range.

Concerning the normality distribution condition, all samples were examined statistically to determine their fit to the normal distribution. To be normally distributed, the data must have similar mean and median values, and the skewness and kurtosis value should be

between -2 and 2. The table below shows an example of normality test for the set of volume scattering of the Pauli decomposition for icebergs in sea ice.

Table 4.1: Normality test, Pauli Volume Iceberg in Sea Ice

Parameter	Value
Mean	-18.1
Standard Error	0.7633
Median	-19.36
Standard Deviation	5.712
Sample Variance	32.627
Kurtosis	-0.654
Skewness	0.1697
Range	23.23
Minimum	-30.89
Maximum	-7.658
Sum	-1013
Count	56

From Table 4.1, the mean is -18.1, which is comparable to the median of -19.36, and the skewness and kurtosis are both between than 2 and -2. Thus, this dataset is normally distributed. Note that all the datasets used in this study pass the normality test and are eligible for the statistical T-test analysis. Both the one and the two tail T-test have been implemented here. As both T-tests are described in Chapter 2, the following two sections focus on the results obtained from the tests.

4.3.1 Two tail T-test

The T-test was used to compare the surface, double bounce and volume scattering of Pauli, Freeman-Durden and van Zyl decompositions for the specific situations in question (sea

ice versus open water, Newfoundland versus Greenland). The significance level was set as $\delta = 0.05$, which is common significance level for statistical tests. Table 4.2 shows the test statistics of two samples, including volume scattering of the Pauli decomposition for icebergs in sea ice versus icebergs in open water. When the probability value P of the dataset obtained from the T-test is greater than the significance level, both data sets are not considered to be significantly different and we accept the null hypothesis. If the probability value P is smaller than the significance level, then the data samples are considered to be significantly different and we reject the null hypothesis. We can also examine t_{STAT} and t_{CRIT} to come to the same conclusion. If t_{STAT} is positive and greater than t_{CRIT} , or if t_{STAT} is negative and is less than $-t_{CRIT}$, then we reject the null hypothesis.

Examining Table 4.2, the significance level P is less than 0.05, and clearly t_{STAT} (negative) is less than $-t_{CRIT}$, and thus we reject the null hypothesis at the 0.05 significant level. This procedure has been applied to all of the decompositions for each of the scattering types, except in the case of the Cloud-Pottier decomposition. These results are discussed in further detail in the next chapter.

Table 4.2 Two sample T-test (assuming unequal samples) for Pauli decomposition volume scattering (sea ice versus open water)

Statistical Parameter	Volume_Pauli_IBSI	Volume_Pauli_IBOW
Mean	-18.097	-12.139
Variance	32.627	10.312
Observations	56	32
Hypothesized Mean Difference	0	
Df	86	
t_{STAT}	-6.264	
$P(t_{STAT} \leq t_{CRIT})$ one-tail	7.158E-09	

Statistical Parameter	Volume_Pauli_IBSI	Volume_Pauli_IBOW
t_{CRIT} one-tail	1.663	
$P(t_{STAT} \leq t_{CRIT})$ two-tail	1.432E-08	
t_{CRIT} two-tail	1.988	

4.3.2 One tail T-test

As suggested in the previous section, the two tail T-test was used to confirm whether or not there were differences between scattering types in each of the decompositions. For the case where the null hypothesis is accepted, these have been excluded from further analysis since the samples are considered to be statistically equivalent. The one tail T-test was applied to the cases where the hypothesis test found significant differences between scattering types. Thus, the application of the one tail test was used to determine whether a scattering type was greater on one situation or another (e.g., is iceberg surface scattering greater in sea ice or in open water). As discussed further in Chapter 5, in the case of surface scattering of icebergs in sea ice versus open water, the two tail T-test found that surface scattering for icebergs in sea ice was significantly different than those in open water, and that volume scattering for icebergs in open water was significantly different than those in sea ice. The one tailed T-test was considered for these specific cases. Table 4.3 shows an example of one of these one-tail T-test results for the Freeman-Durden decomposition for surface scattering of icebergs in sea ice versus icebergs in open water. The null hypothesis is Sea Ice > Open water and the alternative hypothesis is Sea Ice < Open Water. The red line $P(t_{STAT} \leq t_{CRIT})$ one tail value is 0.006398. As before, when $P < 0.05$ significance level, it rejects the null hypothesis. Thus, in this case, surface scattering of icebergs is less

dominant when the iceberg is in sea ice compared to when it is in open water for the Freeman-Durden decomposition.

Table 4.3 One tail T-test of Freeman-Durden surface scattering in sea ice and open water

Statistical Parameter	Sea Ice	Open Water
Mean	-1.131	-2.865
Variance	2.356	12.752
Observations	56	32
<i>DoF</i>	38	
t_{STAT}	2.617	
$P(t_{STAT} \leq t_{CRIT})$ one-tail	0.00640	
t_{CRIT} one-tail	1.686	
$P(t_{STAT} \leq t_{CRIT})$ two-tail	0.0128	
t_{CRIT} two-tail	2.024	

5. Results

A complete analysis of the iceberg datasets included both an analysis of radar cross section differences within the polarimetric channels and an analysis of the outputs of various polarimetric decompositions. Firstly, 2D radar cross section plots of the different polarimetric channels (HH, HV, VV) are provided to give some insight on potential backscatter differences within each channel. Secondly, the polarimetric decomposition results were obtained by following the methodology outlined in the previous section. The decomposition results are presented as a series of plots that graphically illustrate the dominant scattering types for each iceberg. Plots have been generated for each dataset and for each decomposition. The plots are supplemented by the hypothesis tests that provide a statistical comparison of the datasets for each backscatter type. Note that the following acronyms are used for each of the iceberg sample sets:

- NLSI: Newfoundland icebergs in sea ice;
- NLOW: Newfoundland icebergs in open water;
- GLOW: Greenland icebergs in open water.

5.1 Radar Backscatter Plots

When target radar cross sections for the various polarimetric channels are plotted on a simple x/y scatter plot, it provides a simple yet effective feedback on target scattering behavior for the different target scenarios. Figure 5.1 illustrates radar backscatter plots of HV and VV versus HH for icebergs in open and sea ice in the Newfoundland region. Each point in the plot represents the average σ^0 of a total radar cross-section of each iceberg.

The chart to the left in the figure plots HV versus HH, while the right chart plots VV versus HH. The left-plot shows that the icebergs in sea ice and icebergs in open water are quite separable. That indicates that the combination of HH and HV is a good discriminator of the scattering types in iceberg targets. However, the right chart shows that the dual co-polarization combination (HH vs VV) is less useful for separating these two iceberg datasets. In particular, there is much confusion and very little separability between the two situations.

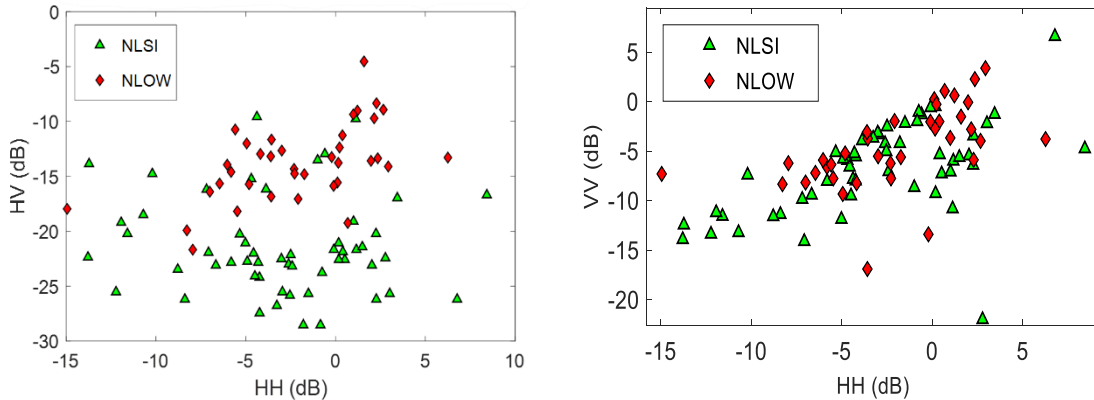


Figure 5.1: Comparison of polarimetric parameters (intensity) Left: HH vs HV; Right: HH vs VV

In Figure 5.2, the same radar cross section plots are given (HH vs HV, HH vs VV) for the Newfoundland and Greenland icebergs. As with Figure 5.1, each point in the plot represents the average intensity value of a total radar cross-section of an iceberg. As the Greenland icebergs are freshly calved and take several years to reach Newfoundland waters, there is speculation that weathering and temperature changes during the long journey south may affect the backscatter properties of the icebergs. However, as shown in

Figure 5.2, the radar cross section plots for both HH versus HV and HH versus VV show very little, if any, separation between the two classes. Though some of the Greenland icebergs are clearly separated at the lower end of the dB scale, most of the icebergs from the two classes are overlapping. Backscatter differences of icebergs from the two locations are hardly distinguishable in both plots. Therefore, to find the similarity or dissimilarity between these random data sets, further statistical analysis is necessary.

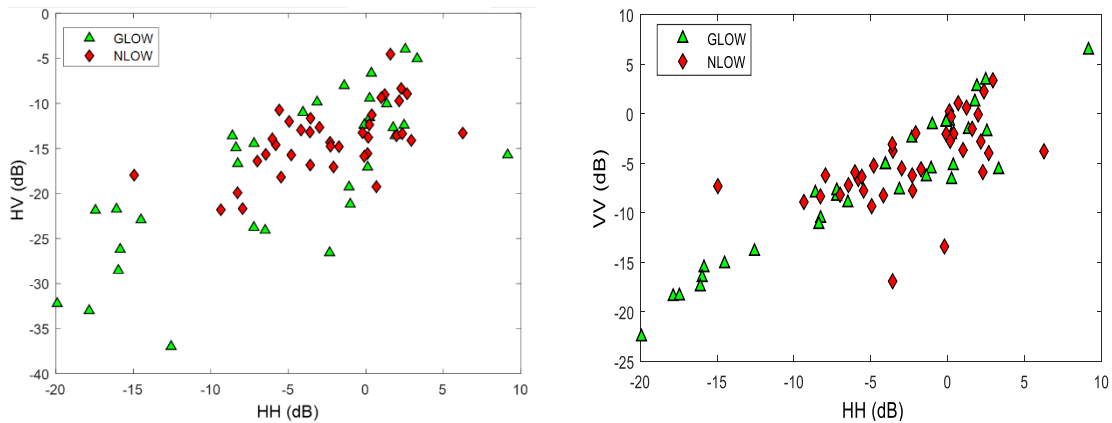


Figure 5.2: Comparison of polarimetric parameters (intensity) of Newfoundland and Greenland icebergs; Left: HH vs HV; Right: HH vs VV

5.2 Decomposition Results

This section provides an analysis of the decomposition results for all of the decompositions that have been presented in the previous chapters. The decomposition results of Pauli, Freeman-Durden, van Zyl and Yamaguchi have been presented here in normalized form, then converted to dB. Note that the values are expressed in units of dBr to indicate that it is relative to a reference level. The process to convert the power output from individual scatterers into normalized dB is shown below:

$$P_{total} = P_s + P_d + P_v (+ P_H \text{ for Yamaguchi}) \quad (3.2)$$

$$P_{s(norm)} = 10 \log_{10}(P_s/P_{total}) \quad (3.3)$$

In the equation above, $P_{s(norm)}$ is the normalized surface backscatter power from each iceberg and P_s, P_d, P_v are the sum of the power contribution of iceberg pixels due to surface, double-bounce and volume scattering respectively. Scatter plots for each decomposition are shown in the following subsections

5.2.1 Icebergs in Open Water Versus in Sea Ice (NLSI Versus NLOW)

This section presents the scatter plot of all five decomposition results for the set of icebergs in sea ice and open water in the Newfoundland region. For each of the plots, the horizontal axis is the iceberg sample index and the vertical axis is the normalized power contribution in dBr.

5.2.1.1 Pauli

Figure 5.3 shows the scatter plot of surface, double bounce and volume scattering contribution from Pauli decomposition. From Figure 5.3, we see that in the case of NLSI, volume scattering is quite low on an average, relative to double bounce and surface scattering. The range of volume scattering is between -8 to -30 dBr (Figure 5.3, top). However, in the case of NLOW, the range of volume scattering is in between -5 to -20dB (Figure 5.3, bottom). Thus, icebergs in open water give a slightly higher range of volume scattering than icebergs in sea ice. The same is true for double bounce scatter; open water bergs have a slightly elevated backscatter than the bergs in sea ice. The range of surface

scattering is quite close for both sets of icebergs (close to 0 dBr) and is dominant among the three scatterers.

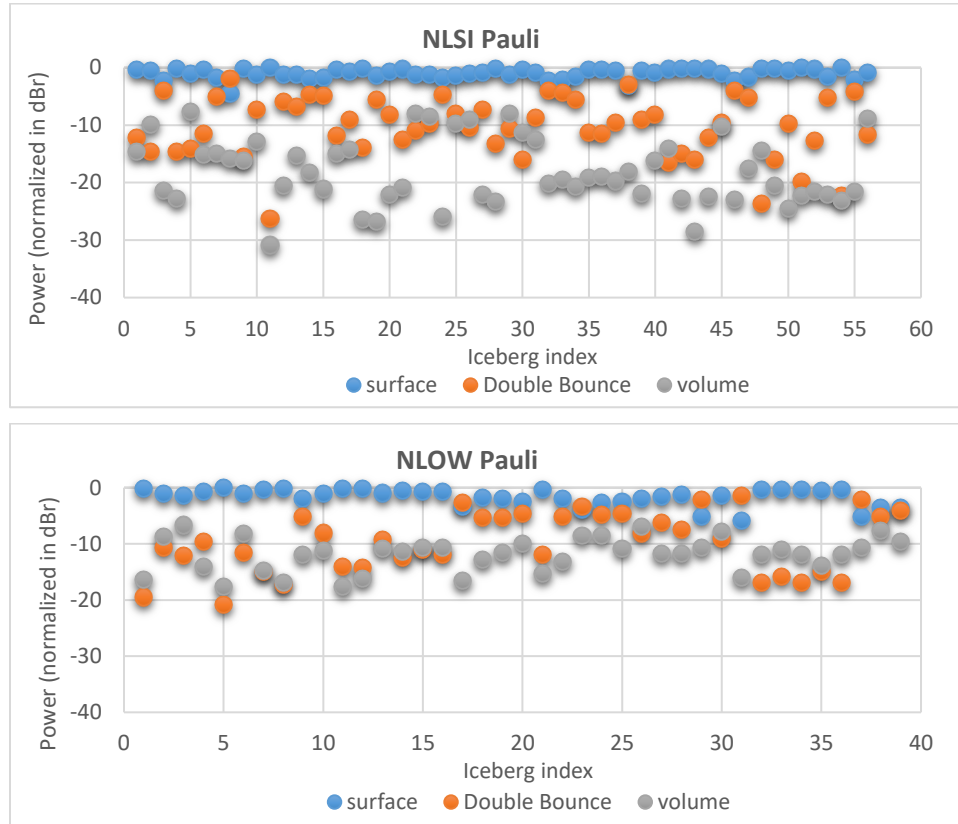


Figure 5.3: Pauli decomposition of NLSI and NLOW group

5.2.1.2 Freeman-Durden

Figure 5.4 shows the Freeman-Durden decomposition results as a scatter plot. As with Pauli, surface scattering is dominant for and in the range of (0 to -10 dBr) for NLSI and (0 to -15 dBr) for NLOW. In the case of volume and double bounce scattering, the range is slightly higher for icebergs in open water, so the trend of decomposition results is similar to Pauli decomposition results. There are some notable icebergs where double bounce

scatter is, in fact, the dominant scatterer. That is the case for both the NLSI and NLOW bergs, but there are more instances of this for the NLOW bergs.

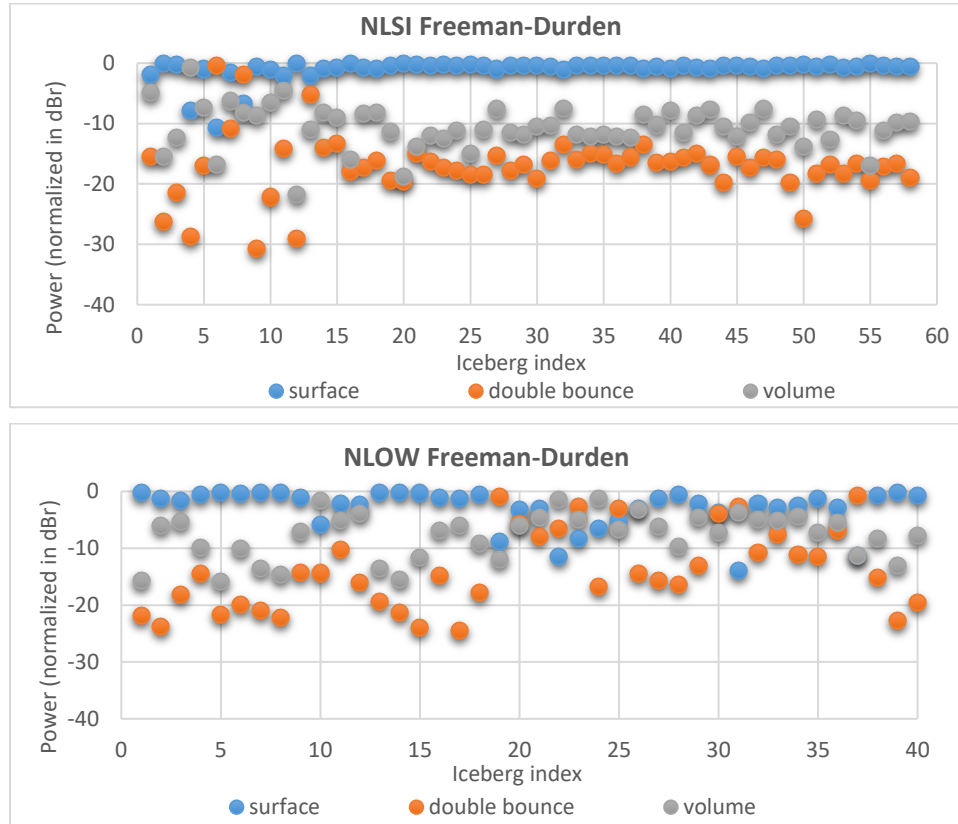


Figure 5.4: Freeman-Durden decomposition of NLSI and NLOW group

5.2.1.3 van Zyl

Figure 5.5 shows the van Zyl decomposition results. In the case of both NLSI and NLOW, the surface scattering power is again very dominant, for NLSI the range is (0 to -1 dBr) and for NLOW the range is (0 to -5 dBr). In the case of volume and double bounce scattering, it is difficult to visually compare the icebergs in both groups, however it appears that many of the bergs have an elevated volume and double bounce scatter for the open

water bergs. Therefore, the trend of the van Zyl decomposition is consistent with both Pauli and Freeman-Durden.

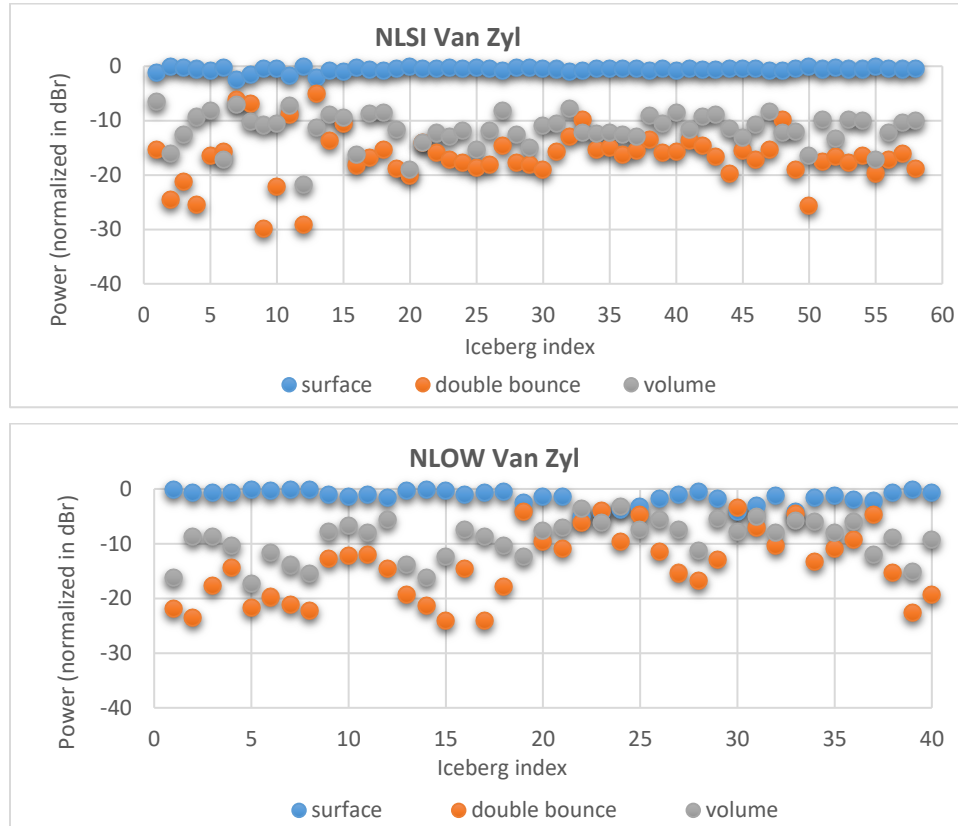


Figure 5.5: van Zyl decomposition of NLSI and NLOW groups

5.2.1.4 Yamaguchi

Figure 5.5 presents the comparison of icebergs in sea ice versus open water for the Yamaguchi decomposition. Figure 5.5 (bottom) shows a very dominant surface scattering over double bounce and volume scattering in NLSI. The relative surface scattering power value is close to 0 dBr for almost all of the icebergs, whereas the contribution of double bounce and volume scattering power is comparatively low. The NLOW (Figure 5.5, top) also has quite dominant surface scattering with a few outliers, whereas double bounce,

helix and volume scattering layer are generally lower. So, as with the other previous decompositions, surface scattering is highly dominant for both sets of icebergs. There are a few notable icebergs in both datasets that buck this trend. However, in general and specifically for the case of NLSI, dominant surface scattering is the trend.

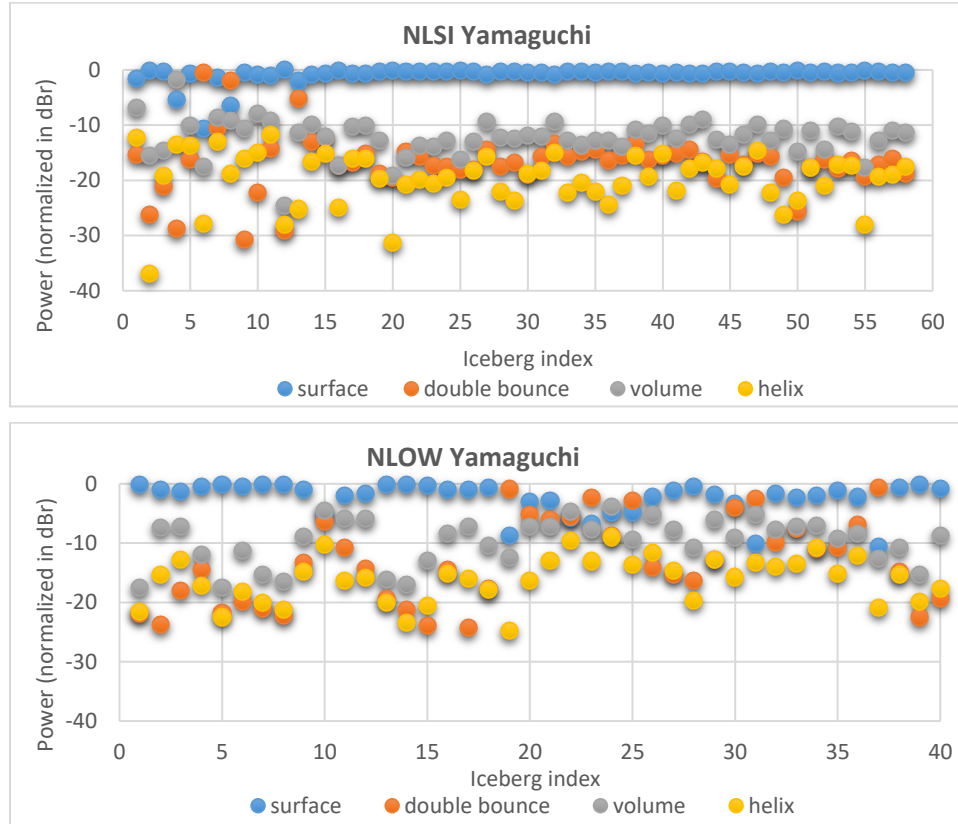


Figure 5.6: Yamaguchi decomposition of NLSI and NLOW group

5.2.1.5 Cloud-Pottier

Figure 5.7 shows the Cloude-Pottier decomposition result for NLSI and NLOW groups in terms of the H/α space. The left side of the figure (a) shows the decomposition output, while the right side of the figure (b) shows the interpretation legend. If we compare Figure 5.7(a) with the H/α plane in Figure 5.7(b), the Cloud-Pottier decomposition results for

NLOW and NLSI group can be readily explained. The zones are defined based on the entropy (H) and alpha angle (α) value (Lee & Pottier, 2009). The figure shows that almost all of the icebergs are located in zone 9, with some in zones 5 to 8.

In Figure 5.7(b), zone 9 represents low entropy surface scatter. Low entropy scattering occurs when the alpha value is less than 42.5° . This includes Bragg surface scattering and specular scattering phenomena which does not involve 180° phase inversion between HH and VV. A smooth physical surface is categorized in this zone. The fact that most bergs falls in this zone is again a case of the dominant surface scatter of both berg sample sets. Note that many of the icebergs in sea ice have a relatively higher alpha value for a given entropy than the icebergs in open water. As a consequence, the two datasets are highly separable in this zone. This makes sense because the sea ice clutter is much brighter than the open water clutter; given that it was challenging to separate the icebergs from the sea ice, it is likely that there may be some contamination of the iceberg target with sea ice clutter. This may be further exacerbated by the use of the speckle filter. More importantly however is the significant scattering interaction between the iceberg and the surrounding sea ice, leading to mixed scatterers. As shown by Scheuchl et al. (2001) and Pottier et al. (2003), C-Band backscatter of sea ice generally falls into Zones 9 and 6, with a higher entropy extent than the icebergs shown in Figure 5.7. To further illustrate this, a sea ice chip (Figure 5.8) was selected in the same scene as many of the icebergs. This chip was inspected to confirm that it did not contain any icebergs. As expected, this sea ice falls predominantly into Zones 9 and 6 and in particular, the zone 6 extent entropy extent is higher than the NLOW bergs. Figure 5.9 provides a H/α decomposition of a sea-ice chip

in the same scene as many of the NLSI icebergs. Thus, the sea ice is likely adding to the diffusivity of the surface scatter, producing a slightly higher alpha angle.

For the icebergs that lie in the other zones, it is likely that these icebergs have more complicated geometric shapes than the bergs in Zone 9, leading to higher alpha angles.

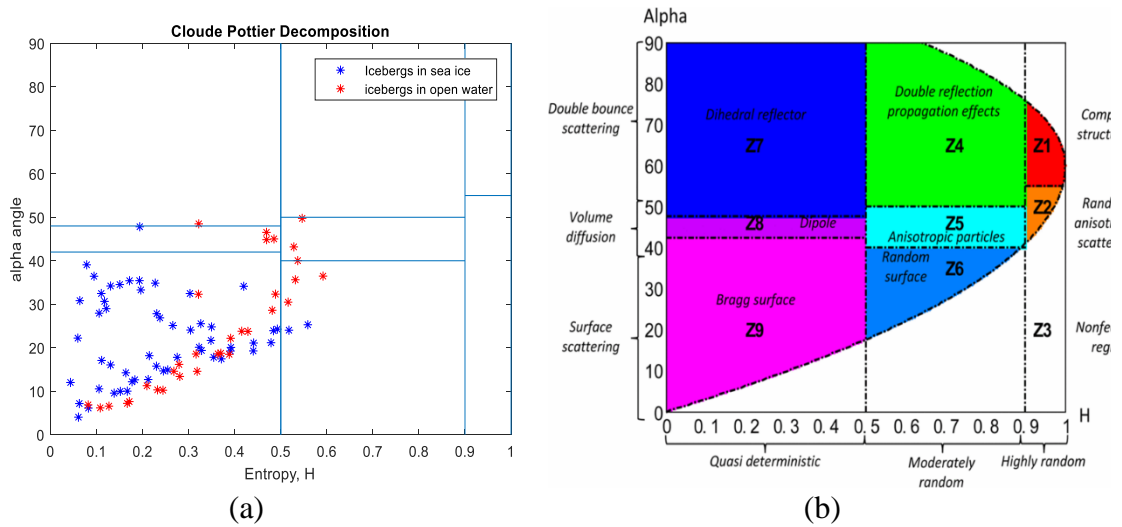
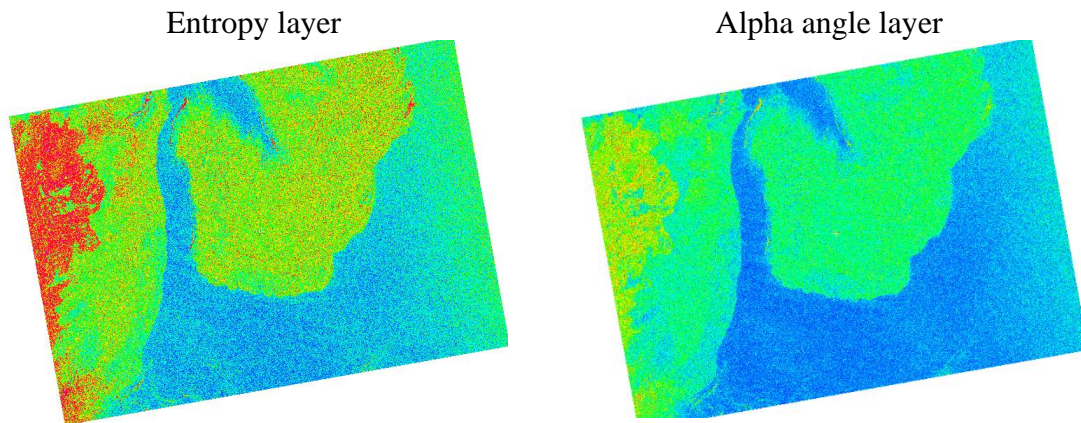
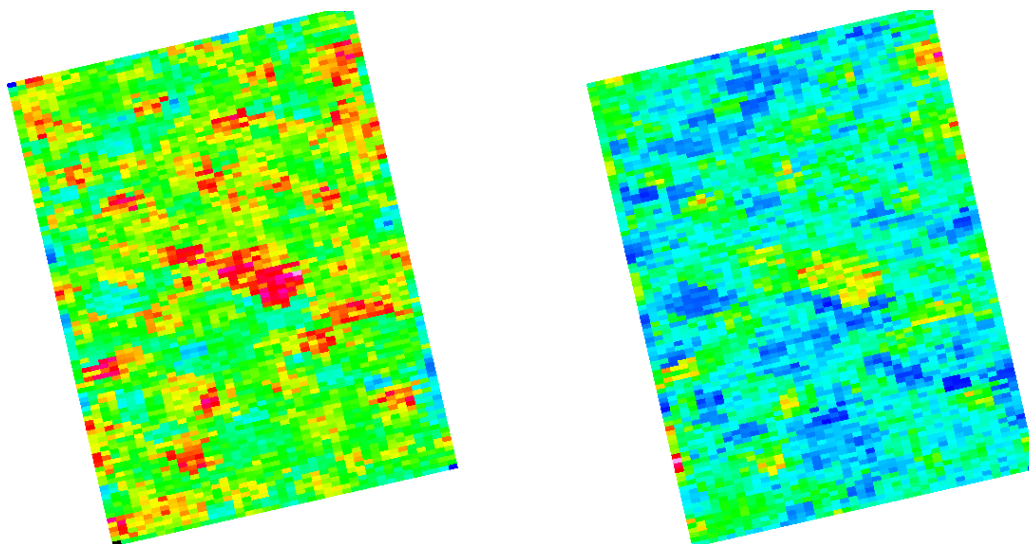


Figure 5.7 (a) Backscatter comparison using Cloudé-Pottier decomposition (b) H/α plane



RADARSAT-2 full scene (Red zone to the left is land and the green+red area in the center is sea ice)



Clip taken from sea ice covered area

Figure 5.8 Sea ice chip selected from RADARSAT-2 scene.

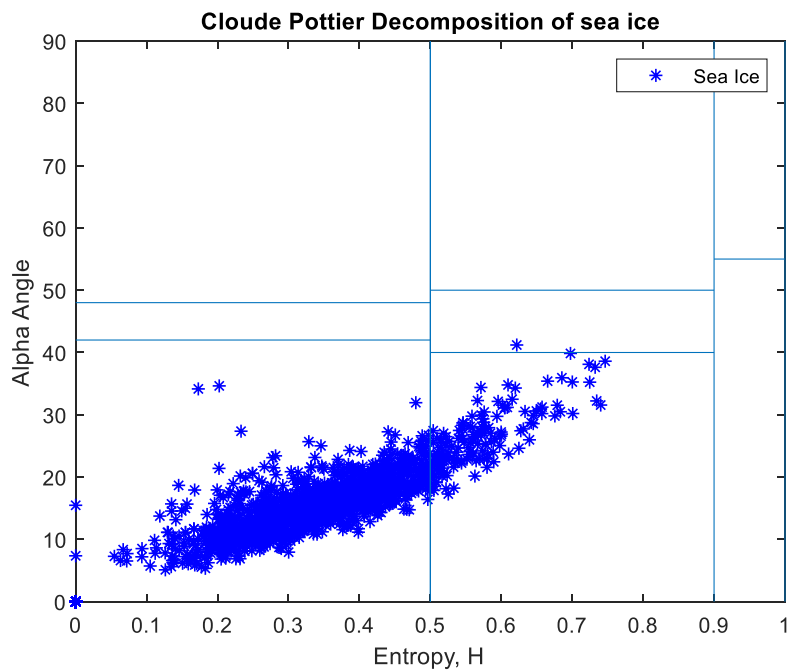


Figure 5.9 Cloud-Pottier decomposition of sea ice

5.2.2 Greenland versus Newfoundland icebergs (GLOW versus NLOW)

This section presents a comparison between icebergs from two different geographic locations, Greenland (GLOW) and Newfoundland (NLOW). This comparison is to determine whether there is any difference in backscatter between freshly calved bergs in the north and weathered bergs in the south. The exact same process was used here to generate the plots as was used in Section 5.2.1 for the NLSI and NLOW icebergs.

5.2.2.1 Pauli

Figure 5.10 illustrates the Pauli decomposition results; the NLOW Pauli plot is repeated here for comparison purposes to the GLOW icebergs. The figure shows that surface scattering is dominant for most of the Newfoundland icebergs (Figure 5.10; top) with only a few outliers. However, for Greenland icebergs, surface scattering is dominant for the majority of the icebergs but there are a larger number of outliers relative to the NLOW bergs (Figure 5.10 bottom). The power range for both cases is quite close and it is ranging from 0 to -25 dBr. The Pauli decomposition shows no obvious patterns or trends in the other two scatterers to differentiate the two datasets.

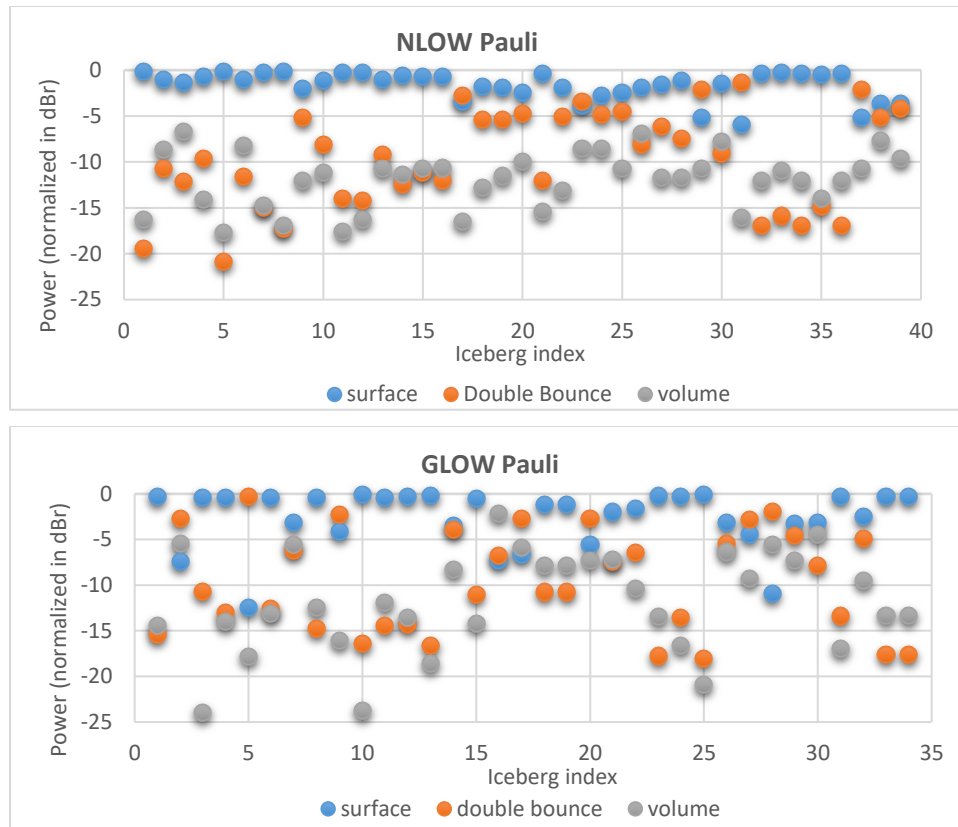


Figure 5.10: Pauli decomposition of NLOW and GLOW groups

5.2.2.2 Freeman-Durden

The Freeman-Durden decomposition results are shown in Figure 5.11, and the results for NLOW are repeated here for comparison purposes. These results are somewhat different from those for the Pauli decomposition for the GLOW dataset. Unlike Pauli, the Freeman-Durden decomposition tends to output higher volume scattering. A closer look at the Freeman-Durden results of GLOW icebergs (Figure 5.11 bottom), shows that surface scattering is not dominant for most of the icebergs and around 14 icebergs show dominant volume scattering, while the rest of the bergs are predominantly surface scattering.

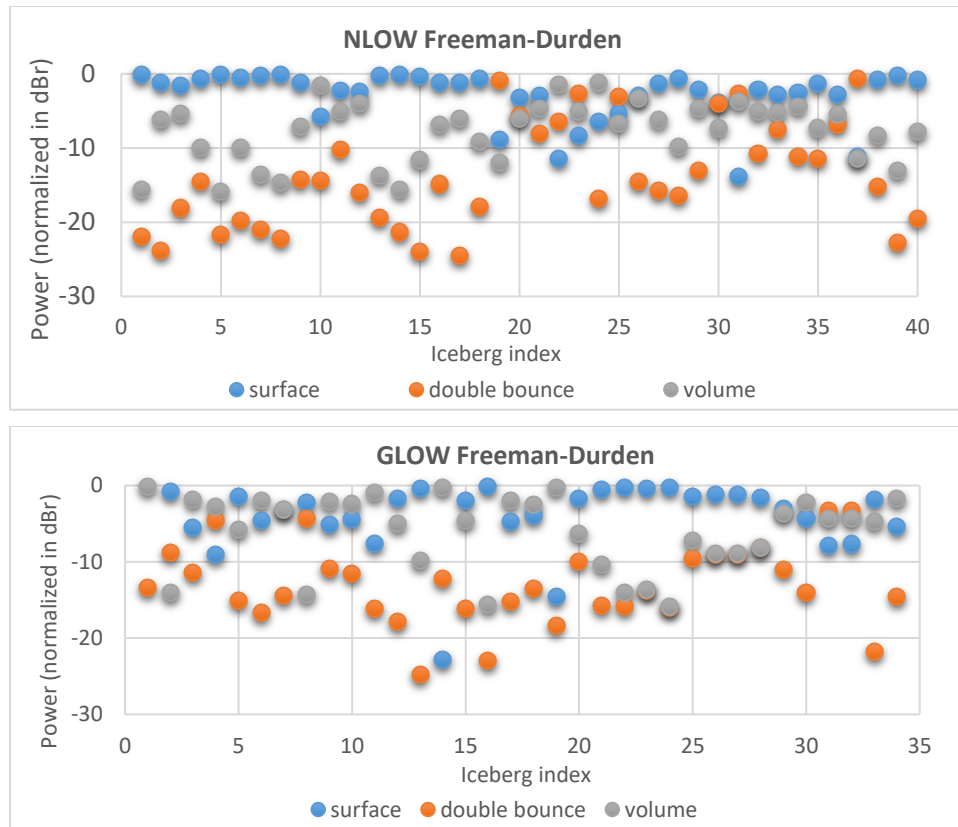


Figure 5.11: Freeman-Durden decomposition of NLOW and GLOW groups

5.2.2.3 van Zyl

Figure 5.12 shows the van Zyl decomposition results for NLOW and GLOW datasets, and again the NLOW plot is repeated here for comparison purposes. In the case of both GLOW and NLOW, the surface scattering power is very dominant; the range of surface scattering power is in between 0 to -5 dBr for both. In the case of volume and double bounce scattering, it is difficult to visually observe any notable trends or differences between the two datasets.

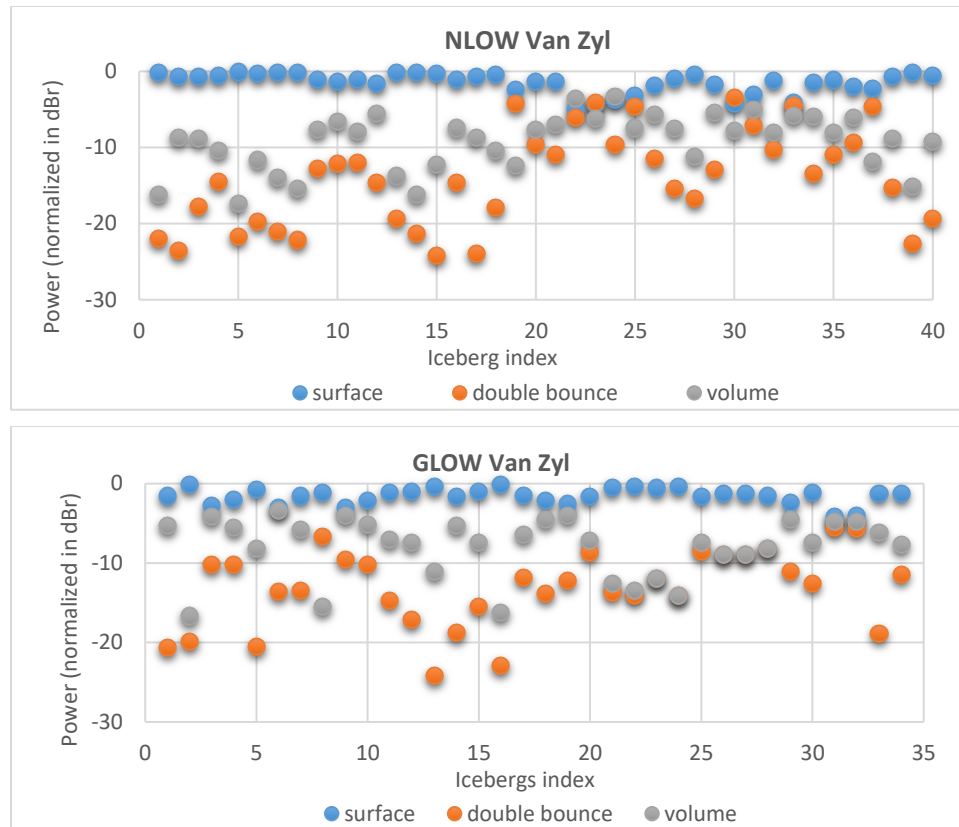


Figure 5.12 van Zyl decomposition results; Top: NLOW, Bottom: GLOW

5.2.2.4 Yamaguchi

Figure 5.13 shows the Yamaguchi decomposition results for NLOW and GLOW datasets, and again the NLOW plot is repeated here for comparison purposes. The figure shows that surface scattering is quite dominant over double bounce, helix and volume scattering for GLOW group. The surface scattering power range is in between 0 to -5 dBr for almost all of the icebergs, whereas the contribution of double bounce, volume and helix scattering power is comparatively low. The NLOW icebergs also have quite dominant surface scattering except few outliers, whereas double bounce, helix and volume scattering layer have no discernable pattern. As noted earlier, a few icebergs in open water tend to give

higher volume and double bounce scattering. However, in the case of both NLOW and GLOW icebergs, the dominant surface scattering is a trend but the double bounce, volume and helical power shows no pattern.

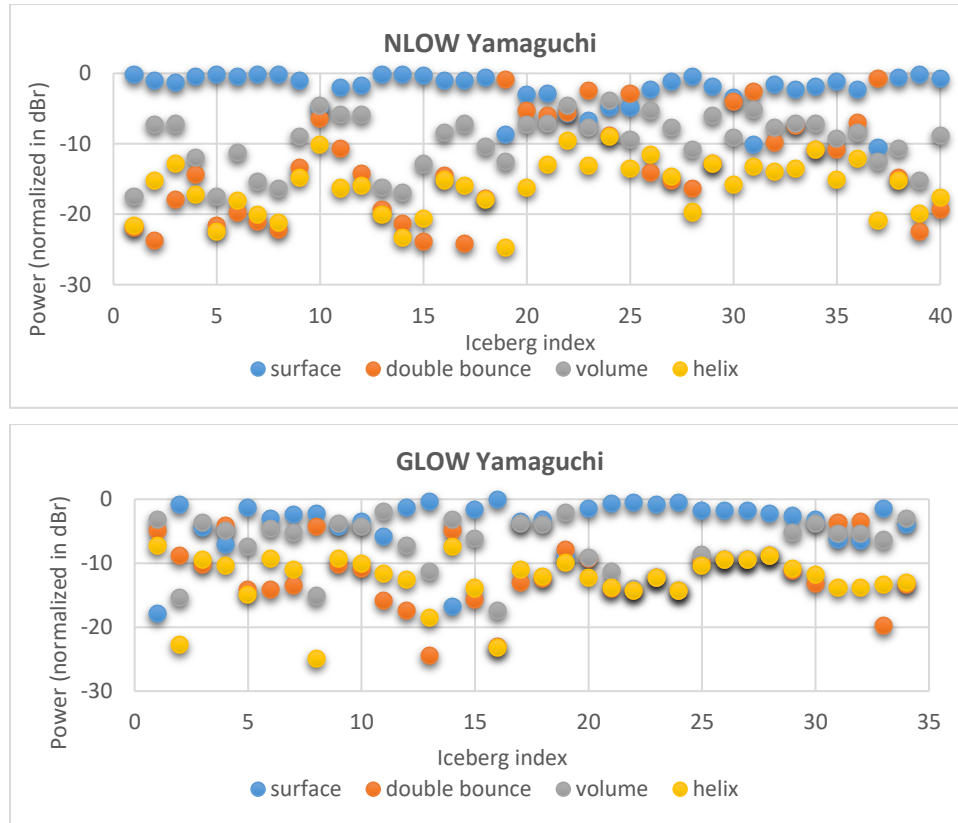
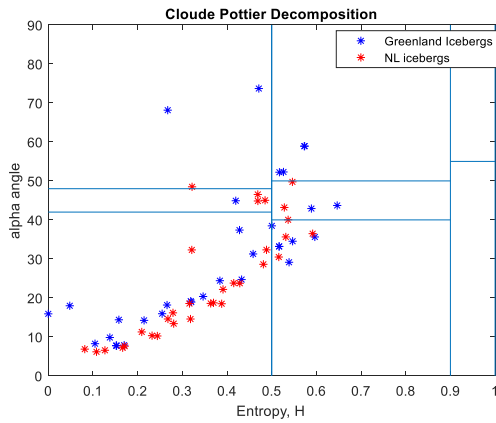


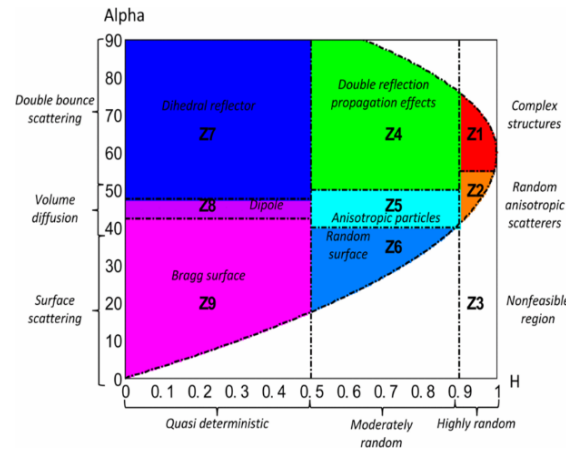
Figure 5.13 Yamaguchi decomposition results; Top: NLOW; Bottom: GLOW

5.2.2.5 Cloud-Pottier

Figure 5.14(a) shows a plot of the Cloud-Pottier decomposition for the NLOW and GLOW icebergs. As with Figure 5.7, the H and α is plotted for each iceberg to show the dominant scattering type of that entire berg. Figure 5.14(b) shows the various zone classes of the H/α plane for reference. As with the earlier decomposition, most of the icebergs are in zone 9, representing low entropy surface scatter.



(a)



(b)

Figure 5.14 (a) Scatter plot of Cloud-Pottier decomposition; (b) H/α plane

As most of the icebergs of both sets are in zone 9, this means that the majority of the icebergs produce dominant surface scattering. For the most part, the NLOW and GLOW bergs have similar entropy and alpha angles, however, unlike the NLSI bergs, there are no GLOW bergs that fall in the mid to upper left side of the zone. This gives further credence to the fact that the NLSI bergs may have been contaminated with sea ice scatter. Instead, there are number of GLOW bergs that instead lie in zones 4 to 8. For example, six NLOW icebergs and three GLOW icebergs are in zones 5 and 8 (α range 42° - 48°) and five GLOW icebergs are located in zones 7 and 4 with high alpha angles.

5.2.3 Statistical Comparison of Iceberg Groups

In the preceding sections, it was demonstrated that polarimetric SAR is useful for the identification of different scattering mechanisms that take place in icebergs. The major question for comparative analysis is whether there is a significant difference in the

scattering properties of these icebergs and whether or not these differences can be exploited for classification purposes.

The preceding sections have shown that there are some visual differences between the decomposition plots, but there is also significant overlap and much confusion would exist using simple classifiers. To determine if the scattering differences are significant, further statistical analysis is necessary. In this section, statistical tests are applied to the data to quantitatively identify these differences and similarities.

Scatter plot representations of the decomposition results in the earlier sections, clearly indicate that surface scattering is dominant than other three scattering power for almost all of icebergs. Nonetheless, there is still no strong evidence of visual differences between the sets of icebergs for double bounce, volume or helix scattering. Hence, to provide another approach to the statistical comparison of three groups of icebergs, box plots are shown below to compare the decomposition results for the NLSI, NLOW and GLOW subset of icebergs.

Figure 5.15 to Figure 5.18 show a comparison of icebergs in terms of the different polarimetric decompositions. The vertical axis represents the total power contribution of each scatterer in normalized linear form (not in dB like the previous scatter plot). Each box

represents the statistics of each scattering class based on decomposition results, as described in the Matlab™ user manual**:

- The tops and bottoms of each “box” are the 25th and 75th percentiles of the samples, respectively.
- The line in the middle of each box is the sample median. If the median is not centered in the box, it shows sample skewness.
- The whiskers are lines extending above and below each box and are drawn from the ends of the interquartile ranges to the furthest observations within the whisker length.
- Observations beyond the whisker length are marked as outliers and are displayed with a red + sign.
- Notches display the variability of the median between samples.

In the x-axis of these plots, S (red), D (green) and V (blue) are added to the class name to represent the surface, double bounce and volume scattering respectively. For example, NLOW_S is the surface scattering component of the Newfoundland icebergs in open water.

Figure 5.15 shows the first box plot for the Pauli decomposition. There is an obvious increase in the volume scattering from NLSI to GLOW, with the volume scattering being lowest in the NLSI subset. There is also an observable drop in surface scattering from the

** <https://www.mathworks.com/help/stats/box-plots.html>

NLSI bergs to the GLOW bergs. However, there are very little observable differences in the means of the double bounce of the helix scattering between the subsets.

All four plots (Figure 5.15-5.18) show a consistency between the differences and trends of the scatterers. The mean surface scattering power is the highest for NLSI and the lowest for GLOW for all decompositions, whereas, the mean volume scattering is the lowest in NLSI and the highest in the GLOW subset of icebergs. Observation of double bounce power among the plots shows very little change in all four decompositions.

In summary, all the decomposition results follow similar trends in comparing the subsets of icebergs. Surface scattering is shown to be the dominant scattering class regardless of the background clutter or the iceberg geographic location.

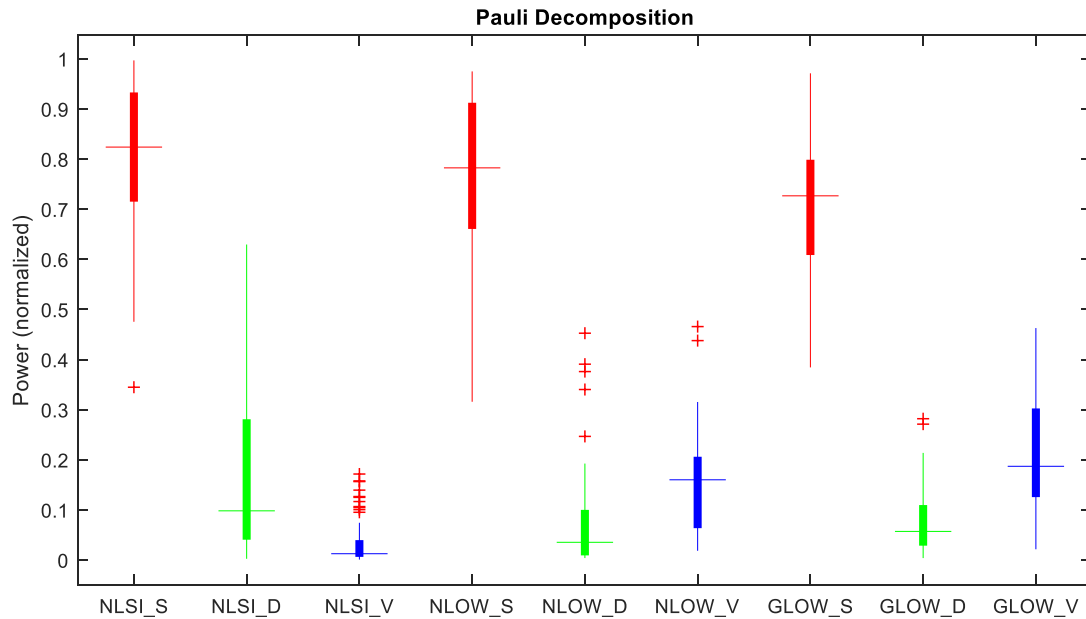


Figure 5.15 Box Plot representation of Pauli decomposition results

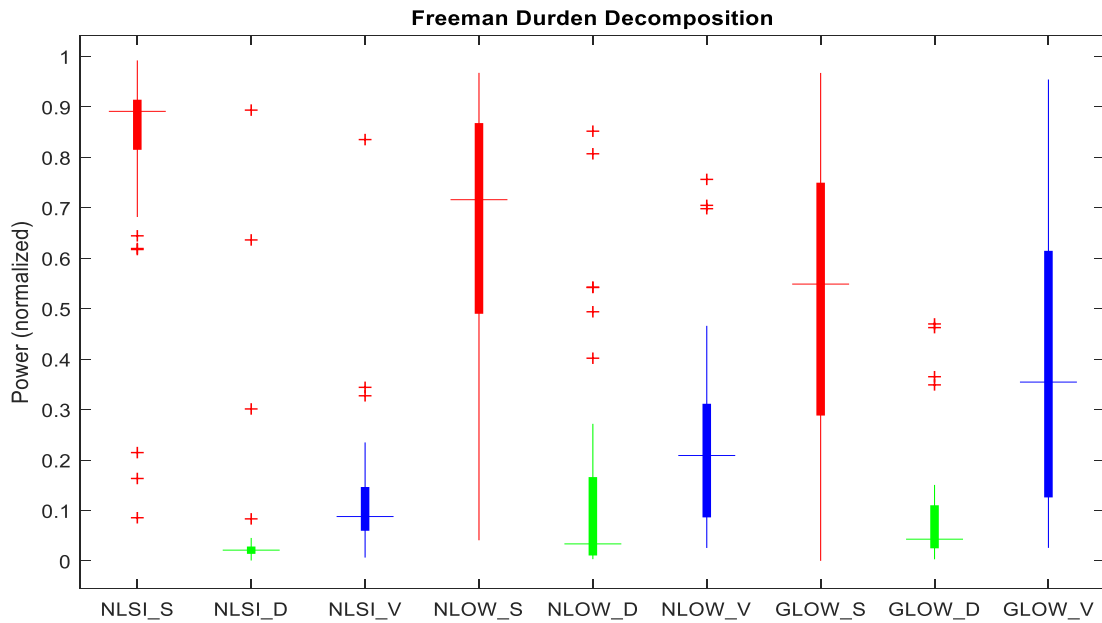


Figure 5.16 Box Plot representation of Freeman-Durden decomposition results

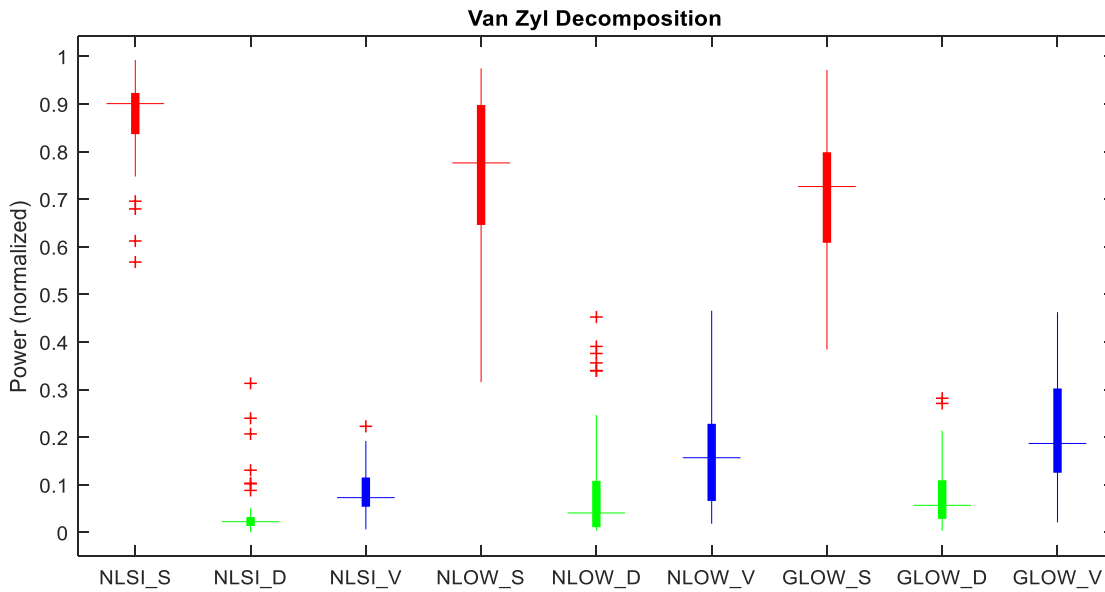


Figure 5.17 Box Plot representation of van Zyl decomposition results

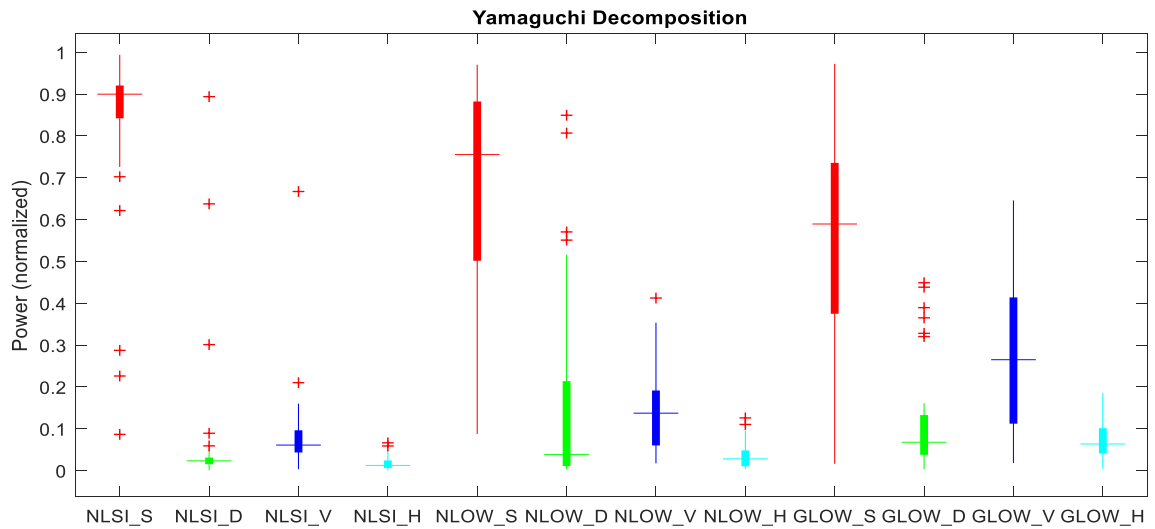


Figure 5.18 Box Plot representation of Yamaguchi decomposition results

5.3 Hypothesis Test

The boxplot results above essentially provide a graphical view of the hypothesis tests that are presented here. The next step is to compute the hypothesis tests to quantitatively show the similarities and differences between the data. T-tests have been used, including both the one tail and two tail T-test. T-tests have been performed on all the decompositions except Cloud-Pottier. The results of these tests have been shown in the following subsections.

5.3.1 Two Tail T-test

Hypothesis testing was performed based on the methods described in Chapter 2 and 4. The first test involves the NLSI and NLOW bergs, whereby the null hypothesis is that the datasets are statistically similar. Table 5.1 provides the two tail T-test results for NLSI and NLOW subsets. From the table below, we see that the T-test rejects the null hypothesis in

the case of surface and volume scattering for all four decompositions. In the case of double bounce scattering, all decompositions reject the null hypothesis except the Pauli. This is consistent with the boxplot results in Figures 5.15 to 5.18. Visually, the boxplot results show observable differences between the NLSI and NLOW scatterers, except in the case of the Pauli plot (Figure 5.15). To summarize, the mean of the power contribution from surface, double bounce, volume and helical scattering of these two datasets are shown to be statistically dissimilar that the mean backscattered power for each scattering component is statistically different between NL icebergs in sea ice and those in open water.

Table 5.1: Two tail T-test of NLSI and NLOW group

Decomposition.	Scatterer	t_{STAT}	t_{CRIT}	P	Observation
Pauli	Surface	2.015	2.008	0.0492	Rejected
	Double Bounce	-0.932	2.006	0.356	Accepted
	Volume	-3.830	2.002	0.000322	Rejected
Freeman-Durden	Surface	3.987	2.000	0.000184	Rejected
	Double Bounce	-2.139	1.999	0.0364	Rejected
	Volume	-3.624	1.9996	0.000593	Rejected
van Zyl	Surface	4.120	2.010	0.0001	Rejected
	Double Bounce	-2.720	2.009	0.0089	Rejected
	Volume	-4.084	2.009	0.000159	Rejected
Yamaguchi	Surface	3.859	2.000	0.000281	Rejected
	Double Bounce	-2.443	1.9996	0.0175	Rejected
	Volume	-3.467	1.992	0.000874	Rejected
	Helix	-3.636	2.007	0.000634	Rejected

The second test involves the NLOW and GLOW bergs, whereby the null hypothesis is that the datasets are statistically similar. Table 5.2 shows the T-test of NLOW and GLOW subsets. All four decomposition results of surface and double bounce scattering accept the

null hypothesis, which indicates that there is no significant difference between Greenland and Newfoundland icebergs in terms of these two backscatters. This is consistent with the boxplot results in Figures 5.15-5.18, which shows significant overlap in the interquartile ranges of these two scattering classes. In the case of volume scattering, the statistical tests are mixed; the null hypothesis is rejected for two of the decompositions (Freeman-Durden and Yamaguchi) and accepted for the other two (Pauli and van Zyl). Again, this is visually consistent with the boxplots. The null hypothesis is also rejected for helical scattering in the Yamaguchi decomposition. In summary, NLOW and GLOW datasets have no significant differences between surface and double bounce scattering but predominantly have significant differences in helical scattering. Volume scattering differences are sensitive to the decomposition, and given the mixed results, no definitive conclusion can be made for this scattering class.

Table 5.2 Two tail T-test of NLOW and GLOW

Decomposition	Scatter	t_{STAT}	t_{CRIT}	P	Observation
Pauli	Surface	1.127	2.003	0.265	Accepted
	Double Bounce	-0.466	1.999	0.643	Accepted
	Volume	-1.889	2.015	0.0656	Accepted
Freeman-Durden	Surface	1.629	1.995	0.108	Accepted
	Double Bounce	1.0087	1.998	0.317	Accepted
	Volume	-2.654	2.005	0.0104	Rejected
van Zyl	Surface	0.724	1.993	0.472	Accepted
	Double Bounce	0.882	1.999	0.381	Accepted
	Volume	-1.838	1.997	0.0705	Accepted
Yamaguchi	Surface	1.912	1.994	0.0599	Accepted
	Double Bounce	0.741	1.997	0.462	Accepted
	Volume	-3.207	2.008	0.00232	Rejected
	helix	-4.170	2.004	0.000109	Rejected

5.3.2 One Tail T-Test

As described earlier, the one tail T-test provides further insight whenever the two tail T-test observes significant differences between classes – in this case, the scattering classes of the iceberg subsets.

In the case of NLSI versus NLOW bergs, Table 5.1 shows that only one of the two tail test was accepted (Pauli Double Bounce). As such, one tail tests were conducted on all of the decomposition outputs, except that one case.

Examining the boxplots, it is clear that the surface scattering of the NLSI bergs appears to be higher than that of the NLOW bergs for all of the decompositions. Therefore, for surface scattering, the null and alternate hypotheses were established as follows.

$$H_0: \text{NLSI}_s \leq \text{NLOW}_s$$

$$H_a: \text{NLSI}_s > \text{NLOW}_s$$

Table 5.3 details the one tail T-test results, which shows the alternate hypothesis is accepted for surface scattering.

Table 5.3 One tail T-test of the surface scattering of NLSI and NLOW group

Decomposition	t_{STAT}	t_{CRIT}	P	Observation
Pauli	2.015	1.675	0.0246	Rejected
Freeman-Durden	3.987	1.671	9.200E-05	Rejected
van Zyl	2.015	1.675	0.0246	Rejected
Yamaguchi	3.859	1.671	0.000141	Rejected

In the case of the other three scattering types, the NLSI bergs are observed to have lower scattering than the SLOW bergs, based on their means. As a consequence, for these scatterers, the following null and alternate hypotheses are formulated:

$$H_0: \text{NLSI}_X \geq \text{NLOW}_X$$

$$H_a: \text{NLSI}_X < \text{NLOW}_X$$

Table 5.4 shows the one tail T-test results for each of these scattering types. In null hypothesis is rejected for all of these cases, therefore NLSI scattering proportion are less than NLOW scattering proportion for double bounce, volume and helix scattering.

Table 5.4 One tail T-test of the double bounce, volume and helix scattering of NLSI and NLOW group

Decomposition	Scatter	t_{STAT}	t_{CRIT}	P	Observation
Freeman-Durden	Double Bounce	-2.137	1.670	0.0182	Rejected
van Zyl	Double Bounce	-2.139	1.670	0.0182	Rejected
Yamaguchi	Double Bounce	-2.720	1.676	0.00446	Rejected
Pauli	Volume	-3.830	1.672	0.000161	Rejected
Freeman-Durden	Volume	-3.624	1.670	0.000297	Rejected
van Zyl	Volume	-4.084	1.676	7.977E-05	Rejected
Yamaguchi	Volume	-3.467	1.665	0.000437	Rejected
Yamaguchi	Helix	-3.636	1.675	0.000317	Rejected

Thus, in summary, the percentage of surface scattering power in NLOW icebergs is higher than NLSI icebergs and is lower for all other scattering types.

In the case of NLOW versus GLOW bergs, only three different cases were rejected. As a consequence, only those three cases were considered for the one tailed test. In all three

cases, the boxplots reveal that the NLOW scattering is less than the GLOW scattering. As such, the hypothesis testing is set up as follows:

$$H_0: \text{NLOW}_x \geq \text{GLOW}_x$$

$$H_a: \text{NLOW}_x < \text{GLOW}_x$$

Table 5.5 shows the output of the one tail T-test results of NLOW and GLOW groups. As can be seen in the table, all scattering classes reject the null hypothesis. Thus, we can conclude that both volume and helical scattering from the GLOW icebergs are greater than the NLOW icebergs just in the case of Freeman-Durden and Yamaguchi decomposition. Overall, NLOW and GLOW bergs don't have significant differences.

Table 5.5: One tail T-test of NLOW and GLOW group

Decomposition	Scatter	t_{STAT}	t_{CRIT}	P	Observation
Freeman-Durden	Volume	-2.654	1.674	0.00522	Rejected
Yamaguchi	Volume	-3.207	1.675	0.00116	Rejected
	Helix	-4.170	1.673	5.45E-05	Rejected

5.4 Summary

The following is a summary for the comparison of the T-test results for both sets of icebergs.

Newfoundland icebergs in Sea Ice versus in Open Water: Significant differences have been found in all scattering classes between the two datasets, with only one outlier in one decomposition (Pauli Double Bounce). Furthermore, surface scattering is dominant over

double bounce, helical and volume scattering for most of the icebergs in both groups. NLSI icebergs tend to give higher proportion of surface scattering compared to the NLOW icebergs, while NLOW icebergs give higher proportion of volume scattering than NLSI icebergs.

Greenland versus Newfoundland Icebergs: No significant differences have been found between Greenland and Newfoundland icebergs in terms of surface and double bounce scattering. Surface scattering is dominant for most of the icebergs for both groups. Significant differences have been found in volume scattering for half of the polarimetric decompositions. Significant differences were also found in the helical scattering in both groups. Greenland icebergs having higher proportion of volume and helical scattering power than the Newfoundland icebergs. In summary, scattering is predominantly similar between Newfoundland and Greenland bergs, with a few exceptions.

5.5 Discussion

Radar backscatter is a complex phenomenon and sensitive to a large number of properties. In the case of point targets such as icebergs, geometric shape, surface roughness, dielectric constant and local incident angle all have significant impacts on the backscatter. Among the sensor parameters, incident angle, wavelength, look direction and polarization all have significant contributions (Lee & Pottier, 2009).

Most icebergs can be well visualized in both co and cross-polarized SAR images at C-Band. However, for a number of icebergs in sea ice, an overlap (obscurity) of their radar backscatter was found that lead to the masking of those icebergs in the clutter. Given the

lower contrast between icebergs and sea ice, it is therefore speculated that iceberg ‘pixels’ in SAR imagery can be contaminated with sea ice backscatter, even when the background sea ice is masked out from the image.

The first major observation is the significance of the surface scatter from icebergs at C-band. As reported by Haykin et al., (1994), radar backscatter from an iceberg arises from both surface and volume scattering and the volume scattering is dominant. Clearly this assertion is a generalized statement, but from the analysis presented here, the dominance of volume scattering does not hold at C-Band. This is in spite of the fact that C-band penetrates significantly into glacial ice by some 3-14 meters at 5.4 GHz depending on the specific ice properties (Lewis et al., 1987). Thus, weathering, iceberg geometry and the interaction between the iceberg and its background (sea ice, ocean) are speculated to play a significant role in contributing to this surface scatter. The dominant surface scatter of icebergs is also reported by Dierking & Wesche (2014), who suggested that actively melting bergs produce dominant surface scatter. This assertion was confirmed by Ferdous et al (2018; 2019) using an electromagnetic backscatter model with comparisons to sample SAR datasets of icebergs. The image acquisition details presented in Table 3.1 show that all icebergs in question were subject to above freezing temperatures (8° C to 16° C range). Therefore, there is a strong possibility of the existence of a meltwater layer on the surface of the icebergs. This would lead to a dominant backscatter surface backscatter, since the melt water layer will result in a highly reflective surface. In summary, it is observed that surface scattering is highly dominant over double bounce and volume scattering.

The second major observation is that surrounding clutter plays a significant role in iceberg backscatter. The two tail T-tests show that icebergs in open water have a statistically different backscatter proportionality than icebergs in sea ice for all scattering classes. The surrounding clutter from the sea ice likely contributes to that fact. It is speculated that there is a significant interaction of scatter between the iceberg and its surrounding clutter, leading to mixed scattering. Icebergs are composed of ice of freshwater origin while sea ice is of saline water origin. Thanks to the brine content of the sea ice, its dielectric strength will thus be higher for sea ice than for glacial ice. The dielectric constant of glacial ice is 3.15 and for sea ice the range is 3.5-5, depending on sea ice type (Haykin et al. 1994). A scatterer with high dielectric constant produces a larger amount of backscatter and is thus brighter in a radar image than a scatterer with a low dielectric constant. Given the low contrast between the icebergs and sea ice in the datasets presented here, it is possible that some of the masked iceberg targets are contaminated with some sea ice pixels. However, it is unlikely that the contamination of sea ice with iceberg pixels is a significant contribution to the scatter. More likely, the answer comes from the scattering interaction of sea ice and icebergs, resulting in higher overall surface scatter from the icebergs. As sea ice scatter will be dominantly a surface scattering mechanism, the interaction of this scatter with the iceberg geometry will likely result in higher overall iceberg surface scatter. This trend holds though from the boxplots and hypothesis testing, with the icebergs in sea ice having higher surface scattering relative to the icebergs in open water.

The hypothesis tests also found a significant difference in the volume scattering of icebergs in sea ice and icebergs in open water, with the NLOW bergs having the higher proportion

of backscatter. Given that it is speculated that there is significant interaction of the icebergs with its surrounding clutter, a contributing factor is likely the higher diffusivity of the scatter from the ocean surface, relative to sea ice. Specifically, the diffuse nature of open water clutter and the resulting interaction with the iceberg geometry likely results in a higher volume scatter for icebergs in open water. In comparison, the dominant surface scattering of sea ice likely results in less volumetric scattering interactions between icebergs and sea ice, thus resulting in a lower total volume scatter from the icebergs when in the presence of sea ice. It is generally assumed that volume scattering originates from within the volume of the iceberg; however, in this case there might be other contributions, such as the diffuse scatter from the ocean interacting with the iceberg geometry. For example, there might be some ocean to iceberg dihedral scattering that, when summed up in a superimposition of scattering from multiple ocean waves, can be classified as volume scattering. Sometimes this can occur because double bounce or dihedral and volume scattering both are in multiple scattering, they can be misclassified. Theoretically, when the dihedral reflector is at a 45° angle, its reflection is predominantly visible in the HV polarization which contributes to volume scattering. As suggested for surface scattering, there may also be some contamination of iceberg and background pixels (sea ice and ocean) and thus there may be a small contribution to the high levels of volume scattering in the open water case. As indicated with the icebergs in sea ice, speckle filtering might also have some contributions to this effect.

Note that the surrounding clutter plays a significant role in iceberg backscatter which is supported by other ongoing research on iceberg backscatter. Specifically, Ferdous et al

(2019) showed, using a 3D electromagnetic backscatter model, that there is significant interaction between icebergs and the surrounding ocean, resulting in significant changes to iceberg backscatter with varying ocean clutter levels.

A third major observation is the differences in backscatter with geographic region. These differences can only be categorized as minor primarily because only three of the T-tests showed differences with any statistical significance. While there were no demonstrable statistical differences, the boxplots showed a decreasing trend in proportion of surface scatter from the Greenland bergs to the Newfoundland bergs. The boxplots also showed an increasing trend in the proportion of volume scatter from Greenland to Newfoundland bergs. These scattering characteristics are likely the result of iceberg weathering. Specifically, it is speculated that the highly weathered bergs in Newfoundland leads to increased proportion of surface and decreased volume scatter. It is also possible that internal temperatures of the Southern Newfoundland bergs are higher than the freshly calved Greenland bergs in the North; those higher internal temperatures would lead to increased microwave attenuation and less volume scattering relative to the colder Greenland bergs.

The differences in backscatter highlighted above have significant consequences for other projects involving iceberg backscatter analysis. In this case, icebergs in open water cannot be considered as proxies for icebergs in sea ice. The same can be said for Greenland and Newfoundland icebergs. As a consequence, machine learning algorithms that rely on

pattern recognition may have to train different algorithms for recognizing icebergs in different clutter conditions and different locations.

The analysis presented here provides little obscurity about the compelling usefulness of polarimetric radar measurements for inferring scattering mechanisms in icebergs. The principal challenge is that the polarimetric signatures of some icebergs overlap with those of sea ice and that iceberg signatures are highly variable, depending on environmental conditions, radar parameters, and imaging geometries, as discussed above. This means, for example, that it is difficult to base the separation between icebergs and sea ice on signature thresholds. This could be a widespread issue for detection and discrimination of all icebergs within a sea ice cover, even when polarimetric data are available.

6. Conclusion

Polarimetric signatures and scattering properties of icebergs in sea ice, open water and from different regions were investigated. RADARSAT-2 C-band images have been acquired over the Atlantic Ocean close to the province of Newfoundland and Labrador, Canada and Greenland. The analysis of the co and cross-polarization scattering indicates that icebergs in sea ice have a lower HV contribution than icebergs in open water. If the incidence angle ranges are considered, icebergs in sea ice are generally more distinguishable in the HH channel, whereas icebergs in open water are more distinguishable in the HV channel. All the decomposition results, including Pauli, Freeman-Durden, van Zyl, Yamaguchi and Cloud-Pottier, indicate dominant proportion of surface scattering among all iceberg targets.

Hypothesis test results have shown considerable differences in all scattering mechanisms between icebergs in sea ice and in open water, with only one exception. Icebergs in open water produce a higher proportion of volume scattering, while icebergs in sea ice produce a higher proportion of surface scattering. However, differences have are also visible in the scattering between Newfoundland and Greenland icebergs, however these should be categorized as minor because only three T-tests showed differences with any statistical significance. The relative contribution of each scatter mechanism varies, depending on the weather conditions (wind, sunshine, temperature), the geometrical shape of the iceberg, radar parameters and imaging geometry.

SAR detection of icebergs is a challenge in situations with high iceberg density, heterogeneous background clutter and sea ice. Detection of an iceberg in the sea ice pack

is particularly problematic because of the obscurity between iceberg and sea ice SAR backscatter. Iceberg detection from sea ice is a significant challenge, as sea ice produces strong backscatter in a SAR image. The statistical analysis presented here is provided to refine the technique of detecting icebergs more precisely in the presence of sea ice.

6.1 Limitations

While this study makes significant contributions in the context of C-band microwave backscatter from icebergs, there are some limitations that should be addressed in future studies. This study is limited to iceberg backscatter with a relatively low incidence angle range and thus higher incident angles should be investigated to determine if the trends are consistent. As this study is a comparative study, the analysis of a higher number of icebergs would be more helpful to provide further confidence in the results. Another limitation of this study is the thresholding technique used to separate iceberg backscatter from sea ice. It was challenging to identify and separate the exact iceberg pixels from the surrounding clutter, so there is a possibility that there were some iceberg pixels that have been masked out as clutter.

Furthermore, the use of the speckle filter in the analysis may lead to some smearing of the iceberg targets, which may account for the observed backscatter contamination effects, particularly in the case of icebergs in sea ice. And finally, the relative power analysis that was performed with the decompositions (i.e., the use of dBr) prevents the observation of absolute backscatter differences between decompositions. These effects may warrant further consideration in future research.

6.2 Future Work

It is an ultimate goal to have the capability of passing unknown SAR targets to a classification model that makes an automated decision on the target type (iceberg, ship, clutter, etc.). To discriminate icebergs from other ocean targets, automated classification is important. Nonetheless, as this study points out, first there is a need to know the iceberg properties from different locations and in different conditions. If icebergs from different locations and in different conditions exhibit distinguishable properties, it is mandatory to train different classification algorithms based on their properties. This will lead to classifiers with greater skill in determining the target type. As significant differences between icebergs in sea ice and in open water have been found, this should be considered during classification and different classifiers need to be developed for these two circumstances. However, as the RADARSAT-2 images used in this study were acquired around the summer season in the lower incident angle range, a similar study should be done for RADARSAT-2 images acquired in winter and with wider incident angle ranges. One future step following this study is to generate a classification algorithm to classify icebergs and other targets from SAR images based on the results obtained here. In particular, parallel studies are presently being conducted to apply machine learning algorithms (e.g., artificial neural networks) to help distinguish and discriminate iceberg targets in both open water and in sea ice in different SAR image types. Machine learning could also be applied for other applications, such as in the determination of better and more robust iceberg edge detection techniques that provide a more accurate estimate of iceberg size. In this study, a general-purpose thresholding technique has been used and there is a possibility to lose

target pixels or contaminate the target data with clutter pixels. More robust and objective iceberg edge detection techniques will make a significant contribution to the study of iceberg backscatter in future projects.

7. References

- Akbari, V., & Brekke, C. (2018). Iceberg Detection in Open and Ice-Infested Waters Using C-Band Polarimetric Synthetic Aperture Radar. *IEEE Transactions on Geoscience and Remote Sensing*, 56(1), 407-421.
- Brown, M. B., & Forsythe, A. B. (1974). Robust T-tests for the equality of variances. *Journal of the American Statistical Association*, 69(346), 364-367.
- Cloude, S. R., & Pottier, E. (1997). An entropy based classification scheme for land applications of polarimetric SAR. *IEEE Transactions on Geoscience and Remote Sensing*, 35(1), 68-78.
- Cloude, Shane, R, Pottier, Eric and Boerner, Wolfgang M (2002). Unsupervised image classification using the entropy/alpha/anisotropy method in radar polarimetry. *NASA-JPL, AIRSAR-02 Workshop*, p. 04-06.
- Dierking, W., & Wesche, C. (2014). C-Band radar polarimetry—useful for detection of icebergs in sea ice? *IEEE Transactions on Geoscience and Remote Sensing*, 52(1), 25-37.
- Eadie, W. T., Drijard, D., & James, F. E. (1971). Statistical methods in experimental physics. *Amsterdam: North-Holland*, 1971.
- Ferdous, M. S., Himi, U.H., McGuire, P., Power, D., Johnson, T., Collins, M. A. (2018). A Comparison of Numerically Modelled Iceberg Backscatter Signatures with

- Sentinel-1 C-Band Synthetic Aperture Radar Acquisitions. *Canadian Journal of Remote Sensing*, pp. 1-11, 2018.
- Ferdous, M. S., Himi, U.H., McGuire, P., Power, D., Johnson, T., Collins, M. A. (2019). A Comparison of an Iceberg Electromagnetic Backscatter Model with C-Band SAR Data at Varying Wind Conditions and Iceberg Orientations; submitted for publication.
- Freeman, A., & Durden, S. L. (1998). A three-component scattering model for polarimetric SAR data. *IEEE Transactions on Geoscience and Remote Sensing*, 36(3), 963-973.
- Haykin, S., Lewis, E. O., Raney, R. K., & Rossiter, J. R. (1994). *Remote sensing of sea ice and icebergs* (Vol. 13). John Wiley & Sons.
- Howell, C., Bobby, P., Power, D., Randell, C., & Parsons, L. (2012). Detecting icebergs in sea ice using dual polarized satellite radar imagery. In *10th Int'l Conference and Exhibition on Performance of Ships and Structures in Ice (ICETECH)*.
- Howell, C., Power, D., Lynch, M., Dodge, K., Bobby, P., et al. (2008). Dual polarization detection of ships and icebergs-recent results with ENVISAT ASAR and data simulations of RADARSAT-2. In *Geoscience and Remote Sensing Symposium, 2008. IGARSS 2008. IEEE International* (Vol. 3, pp. III-206).
- Kim, J. W., Kim, D. J., Kim, S. H., & Hwang, B. J. (2011). Iceberg detection using full-polarimetric RADARSAT-2 SAR data in West Antarctica. In *Synthetic*

Aperture Radar (AP SAR), 2011 3rd International Asia-Pacific Conference on (pp. 1-4)

Lane, K., Power, D., Chakraborty, I., Youden, J., Randell, C., et al. (2002). RADARSAT-1 synthetic aperture radar iceberg detection performance ADRO-2 A223. In *Geoscience and Remote Sensing Symposium, 2002. IGARSS'02. 2002 IEEE International* (Vol. 4, pp. 2273-2275).

Lee, J. S., & Pottier, E. (2009). *Polarimetric radar imaging: from basics to applications*. CRC press.

Lewis, E., Currie, B., and Haykin, S. (1987). *Detection and Classification of Ice*, John Wiley and Sons Inc., New York, p. 156.

Massey Jr, F. J. (1951). The Kolmogorov-Smirnov test for goodness of fit. *Journal of the American statistical Association*, 46(253).

Morena, L. C., James, K. V., & Beck, J. (2004). An introduction to the RADARSAT-2 mission. *Canadian Journal of Remote Sensing*, 30(3), 221-234.

Pottier, E., Ferro-Famil, L., Allain, S., Cloude, S., Hajnsek, I., et al. (2009). Overview of the PolSARpro V4. 0 software. The open source toolbox for polarimetric and interferometric polarimetric SAR data processing. In *Geoscience and Remote Sensing Symposium, 2009 IEEE International, IGARSS 2009* (Vol. 4, pp. IV-936). IEEE.

- Power, D., Youden, J., Lane, K., Randell, C., & Flett, D. (2001). Iceberg detection capabilities of RADARSAT synthetic aperture radar. *Canadian Journal of Remote Sensing*, 27(5), 476-486.
- Richards, J. A. (2009). *Remote sensing with imaging radar* (Vol. 1). Berlin: Springer.
- Scheuchl, B., Flett, D., Caves, R., & Cumming, I. (2004). Potential of RADARSAT-2 data for operational sea ice monitoring. *Canadian Journal of Remote Sensing*, 30(3), 448-461.
- Scheuchl, B., Caves, R., Cumming, I., & Staples, G. (2001). $H/A/\alpha$ -based classification of sea ice using SAR polarimetry, *Proc. 23rd Can. Symp. Remote Sens.*, p. 21-24.
- Skolnik, Merrill I. 2008. *Radar Handbook*, Third Edition. McGraw Hill Professional.
- Turkar, V., & Rao, Y. S. (2011). Applying coherent and incoherent target decomposition techniques to polarimetric SAR Data. In *Proceedings on the IJCA International Conference on Technology Systems and Management* (pp. 23-29).
- Ulaby, F. T., Long, D. G., Blackwell, W. J., Elachi, C., et al. (2014). *Microwave radar and radiometric remote sensing* (Vol. 4, No. 5, p. 6). Ann Arbor: University of Michigan Press.

- van Zyl, J. J. (1989). Unsupervised classification of scattering behavior using radar polarimetry data. *IEEE Transactions on Geoscience and Remote Sensing*, 27(1), 36-45.
- van Zyl, J. J., Arii, M., & Kim, Y. (2008). Requirements for model-based polarimetric decompositions. In *7th European Conference on Synthetic Aperture Radar* (pp. 1-4). VDE.
- van Zyl, J. J., Arii, M., & Kim, Y. (2011). Model-based decomposition of polarimetric SAR covariance matrices constrained for nonnegative eigenvalues. *IEEE Transactions on Geoscience and Remote Sensing*, 49(9), 3452-3459.
- Wesche, C., & Dierking, W. (2012). Iceberg signatures and detection in SAR images in two test regions of the Weddell Sea, Antarctica. *Journal of Glaciology*, 58(208), 325-339.
- Yamaguchi, Y., Moriyama, T., Ishido, M., & Yamada, H. (2005). Four-component scattering model for polarimetric SAR image decomposition. *IEEE Transactions on Geoscience and Remote Sensing*, 43(8), 1699-1706.

Appendix I

Image Processing Algorithm

MATLAB Code:

```
i=1;

Str=num2str(i);

filename=strcat('IB',Str,'_intensity.tif');

I=imread(filename);

HH=I(:,:,1);

[t th]= my_clutter_clip(HH,3);

mask=(HH>=th);

function [imOUT th]=my_clutter_clip(imIN,sd_factor)

% this function will give the output image as clutter masked

mu=(mean2(imIN));

st_dev=std2(imIN);
```

```
th=mu+st_dev*13;

MASK=imIN>th;

imOUT=imIN;

imIN=imIN.*(MASK==0);

imIN_dummy=reshape(imIN,1,[]);

imIN_dummy(imIN_dummy==0)=[];

mu=mean2(imIN_dummy);

st_dev=std2(imIN_dummy);

th=mu+sd_factor*st_dev;

MASK_dummy=imIN>th;

MASK=xor(MASK,MASK_dummy);

imOUT=imOUT.*MASK;

end
```

Appendix II

Decomposition Algorithm

This appendix only provides the code for pauli decomposition as it is handwritten. The Freeman-Durden, van Zyl, Yamaguchi decompositions have been applied using SNAP ESA and Cloud-Pottier has been implemented using PCI Geomatica tool.

Pauli Decomposition

Function

```
[alpha, beta, gamma]=my_pauli(SHH,SHV,SVH,SVV,mask)

alpha=(SHH(:, :, 1)+SVV(:, :, 1))./sqrt(2);

beta=(SHH(:, :, 1)-SVV(:, :, 1))./sqrt(2);

gamma=sqrt(2).*SHV(:, :, 1);

alpha=(abs(alpha)).^2;

beta=(abs(beta)).^2;

gamma=(abs(gamma)).^2;

alpha=alpha.*mask;

beta=beta.*mask;
```

```
gamma=gamma.*mask;
```

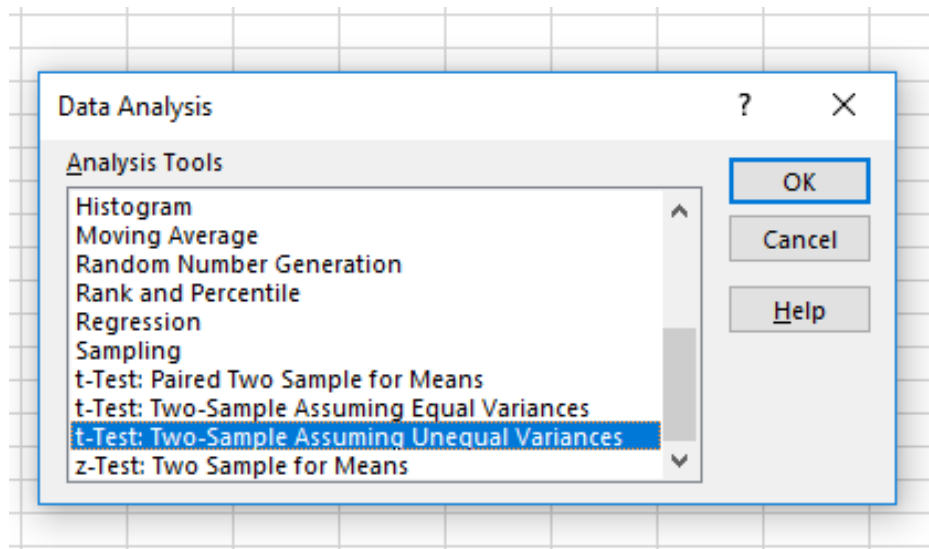
```
end
```

Appendix III

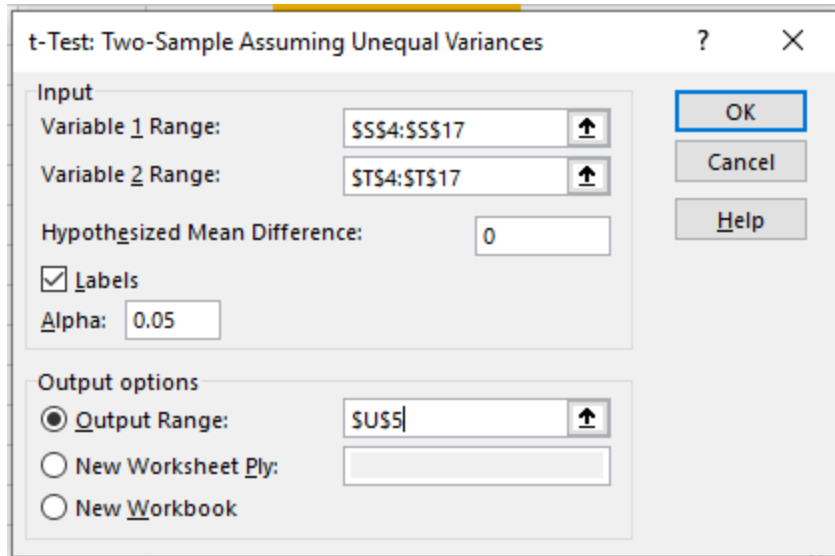
Statistical Test

T-test: Microsoft excel have been used to implement the statistical T-test. The following step shows one example of implementing T-test in Excel. Two samples are volume scattering of icebergs and open water using Pauli. The steps are following

Step 1: The algorithm has been selected from the **Data Analysis** tab. Here Two-Sample Assuming Unequal variances have been used as the variances of two samples are not equal.



Step 2: The input variables have been loaded in variable 1 and variable 2 range. Hypothesis mean difference was set to zero. The significance level was set to 0.05.



Once hit 'OK', the results of T-test will pop up in the selected output range (table below). This test gives output of both one tail and two tail T-tests. T statistics value are independent of tail (same for both one and two tail tests). P value and t-critical values are different for both tests. The hypothesis and the results interpretation have already been discussed in chapter 4 and 5.

T-test: Two-Sample Assuming Unequal Variances		
	<i>v_Pauli_SI</i>	<i>v_Pauli_OW</i>
Mean	-18.09743214	-12.1387375
Variance	32.62718914	10.31153762
Observations	56	32
Hypothesized Mean Difference	0	
df	86	
t Stat	-6.264111687	
P(T<=t) one-tail	7.15812E-09	
t Critical one-tail	1.662765449	
P(T<=t) two-tail	1.43E-08	
t Critical two-tail	1.987934206	

Appendix IV

Icebergs Ground Truth Profile: Table I and II provide the icebergs pixel and line information in the associating RADARSAT-2 images. The information's have been collected from C-CORE.

Table I: Newfoundland Icebergs

pixel	line	iceberg LenFLIR	iceberg LenISAR_m
RS2_OK86470_IK562928_PEK005909002_FQ10W_20170530_211446_HH_HV_VH_VV_SLC			
730.5	979.5	n/a	30
645.5	1172.5	n/a	95
285.5	1762.3	n/a	83
2414.8	2698.6	n/a	160
2522.6	3018.5	n/a	45
2222.9	4176.2	n/a	95
1431.9	3741.8	n/a	92
2781.4	3807.3	n/a	60
3687.4	4774.4	n/a	30
2956.7	4535.4	n/a	35
RS2_OK87528_IK565076_PEK006014557_FQ9W_20170609_212328_HH_HV_VH_VV_SLC			
4218.8	6284.2	73.6	n/a
3289.2	5221.3	168.5	n/a
2960.6	4401.5	139.2	n/a
929.4	2810	107	n/a
1738	1131.6	154.3	n/a
1818.4	1042.3	115.8	n/a
3391.4	2964.4	n/a	n/a
3391.2	2963.8	71.5	n/a
3908	2983.2	154.4	n/a
4744.1	2906.2	185.5	n/a
4938.2	2891.5	n/a	n/a
4462.9	2088.6	129.5	n/a
4301.2	1889.3	187	n/a
4248.5	1796.5	103.5	n/a

4158.4	1676.2	109.3	n/a
4126	1570.3	102.2	n/a
4079.7	1494.7	96.2	n/a
3631.7	5496.4	120	n/a
3578.1	1825.8	122.1	n/a
4456.4	2658.8	140	n/a
4043.8	671.2	161.9	n/a
2483.9	4085.2	118.4	n/a
3664.8	4233.1	n/a	n/a
4794.1	3348.7	127.2	n/a
3218	1459.6	200.3	n/a
3725.7	1155.2	197.7	n/a
3679.7	573	105.8	n/a
3269.7	240.4	199.7	n/a
3081	65.8	n/a	n/a
RS2_OK88865_PK789651_DK718235_FQ4W_20170530_211543_HH_VV_HV_VH_SLC			
1079.7	5275.8	102.8	n/a
2356.5	4604.6	147.3	100
1181.9	4718.8	103.7	n/a
787.8	3971.2	94.9	n/a
562.8	3532.8	111.5	85
1561.9	3857.4	153.3	110
534.7	2138.3	130.6	45
290.9	1756.1	156.4	70
1885.4	2060.5	62.7	40
92.9	1123.3	n/a	50
930	1538.3	n/a	80
439.4	1188.2	55.8	n/a
536.7	1284.7	124.7	n/a
732.3	1302.8	144.9	n/a
527.5	1386.5	193.8	240
619.7	1308.5	104.8	100 140
758.9	759.7	n/a	n/a
922.4	952	213	60
1082.8	864.5	176.4	100
983.5	586.1	217.9	200
1108.1	629.6	76.6	70
1391	672.1	152.9	88
1549.5	1213.9	121.5	65

1982.8	607	218.2	n/a
1998.9	736.4	233.9	85
1786.9	234.7	240	180
1788.9	46.2	98	n/a
1920.8	249.4	n/a	125
RS2_OK88865_PK789652_DK718236_FQ4W_20170530_211546_HH_VV_HV_VH_SLC			
1388.5	4658.9	181.3	85
1374.4	4587.1	89.9	75
1230.6	4763.7	220	n/a
617.5	4637.1	90	n/a
289.2	3076.6	71.7	n/a
986.7	3909.1	n/a	30
1377	4011.2	257	140
1231.6	3834.5	83.2	n/a
1242.7	3766.1	175.6	n/a
1337.5	3591.4	120.1	n/a
1102.6	3504.5	n/a	35
1095.4	3123.7	179.9	100
2608.4	3580.3	n/a	70
3058.1	3837.2	n/a	115
3122.4	2892.6	215	170
3362.8	2671.9	140	115
2566.7	1956.9	55	40
3073	1250.8	n/a	75
1525.5	2819.7	109.9	30
2054.9	1298.4	78.4	n/a
2196.5	920.9	n/a	45
2183.5	291.1	123.9	50
2205	206.9	n/a	50
1996.5	481.6	156	n/a
1910	673.9	150	n/a
1782.1	974.9	132	60
1770.5	922	n/a	60
1655.4	1297.4	n/a	60
1585.6	1337.5	112.1	n/a
1562.2	1410.3	115.7	n/a
1585.4	1735.2	n/a	35
1903.3	1142.9	90.1	n/a
1689.1	2209.2	90.4	n/a

1525.6	2821.6	108.6	30
756.5	2564.9	89.4	n/a
408.6	2519.4	132.2	n/a
382.5	2121.1	219.6	n/a
220	1207.9	152.4	45
774.8	1694.1	125.8	n/a
1332.2	734.5	185	75
1541.5	259.7	201.3	75
1338.3	832.3	145.1	n/a
RS2_OK88865_PK789653_DK718237_FQ4W_20170530_211549_HH_VV_HV_VH_SLC			
1989.4	4792.1	218.6	37
2419.3	4739.5	162.5	n/a
2970.3	4540.2	n/a	145
1099.6	2661.3	150	140
1058.5	3221.6	100	50
803.5	3837.6	200	145
RS2_OK87528_IK565981_PEK006060035_FQ1W_20170613_210627_HH_HV_VH_VV_SLC			
pixel	line	longitude	latitude
146.5	2929.9	-53.1556	48.64591
26.8	1555.7	-53.1588	48.64297
966.9	3587.9	-52.9821	48.6427
948.9	3590.1	-52.9898	48.64277
899.8	3278.9	-53.0045	48.65306
800.2	3170.8	-53.0251	48.65399
617.8	2434.8	-53.0723	48.68002

Table II: Greenland Icebergs

Original Target Row (Line)	Original Target Column (pixel)	Target Number	RHRV Target Number
RS2_OK7060_PK86521_DK84094_FQ5_20090805_205207_HH_VV_HV_VH_SLC			
3267	1991	BergShell20090805_205207_0006	BergShell20090805_205207_0006RHRVCombo
3303	2081	BergShell20090805_205207_0007	BergShell20090805_205207_0007RHRVCombo
3478	1955	BergShell20090805_205207_0008	BergShell20090805_205207_0008RHRVCombo
3495	2098	BergShell20090805_205207_0009	BergShell20090805_205207_0009RHRVCombo

3468	2141	BergShell20090805_205207_0010	BergShell20090805_205207_0010RHRVCombo
4436	1900	BergShell20090805_205207_0011	BergShell20090805_205207_0011RHRVCombo
4331	1953	BergShell20090805_205207_0012	BergShell20090805_205207_0012RHRVCombo
4510	1728	BergShell20090805_205207_0013	BergShell20090805_205207_0013RHRVCombo
5556	2367	BergShell20090805_205207_0014	BergShell20090805_205207_0014RHRVCombo
6423	1953	BergShell20090805_205207_0015	BergShell20090805_205207_0015RHRVCombo
3543	2115	BergShell20090805_205207_0016	BergShell20090805_205207_0016RHRVCombo
1735	1328	BergShell20090805_205207_0017	BergShell20090805_205207_0017RHRVCombo
2978	44	BergShell20090805_205210_0018	BergShell20090805_205210_0018RHRVCombo
1676	1314	BergShell20090805_205207_0003	BergShell20090805_205207_0003RHRVCombo
1641	1342	BergShell20090805_205207_0004	BergShell20090805_205207_0004RHRVCombo
5081	1341	BergShell20090805_205210_0019	BergShell20090805_205210_0019RHRVCombo
RS2_OK7060_PK87660_DK85431_FQ6_20090815_210036_HH_VV_HV_VH_SLC			
5655	1274	BergShell20090815_210036_0024	BergShell20090815_210036_0024RHRVCombo
6003	1600	BergShell20090815_210036_0025	BergShell20090815_210036_0025RHRVCombo
5874	980	BergShell20090815_210036_0026	BergShell20090815_210036_0026RHRVCombo
2911	1295	BergShell20090815_210036_0022	BergShell20090815_210036_0022RHRVCombo
RS2_OK7060_PK87667_DK85438_FQ7_20090822_205621_HH_VV_HV_VH_SLC			
2063	1701	BergShell20090905_204758_0037	BergShell20090905_204758_0037RHRVCombo
3828	172	BergShell20090905_204758_0038	BergShell20090905_204758_0038RHRVCombo
RS2_OK7060_PK87662_DK85433_FQ16_20090818_211300_HH_VV_HV_VH_SLC			
463	2144	BergShell20090818_211300_0039	BergShell20090818_211300_0039RHRVCombo
392	2076	BergShell20090818_211300_0040	BergShell20090818_211300_0040RHRVCombo
354	2168	BergShell20090818_211300_0041	BergShell20090818_211300_0041RHRVCombo
1349	3088	BergShell20090818_211300_0042	BergShell20090818_211300_0042RHRVCombo
1540	2911	BergShell20090818_211300_0043	BergShell20090818_211300_0043RHRVCombo
2066	2582	BergShell20090818_211300_0044	BergShell20090818_211300_0044RHRVCombo

RS2_OK7060_PK92728_DK91218_FQ2_20090905_204801_HH_VV_HV_VH_SLC			
2710	1059	BergShell20090915_110230_0055	BergShell20090915_110230_0055RHRVCombo
3907	126	BergShell20090915_110230_0056	BergShell20090915_110230_0056RHRVCombo
RS2_OK7060_PK89381_DK86922_FQ11_20090825_210858_HH_VV_HV_VH_SLC			
2392	266	BergShell20090825_210858_0058	BergShell20090825_210858_0058RHRVCombo
2319	287	BergShell20090825_210858_0059	BergShell20090825_210858_0059RHRVCombo
RS2_OK7060_PK87659_DK85430_FQ9_20090815_210029_HH_VV_HV_VH_SLC			
71	2079	BergShell20090815_210029_0060	BergShell20090815_210029_0060RHRVCombo
1981	1899	BergShell20090815_210029_0061	BergShell20090815_210029_0061RHRVCombo
2365	1324	BergShell20090815_210029_0062	BergShell20090815_210029_0062RHRVCombo
RS2_OK7060_PK87666_DK85437_FQ7_20090822_205618_HH_VV_HV_VH_SLC			
554	1470	BergShell20090822_215618_0064	BergShell20090822_215618_0064RHRVCombo
RS2_OK7060_PK86522_DK84095_FQ5_20090805_205210_HH_VV_HV_VH_SLC			
2978	44	BergShell20090805_205210_0018	BergShell20090805_205210_0018RHRVCombo
5081	1341	BergShell20090805_205210_0019	BergShell20090805_205210_0019RHRVCombo
5863	2092	BergShell20090805_205210_0021	BergShell20090805_205210_0021RHRVCombo